Design and Analysis of Gearless Direct-Grid Permanent Magnet Induction Wind Generator

by
Johannes H. J. Potgieter

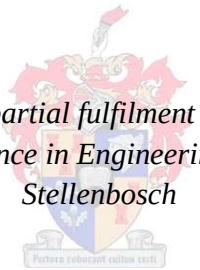

Dissertation presented in partial fulfilment of the requirements for the degree Master of Science in Engineering at the University of Stellenbosch

Supervisor: Prof. Maarten J. Kamper
Department of Electrical and Electronic Engineering

March 2011

DECLARATION

By submitting this dissertation electronically, I declare that the entirety of the work contained therein is my own, original work, that I am the sole author thereof (save to the extent explicitly otherwise stated), that reproduction and publication thereof by Stellenbosch University will not infringe any third party rights and that I have not previously in its entirety or in part submitted it for obtaining any qualification.

Date: March 2011

Summary

In this study a new type of gearless, direct-drive wind generator, which can be connected directly to the grid, is proposed. The working characteristics of this generator are based upon the principles of the permanent magnet induction generator (PMIG). By omitting the need for a gearbox and power electronic converter this generator type has several advantages regarding cost and reliability. Although the PMIG is proposed in previous studies as favourable for wind power generation, the mechanical complexity and difficult construction associated with these types of generators, seems to be the main reason why these generator systems are not used.

The design methods presented in this study are intended to alleviate these constructional issues by proposing the split-PMIG (S-PMIG), where the stator winding and the induction cage-rotor windings are electromagnetically separated. The machine is basically split into two permanent magnet (PM) machines, a grid connected synchronous generator (SG) unit and a turbine connected induction generator (IG) unit. These two units are mechanically linked by a common PM-rotor. To evaluate this concept a finite element (FE) design analysis is done independently for both machine components. The emphasis of the design optimisation is the minimisation of the cogging torque, while still having a decent performing, easily constructible generator. This generator should also have low load ripple content. Cogging torque can result in the failure of the turbine to start up, especially at low wind speeds. As this is a directly grid connected generator, torque ripple transferred to the common PM-rotor can destabilise the generator.

Based upon the FE designs a preliminary S-PMIG system is constructed and practically evaluated. Due to the modular nature of the design it is possible to implement the synchronous generator part of the S-PMIG in conjunction with a grid-connected solid state converter (SSC). This allows for a useful comparison with the S-PMIG system. Promising results are obtained from initial tests of the S-PMIG directly connected to the grid. It is shown that the operation of this generator is stable under a wide range of wind load conditions. However, some important machine design issues are identified from these practical results, which could prove vital in the implementation of future S-PMIG designs.

Opsomming

In hierdie studie word 'n nuwe ratkaslose direk-aangedrewe wind generator voorgestel, wat direk aan die krag netwerk gekoppel kan word. Hierdie generator is gebaseer op die beginsels waarop permanente magneet induksie generators (PMIG's) werk. Deur die ratkas en drywings-elektroniese omsetter uit te laat, het hierdie generator verskeie voordele rakende koste en betroubaarheid. Alhoewel vorige studies hierdie generator voorstel as 'n belowende opsie vir gebruik in wind-energie-stelsels, lyk dit of die meganiese kompleksiteit en moeilike konstruksie die hoof rede is hoekom hierdie generator stelsels tans nie gebruik word nie.

Die ontwerpsmetodes wat in hierdie studie voorgestel word poog om die genoemde konstruksie probleme op te los deur die gesplete-PMIG (S-PMIG), waar die stator wikkelings en die induksie masjien kou-rotor wikkelings elektromagneties ontkoppel is, voor te stel. Hierdie masjien is basies verdeel in twee permanente magneet (PM) masjiene, 'n netwerk gekoppelde sinchroongenerator (SG) eenheid en 'n turbine gekoppelde induksie generator (IG) eenheid. Hierdie twee eenhede word gekoppel deur 'n gemeenskaplike PM-rotor. Om hierdie konsep te evalueer word eindige element analise onafhanklik vir beide masjiene gedoen. Die fokus van die ontwerp optimering is die minimalisering van die vertandingsdraaimoment, terwyl die generator steeds goed presteer en maklik is om te vervaardig. Vertandingsdraaimoment kan tot die gevolg hê dat die turbine versuim om te begin draai, veral by lae windsnelhede. Dit is ook belangrik dat die generator 'n lae rimpel inhoud onder las bevat. Omrede hierdie generator direk aan die netwerk gekoppel is, kan draaimoment pulsasies, oorgedra aan die gemeenskaplike PM-rotor, die masjien destabiliseer.

Gebaseer op die eindige element ontwerpe, is 'n voorlopige gesplete-PMIG gebou en prakties geëvalueer. As gevolg van die modulêre struktuur van die ontwerp, is dit moontlik om die SG gedeelte van die gesplete-PMIG saam met 'n drywings-elektroniese omsetter te implementeer. Dit laat toe vir 'n nuttige vergelyk tussen die twee stelsels. Belowende eerste toets resultate is verkry van die gesplete-PMIG direk gekoppel aan die netwerk. Daar word gewys dat hierdie generator stabiel oor 'n wye operasionele gebied kan funksioneer. Verskeie belangrike masjien ontwerpsfaktore word ook uitgelig met die praktiese evaluering van die gesplete-PMIG. Hierdie faktore kan uiters belangrik wees in die ontwerp en implementering van toekomstige gesplete-PMIG stelsels.

List of Conference Proceedings

The following literature is based upon the work presented in this thesis.

Local Conferences

J.H.J. Potgieter, A.N. Lombard, R. J. Wang and M.J. Kamper, "Evaluation of a permanent magnet excited induction generator for renewable energy applications", Southern African Universities Power Engineering Conference (SAUPEC), Stellenbosch, South Africa, Jan. 2009, pp.299-304.

International Conferences

R. Vermaak, J.H.J. Potgieter and M.J. Kamper, "Grid-connected VSC-HVDC wind farm system and control using permanent magnet induction generators", IEEE International Conference on Power Electronics and Drive Systems (PEDS), Tapei, Taiwan, Nov. 2009.

J. H. J. Potgieter and M.J. Kamper, "Cogging torque sensitivity in design optimisation of low cost non-overlap winding PM wind generator", Proc. of International Conference on Electrical Machines (ICEM'10), Rome, Italy, Sept. 2010 .

J.H.J. Potgieter and M.J. Kamper, "Design of new concept permanent magnet induction wind generator", IEEE Energy Conversion Congress & Expo (ECCE), Atlanta (USA), 12-16 Sept. 2010.

Patent Applications

M.J. Kamper, J.H.J. Potgieter and J.N. Stander, "Split permanent magnet induction generator", South African Provisional Patent Application, Ref No: P2139ZA00, June 2010.

Acknowledgements

I owe great debt to several individuals who have helped me throughout the course of my studies. If I fail to mention anyone, I apologize and please accept my sincerest thanks.

- First off, I would like to thank my supervisor Professor Maarten Kamper. Without his guidance the research presented in this study would never have been possible.
- Adriaan Lombard and Johan Stander who greatly assisted me with the mechanical aspects of all the machine designs presented in this document.
- Also, Ivan Hobbs and Jaco Serdyn with the testing and construction of the converter-fed system, as well as Ulwin Hofmann who assisted me with the testing of the directly grid connected S-PMIG system.
- The help of Arnold Rix and Roger Wang on the FE software.
- Pieter Bouwer who assisted me with the dynamic simulations of the S-PMIG system.
- The help of the various technical lab assistants, Albertu Prins, Ruan Bester and Will Esterhuyse.
- The help of Gert Goosen and Hugo Barnard on the construction of the IG unit.
- The SED workshop; Pietro Petzer, Murray Jumat, and André Swart, as well as the SMD workshop; Jakkie Blom, Jos Weerdenburg and Henry Bennett.
- All the other Electrical Machines Laboratory members throughout the years; thank you for a memorable experience.

Most of the funding regarding my research and studies was granted by the National Research Foundation (NRF). I also received bursary support from the Centre for Sustainable and Renewable Energy Studies (CRSES). Support was also received from the South African National Antarctic Project (SANAP) for the installation of a test wind turbine system at the South African National Antarctic Base (SANAE IV).

Table of Contents

List of Abbreviations and Symbols

Abbreviations

Al	Aluminium	MMF	Magnetomotive force
C-PMIG	Coupled PMIG	OC	Open circuit
Cu	Copper	PM	Permanent magnet
DFIG	Doubly fed induction generator	PMIG	Permanent magnet induction generator
EMF	Electromotive force	PMSG	Permanent magnet synchronous generator
FE	Finite element	RMS	Root mean square
FE-1	Non-commercial custom FE package	SC	Short circuit
FE-2	Magnet v7, commercial FE package	SG	Synchronous generator
FE-3	Maxwell v13, commercial FE package	S-PMIG	Split-PMIG
HVDC	High voltage direct current	SSC	Solid state converter
IG	Induction generator	STATCOM	Static synchronous compensator
IGBT	Insulated-gate bipolar transistor	THD	Total harmonic distortion

Symbols

a	Number of parallel circuits	T_{ave}	Average torque, Nm
a_{scs}	Active SG stator slot conductive area, mm^2	T_b	Pull-out torque , Nm or pu
a_{scr}	Active IG cage slot conductive area, mm^2	T_{cog}	No load cogging torque, Nm
B_g	Air gap flux density, T	T_{gr}	IG or cage-rotor steady-state torque, Nm
C_f	LC filter capacitor, F	T_{gs}	SG or stator steady-state torque, Nm
d_1	Machine air gap diameter, mm	T_L	Load torque, Nm
d	Direct axis	T_m	PM-rotor torque response, Nm
D_i	SG or stator inner diameter, mm	T_s	SG electrical torque response, Nm
d_i	IG or cage-rotor inner diameter, mm	T_t	Turbine torque, Nm
D_o	SG or stator outer diameter, mm	T_{rated}	Rated machine torque, Nm
d_o	IG or cage-rotor outer diameter, mm	T_c	Winding temperature, °C
E_1	SG or stator winding induced voltage, V	t_s	Settling time, s
E_2	IG cage winding induced voltage, V	V_1	SG or stator per phase voltage, V
E_{dr}	IG steady-state *d*-axis induced voltage, V	v_{abc}	Indicates three-phase voltages, V
E_{ds}	SG steady-state *d*-axis induced voltage, V	v_{dc}	SSC DC-bus voltage, V
E_{qr}	IG steady-state *q*-axis induced voltage, V	V_{ds}	SG steady-state*d*-axis terminal voltage, V
E_{qs}	SG steady-state *q*-axis induced voltage, V	v_{ds}	SG *d*-axis voltage response, V
E_s	Magnetic branch voltage (C-PMIG), V	V_{qs}	SG steady-state *q*-axis terminal voltage, V
f_1	Fundamental SG or stator frequency, Hz	v_{qs}	SG *q*-axis voltage response, V

h_m	PM height, mm	V_k	Voltage harmonic component (k = 2,3,...), V
h_r	PM-rotor yoke height, mm	V_{LL}	Line voltage, V
h_s	SG stator or IG cage-rotor yoke height, mm	V_{oc}	Open circuit terminal voltage, V
I_1	SG or stator per phase current, A	v_w	Wind speed, m/s
i_1	Per phase current response, A	w	Weighting factor
I_2	IG or cage-rotor per phase current, A	W_1	Number of series turns per phase
I_{dr}	IG steady-state d-axis current, A	W_s	Number of winding sections
i_{dr}	IG d-axis current response, A	$\mathbf{X}$	Optimisation input parameter vector
I_{ds}	SG steady-state$d$-axis current, A	x	Optimisation parameter
i_{ds}	SG d-axis current response, A	x_0	Optimisation parameter boundary limit
I_m	IG and C-PMIG magnetizing current, A	X_1	SG or stator per phase reactance, Ω
I_{qr}	IG steady-state q-axis current, A	X_2	IG or cage-rotor per phase reactance, Ω
i_{qr}	IG q-axis current response, A	X_m	Magnetizing reactance, Ω
I_{qs}	SG steady-state q-axis current, A	$\mathbf{Y}$	Optimisation output parameter vector
i_{qs}	SG q-axis current response, A	α_r	IG current angle, degrees or radians
I_{sc}	Short-circuit current, A	α_s	SG current angle, degrees or radians
J_1	Inertia experienced by SG, kg.m^2	Δ	SG power angle, degrees or radians
J_2	Inertia of cage and turbine, kg.m^2	δ_m	SG mechanical power angle, degrees or radians
J_s	SG current density, A.mm^{-2}	δ	Equivalent air gap size, mm
J_r	IG current density, A.mm^{-2}	δ''	Equivalent air gap size (saturated), mm
k	Harmonic index	δ_1	Air gap; SG and cage or SG and PM-rotor, mm
K_1	SG machine constant (Chapter 5)	δ_2	Air gap; cage and PM rotor, mm
K_2	IG machine constant (Chapter 5)	δ_3	Air gap; shaft and PM-rotor, mm
$\mathbf{K_s}$	Park transformation vector	Δt	Time step, s
k_w	Fundamental winding factor	ΔT_{cog}	Peak to peak no-load cogging torque, Nm
L_1	SG per phase winding inductance, H	$\Delta\tau$	Per unit cogging torque, pu
L_2	IG per phase winding inductance, H	$\Delta\tau_L$	Per unit load torque ripple, pu
l_1	SG axial stack length, mm	ε	Penalty function used in optimisation
l_2	IG, axial stack length, mm	η_t	Overall system efficiency, %
L_{dr}	IG d-axis inductance, H	η_1	SG efficiency, %
L_{ds}	SG d-axis inductance, H	η_2	IG efficiency, %
L_{qr}	IG q-axis inductance, H	θ	Power factor angle, degrees
L_{qs}	SG q-axis inductance, H	θ_e	Rotor electrical angle, degrees
L_f	LC filter inductor, H	θ_M	Rotor mechanical angle, degrees
N_r	IG number of turns per coil	θ_g	Slot width, degrees

N_s	SG number of turns per coil	θ_m	Magnet pitch, degrees
n_r	Cage rotor operating speed, r/min	θ_t	Slot pitch, degrees
n_s	Synchronous speed, r/min	θ_w	Slot opening width, degrees
n_t	Wind turbine rotational speed, r.min^{-1}	θ_P	Average pole section, degrees
p	Number of poles	θ_S	Average slot section, degrees
P_{cur}	IG copper losses, W	λ_1	SG or stator per phase flux linkage, Wb.t
P_{cus}	SG copper losses, W	λ_2	IG per phase flux linkage, Wb.t
P_{ecr}	IG rotor eddy current and core losses, W	λ_3	PM defined coil flux linkage, Wb.t
P_{ecs}	SG rotor eddy current and core losses, W	λ_{abc}	Three-phase flux linkages, Wb.t
P_{er}	PM-rotor eddy current losses, W	λ_{dr}	IG *d*-axis flux linkage, Wb.t
PF	Power factor	λ_{ds}	SG *d*-axis flux linkage, Wb.t
P_{gr}	IG or cage output power, kW	λ_{mr}	IG PM flux linkage, Wb.t
P_{gs}	SG or stator output power, kW	λ_{ms}	SG PM flux linkage, Wb.t
P_{NL}	No-load losses, W	λ_{qr}	IG *q*-axis flux linkage, Wb.t
P_t	Mechanical turbine power, kW	λ_{qs}	SG *q*-axis flux linkage, Wb.t
P_{wfr}	IG wind and friction losses, W	μ_0	Permeability of air, $4\pi.10^{-7}$, H/m
P_{wfs}	SG wind and friction losses, W	ρ_{Cu}	Resistivity of copper, Ω/m
q	Quadrature axis	σ_g	Slot width to average slot pitch ratio, pu
Q	Single-layer (Q = 1) or double-layer (Q = 2)	σ_m	Magnet pitch to average pole pitch ratio, pu
q_1	Stator slots per pole per phase	σ_t	Slot pitch to average slot pitch ratio, pu
Q_1	X_1 reactive power (Chapter 2), kVAr	σ_w	Slot opening to slot width ratio, pu
Q_{gs}	SG or stator reactive power, kVAr	τ_{ave}	Per unit average torque, pu
Q_m	IG magnetic branch reactive power, kVAr	ϕ_1	SG and C-PMIG air gap flux per pole, Wb
Q_{NL}	No-load reactive power, kVAr	ϕ_2	IG air gap flux per pole, Wb
r	FE program counter	ω_e	PM-rotor electrical speed, rad/s
R	Number of cage-rotor slots	ω_m	PM-rotor mechanical speed, rad/s
R_1	SG or stator per phase resistance, Ω	ω_s	Synchronous electrical speed, rad/s
R_2	IG or cage-rotor per phase resistance, Ω	ω_{sm}	Synchronous mechanical speed, rad/s
R_m	Core loss resistance, Ω	ω_{sl}	Slip electrical speed, rad/s
S	Number of stator slots	ω_{slm}	Slip mechanical speed, rad/s
s	Laplace operator, or slip, pu	ω_t	Turbine speed, rad/s
s_r	Rated slip, pu	ω_n	Undamped natural frequency, rad/s
t	Time, s or ms	ς	Damping coefficient

Chapter 1 - Introduction

1.1 Background

The need to harness alternative energy resources is inevitable and this topic does not need any further elaboration. Wind energy has the potential to make a large contribution to the sustainable energy mix. This energy source is currently the most widely deployed and commercially used renewable energy resource. However, like most other renewable energy harnessing methods, generating electricity from wind is still expensive. High initial capital cost of installations and long payback periods on wind power investments still hamper the full potential of this resource. To address these issues, research in the field of wind energy constantly presents new and innovative means of harnessing this energy resource, more efficiently and cost effectively.

1.1.1 Major wind power systems currently in use

A key topic in the installation of new wind generation systems is the selection of the optimum drive train. Several options are available, but currently there are only three types of technologies which dominate the market, with each option exhibiting different advantages and disadvantages.

Up until recently most commercial wind generation systems consisted of a gearbox and high speed asynchronous squirrel cage induction generator (IG) directly connected to the utility grid as shown in Fig. 1.1(a)[1-5]. Although IG systems can be assumed to operate at a fixed turbine speed, a slight speed variation is possible. Depending on the applied load, the cage induction rotor of this generator operates at a speed that differs from that of the synchronous grid. The speed difference is known as the slip speed. Due to this slip, these generators can be directly connected to the grid.

A variation of the IG known as the doubly fed induction generator (DFIG) as in Fig. 1.1(b) is the most popular choice in current wind generation installations [1]. DFIG systems can operate at variable turbine speeds, with a speed variation of +/- 30% around the synchronous speed. A power electronic converter controls the frequency in the wound rotor of the DFIG. This power electronic converter, however, only needs to be rated at partial load. As it is connected to the DFIG rotor, it only needs to be able to handle the rotor power which is typically 25% to 30% of the generator rated power [1].

The newest trend in wind generator design is direct-drive (gearless) systems. In these systems a synchronous generator (SG) is directly connected to the turbine without making use of a gearbox as shown in Fig. 1.1(c). The SG can either make use of a wound-rotor that is externally excited, or the rotor can be excited by permanent magnets. The current and future tendency seems to be the permanent magnet synchronous generator (PMSG). To interface the SG with the utility grid a full rated power electronic converter, which also allows for full variable speed operation, is needed. In a grid connected system the SG can only be connected directly to the grid if a steady power flow is available. Due to transient torques generated by the wind turbine, these systems will be unstable in a wind generation system if directly connected to the grid.

1.1.2 Drive train implementation issues

At present the choice of drive train system is mostly governed by cost, with the emphasis being on the initial capital cost of wind generator installations. However other factors, like maintenance requirements and system downtime caused by component failures, also significantly contributes to the cost of energy production. Reliability is thus another important criterion in the choice of the optimum drive train.

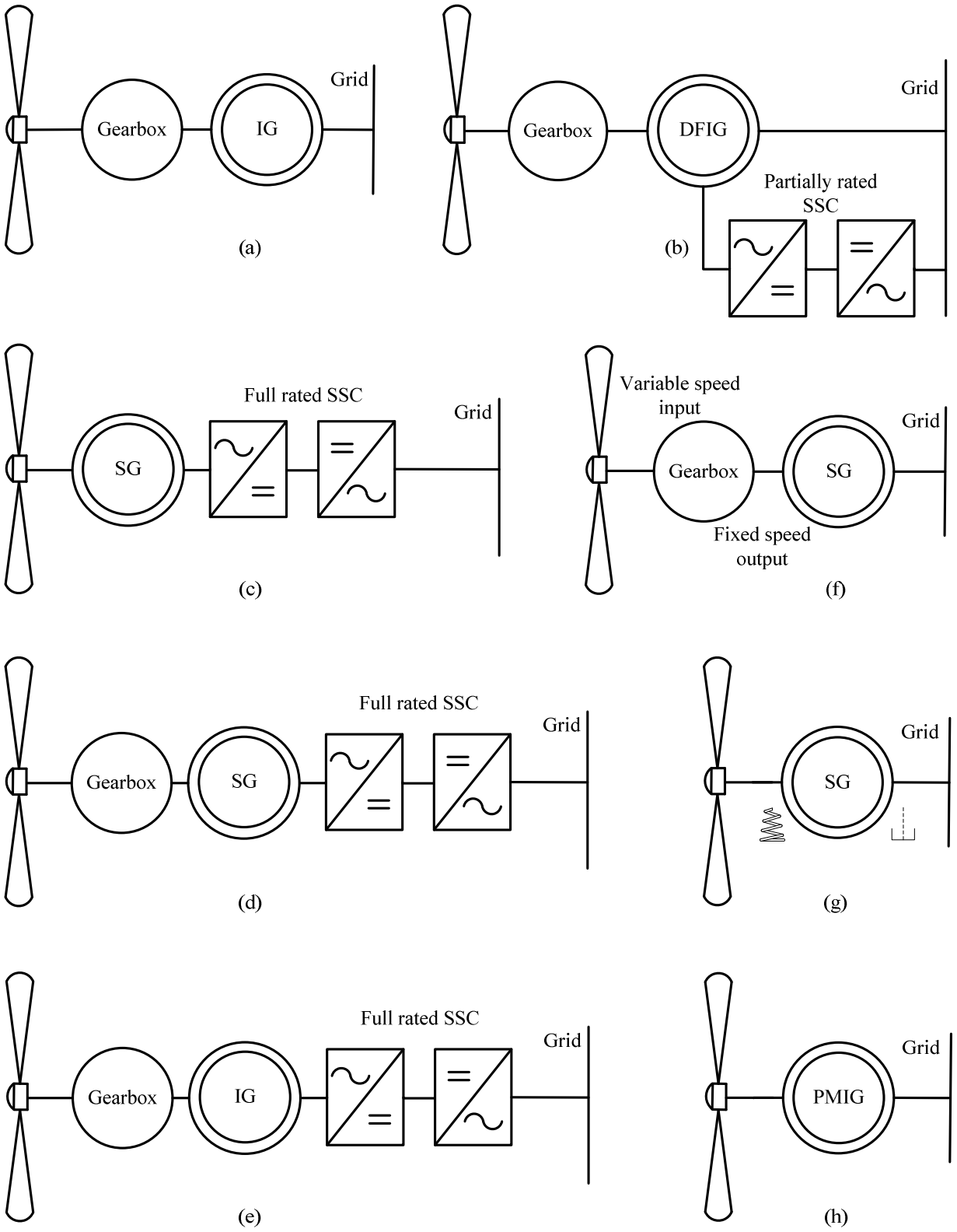

Figure 1.1: Different wind generator drive train lay-outs with (a) IG with gearbox; (b) DFIG with gearbox and partially rated converter; (c) SG with full rated converter; (d) SG with gearbox and full rated converter; (e) IG with gearbox and full rated converter; (f) directly grid connected PMSG with constant output speed gearbox; (g) directly grid and turbine connected SG with additional damping added and (h) directly grid and turbine connected PMIG system.

A large driving force behind the current trend to move to direct-drive generators is the fear of gearbox failure, which leads to prolonged turbine standstill times. Down time caused by component failures in wind farms, will have a significant impact on the investment returns of wind energy projects. With several stages of gearing needed in large wind turbine systems, the gearboxes used in these systems with several moving parts are also expensive and maintenance intensive.

However, power electronic converters in direct-drive systems are not faultless and system faults still occur, which also contributes to system downtime. Although not one of the main cost contributors, power electronic converters still add a significant portion to the overall cost of a wind generation setup [5].

Other factors governing the choice of drive train, are the connection requirements of the utility grid. With wind power penetration increasing every year, the impact of wind turbine systems on power systems grows larger [1]. Grid connection standards for wind turbine systems are increasingly focussing on issues concerning low voltage ride through capability and reactive power control. In this regard it seems that wind generation systems with full rated converters perform the best and directly grid-connected cage induction generators the worst.

To address some of the implementation issues associated with current drive train technologies, variations of the classical drive trains are used. In some cases combinations of converter fed PMSGs and gearboxes are used, known as hybrid systems, as shown in Fig. 1.1(d).The problem with direct-drive generators is the sheer size, as the generator needs to deal with the full torque developed by the wind turbine. If a full geared system is implemented a much smaller generator can be used. However, if a smaller high speed generator is used at least three stages of gearing are needed. Hybrid systems on the other hand utilise a medium speed generator, which means that fewer gearing stages are needed. Hybrid systems are more reliable than full geared systems and at current they seem more economical than full direct-drive systems [5].

Another variation of current drive train systems is the use of cage induction generators and full scale converters as shown in Fig. 1.1(e). This alleviates many of the grid connection aspects associated with these generator types and it also allows for variable speed operation. Although the future norm seems to be gearless systems, a geared system with an IG seems to be the most inexpensive currently. This appears to be the main reason why geared IG systems are still used.

1.1.3 Non-conventional and experimental wind generator concepts

In the next section some studies that have been conducted on the feasibility of a number of non-conventional wind power system types are mentioned. These systems deviate from the more conventional drive trains previously mentioned and are not currently implemented in large scale systems.

Although methods can be implemented to increase the reliability of conventional gearboxes, gearless systems will always have the upper hand regarding reliability. However with the use of novel technologies like PM gearboxes the performance, reliability and maintenance needs of gearboxes can be largely improved [6].Although these systems are much less prone to failure and require almost zero maintenance, further studies need to be done in order to determine whether the higher cost of these systems due to the use of more PM material can be justified.

In [7] a variable speed, hydro-dynamically controlled gearbox with a smooth power output at a constant speed is proposed for use with a directly grid connected PMSG as shown in Fig. 1.1(f). It was found in this study that the directly grid connected SG offers a stable grid connection and supports the grid when short circuit faults occur. Although this type of wind power system has advantages, the complexity and reliability of the hydro-dynamically controlled gearbox needs to be evaluated to a further extent.

In all of the pre-mentioned drive train configurations an electrical machine is operated in conjunction with either a gearbox, or a power electronic converter, or both. However, some previous work has been done on gearless, direct online PM synchronous wind generators. In [8] an unconventional method is proposed where a PMSG is used in conjunction with a mechanical spring and damper system to damp power angle

oscillations, as shown in Fig. 1.1(g). This system is reported to provide better damping than conventional damper windings usually incorporated within synchronous machines. Currently no information exists on the successful implementation of such a system.

Another direct-drive, directly grid connected generator configuration proposed in literature, is the Permanent magnet induction generator (PMIG) [9-30]. Although IGs can be connected directly to the power grid, these machines cannot be connected directly to a wind turbine, as it is not possible to utilise low speed large diameter induction machines efficiently. The PMIG on the other hand, combines the direct-drive gearless capabilities of the PMSG and the soft direct grid-connection of the IG within one generating unit. These machines can be directly connected to the turbine and to the utility grid as shown in Fig. 1.1(h). In such a system gearboxes and power electronic converters can be omitted, simplifying the drive train to a large extent. This thesis further describes the PMIG concept. In the next sections the feasibility of the PMIG concept is evaluated and methods are developed and proposed to enable the successful implementation of such a device. Fig. 1.2 shows an example of a PMIG.

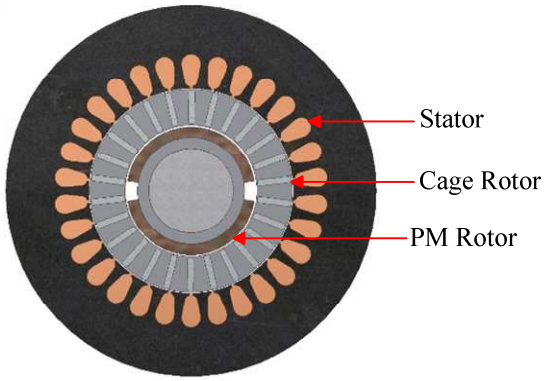

Figure 1.2: Section view of an example PMIG.

1.2 Existing knowledge of PMIG systems

Although a fair amount of literature exists on the PMIG concept, the idea is still relatively unknown in wind energy. In the next section some information on the concept as well as a review of the most important PMIG literature currently available is presented.

1.2.1 PMIG working characteristics

The PMIG idea originated from the need to improve the power factor of induction machines. A standard induction machine consumes a relatively large amount of reactive power due to the relatively large magnetizing current. This magnetizing current supports the flux within the machine. In current wind generation systems the magnetizing current can be supplied by the utility grid, but this results in a poor power factor. Normally a capacitor bank is used to produce the reactive power needed.

The PMIG makes use of an additional free rotating PM-rotor which operates independently from the cage-rotor of an induction machine. Mechanical to electrical power transfer still takes place via the induction machine cage-rotor. In Fig. 1.2 the PM-rotor is situated within the induction machine squirrel-cage-rotor, with the machine stator on the outside. This PM-rotor rotates synchronously under steady state conditions with the revolving stator field. The PM-rotor supplies the magnetic flux within the machine and induces a voltage in the stator winding. This in principle reduces the magnetizing current and improves the power factor of the machine.

1.2.2 Previous PMIG research

The internally excited induction machine concept originated as early as 1926 from the work reported in [9]. An internally excited induction machine with electromagnets on a secondary rotor is proposed as a single phase electrical locomotive drive. This concept seemed unpractical at the time due to the use of electromagnets and slip-rings.

In 1959 [10] proposed the use of permanent magnets for the first time. Already in this study several constructional issues surfaced, which impose significant constraints on the design. It was also concluded that the PMIG is more suited to higher pole numbers, due to the limited amount of space available for flux penetration in lower pole number machines. This study was followed in 1967 by [11], where the use of permanent magnets was proposed for the construction of a small scale PMIG prototype. It was concluded by both [10] and [11] that this machine has large potential, but due to the limitations on PM material at the time, this machine type was deemed unpractical as well.

With the advances made in PM materials, a prototype PMIG was constructed in 1992 by [12] using high power density magnets. The topology of this prototype was mostly based on the structures proposed in the literature mentioned above. To limit the reactive power flow, it is important that the PM-induced-voltage matches the grid voltage as mentioned in [12]. In [12] a limitation on the matching of the PM-induced-voltage and the grid-voltage for this machine was found to be the size of the stator leakage reactance. As the load increases, the voltage drop over this impedance increases as well. This in turn leads to a larger difference between the induced and the grid voltage.

Since 1999 more relevant literature on the PMIG topic has surfaced from the Technical University Darmstadt, Germany. This includes the work reported in [13-17]. In [13] and [14] the PMIG is proposed for the first time as a direct-drive, directly grid connected solution for wind energy applications. This originated from the need for low maintenance wind generating solutions for offshore wind turbine systems. Furthermore the advantages of a more robust and possibly more cost effective system by omitting the full rated IGBT converter, are mentioned.

Also reported in these studies is some explanation of the inefficient utilisation of induction generators at low speeds. For low speed, large diameter machines a large air gap needs to be specified to accommodate for mechanical deformations. Also, as the pole pitch becomes smaller, with an increase in the number of poles, the air gap/pole-pitch-ratio becomes larger for lower speed machines. With the magnetizing current proportional to the air gap/pole-pitch-ratio, the power factor and efficiency of the machine will decrease accordingly.

The PMIG is also compared with a conventional IG plus gearbox system. Favourable performance is observed, especially at partial load where the PMIG has a much better efficiency than the IG with gearbox. Initial transient measurements for a small scale prototype find the PMIG to operate in a stable way, with no dynamic oscillations which might destabilise the system being observed.

Research on the concept of a PMIG surfaced in Japan in 1996 in the Toyota Technological Institute. In this research the focus was again on the improvement of conventional induction machines. The work done in [18] and [19] proposes a new type, high torque induction machine by incorporating permanent magnets within the design. This prototype showed several performance improvements over conventional induction machines.

Further research in Japan was done by the Kanazawa Institute of Technology, starting in 2002. Most of the research mentioned in what follows is based upon a small scale experimental PMIG prototype. In [20] unlike the other Japanese research, the PMIG is proposed as a generator. This is due to the inability of the PMIG to line start if it is operated as a motor. The machine thus needs a mechanical source to bring it up to the required synchronous speed, which makes it more attractive as a generator. This research was followed by [21] in 2003. In 2004 a more refined technique is presented to predict the performance of the PMIG [22].

More research work is described in [23] on the performance of the PMIG connected to a single phase grid and on the inrush current of a PMIG in [24]. The last known research work done is described in [25], where the effects of the PM-rotor on the equivalent circuit parameters was investigated. In [25] the PMIG is also compared with a conventional same sized IG. The PMIG was found to perform much better than the conventional IG.

Some interesting work originating from the Massachusetts Institute of Technology where a doubly-fed PM generator for wind energy applications was evaluated [26]. In this study a free rotating PM-rotor is combined with a conventional stator and a wound rotor which is connected to the wind turbine. By using a converter to modify the wound rotor frequency, this machine can be implemented as a variable speed wind energy converter. This system is also proposed as a direct-drive system without a gearbox.

The latest research on the PMIG concept is reported by [27-29]. In [27] a small prototype is constructed and evaluated, mostly based upon the methods introduced in previous literature. In [28] the PMIG is proposed for use in a HVDC distribution network. Several PMIGs are connected in an AC collection grid of which the frequency and voltage is controlled by a single power electronic converter to enable optimum power point tracking. A central DC transmission is used to convey power to the main distribution point. The latest published research on PMIGs is contained within [29].Here a new concept PMIG is presented, which proposes to alleviate many of the constructional difficulties previously associated with this device.

In all the discussed literature the PMIG is identified as a generating solution which shows great potential. However, only small-scale prototypes have been built thus far and no proof could be found of a fully implemented large diameter, high pole operational PMIG. The main reason seems to be the mechanical complexity associated with this generator. However, from all literature it is evident that the PMIG concept should definitely be investigated further to find out whether this is a feasible concept.

1.3 Proposed solution

The main reason for proposing the use of a PMIG is to simplify the wind generator system drive-train, by omitting the gearbox and power electronic converter. However, although the drive-train is simplified the electrical generator is made more complex. The main aim in this study, thus, is to present a mechanically feasible and simple permanent magnet induction generator construction, which can be realised as a high pole large diameter wind generator. The resulting wind generation system should be cost effective, simple, robust and almost maintenance free.

To lessen the mechanical complexity of this generator, a method is introduced in this study to electromagnetically split the grid-connected synchronous-generator-stator-unit and the turbine connected induction-type-cage-unit. These two units are each presented with a separate set of PMs, providing separate excitation for each unit. The machine can thus be approached as two separate PM machines mechanically linked by a common PM-rotor. The grid-connected unit is referred to as the SG and the turbine connected unit is referred to as the IG. The cross section of a machine of this type is shown in Fig. 1.3. To fully capitalise on the split-PMIG (S-PMIG) concept, instead of radially separating these two machines as shown in Fig. 1.3, it is proposed that the two machines be separated axially as shown in Fig. 1.4 [29].

The concept of magnetically separating the two machines has several advantages over the conventional coupled PMIG (C-PMIG). The C-PMIG refers to the classical coupled PMIG concept as described in the reviewed literature. There is no real mass disadvantage as the amount of material used for both PMIGs are more or less the same. With the same amount of PM material used, only the amount of yoke material will increase, but for high pole machines this increase will be low.

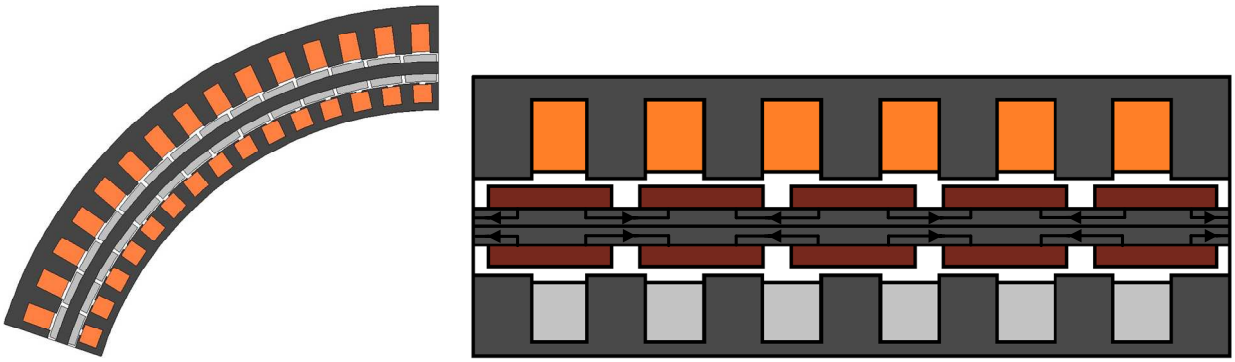

(a) (b)

Figure 1.3: (a) Electromagnetically split-PMIG, (b) with separate flux paths.

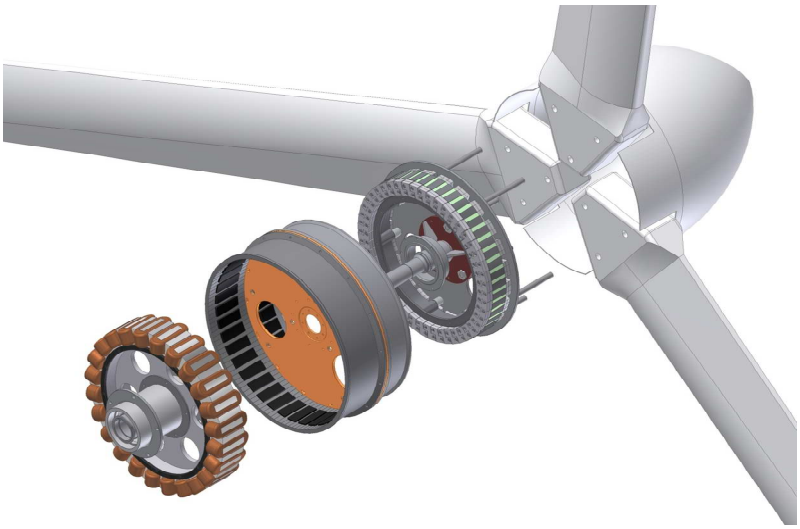

Figure 1.4: Electromagnetically, axially separated, S-PMIG [29].

A completely modular approach can be followed for the design of both the SG and IG units. By making use of the conventional C-PMIG concept only overlap windings can be used for both the SG and IG. For the S-PMIG there is no limit on which winding configuration to use and different winding lay-outs can be used for each unit. The amount of poles and the pole-slot combinations for both units need not to be the same. There is also more freedom regarding the dimensional constraints. This is especially true if the axial separation method is used. In this case the air gap diameters of both machines can be set at a maximum, resulting in a better overall machine performance.

Another advantage of axially separating the two machine units is the modularity of the manufacturing and assembly processes. In this study, it is also proposed that it should be easy to remove the SG and IG units from one another. If the IG is removed the SG can be used and be operated as a conventional direct-drive PMSG with a full scale converter as in Fig. 1.1(c). With the IG attached, the combination can be used as a direct-drive, direct online system as in Fig. 1.1(h).By evaluating both system types an insightful comparison can be made between the two systems.

The overall design aim of presenting the combined generating unit as an easily constructible, cost effective, efficient alternative, to other wind generating solutions needs to be applied separately to the design of both the SG and IG units. With, in effect two PM generators on top of the wind turbine tower, another design goal is to keep the mass of the whole S-PMIG within reasonable bounds. Finally the S-PMIG system needs to offer a stable grid connection and be able to operate under all wind generation modes of operation.

1.4 Thesis outlay

With the basic working theory and background of the PMIG system and the new concept S-PMIG system covered, the focus of the rest of this thesis (except for Chapter 2) will be on the evaluation and design of an S-PMIG system.

A first evaluation of the conventional C-PMIG system, as done in Chapter 2 gives a basic idea of the working characteristics of a C-PMIG system. This experimental study is mostly based upon the literature as previously discussed.

The design of the new proposed S-PMIG system is done in two steps. A first design focuses on the grid connected PMSG as obtained in Chapter 3, while a second design iteration focuses on the turbine connected IG unit as obtained in Chapter 4. With both machines being PM machines, most of the design procedures developed can be used for both machine types. A full FE design analysis results in the optimum machine design in both cases.

The focus of further studies is on the combination of the two machines. This relates to the mechanical interaction with the turbine as well as the electrical interaction with the grid. The latter is done to validate the stability of the grid-connected PMIG system as described in Chapter 5.

As far as possible all simulation results are validated in Chapter 6 by practical measurements on a prototype S-PMIG, which has been designed and developed based on the analysis of this study.

Chapter 2 – Classical PMIG Concept

The classical PMIG refers to the original coupled-PMIG (C-PMIG) concept as first introduced by [9] in 1926. To gain practical knowledge on the operation of PMIG systems and to get a basic idea on the limitations mentioned in literature, there will be a discussion in this chapter of the evaluation of a small scale conventional C-PMIG prototype.

2.1 Conventional IG operation

To gain a better understanding of why high pole large diameter IGs are not used some information on the conventional IG will be given in this chapter. Fig. 2.1 shows the per phase equivalent circuit of the IG. In Fig. 2.1 V_1 is the per phase grid voltage connected across the terminals of the machine. R_1 and X_1 are the per phase stator resistance and synchronous reactance respectively. The rotor resistance and reactance is indicated by R_2 and X_2. I_1 is the primary stator current and I_2 is the per phase current circulating in the rotor bars. R_m and X_m represent the core loss resistance and the magnetizing reactance respectively. The magnetic branch voltage is indicated by E_s and the magnetizing current by I_m. It should be noted that all the parameters indicated in the per phase equivalent circuit are referred to the primary stator winding.

For the IG the magnetizing reactance and current are given as

$$X_m = \frac{6 f_1 W_1^2 k_w^2 d_1 l_1 \mu_0}{p^2 \delta''}; \tag{2.1}$$

$$\mathbf{I_m} = \frac{\mathbf{E_s}}{jX_m}. \tag{2.2}$$

In (2.1) f_1 is the operating frequency, W_1 the number of series turns per phase, k_w the fundamental winding factor, d_1 the machine air gap diameter,l_1 the axial core length, p the number of poles and δ'' indicates the equivalent air gap length with saturation taken into account. In (2.1) it is shown that the magnetizing reactance is inversely proportional to the square of p and the equivalent air gap length (δ), which in this case is the air gap between the stator and the cage-rotor (δ_1). [31], [32].

In most design cases the ratio of d_1 to δ stays roughly constant, but in bigger machines this ratio might change to incorporate larger tolerances as mentioned in [13] and [14]. For the same size machine, if X_m decreases with an increase in δ, from (2.1) and (2.2) it is observed that I_m will increase. With an increase in I_m the magnetic branch reactive power demand (Q_m) increases accordingly with

$$Q_m = 3 I_m^2 (X_m), \tag{2.3}$$

which in turn leads to a lower power factor.

To investigate the effect of increasing p it is assumed that δ stays constant. With an increase in p,W_1 increases accordingly with

$$W_1 = \frac{Q N_s q_1 p}{a}. \tag{2.4}$$

In (2.4) [31] Q indicates a single-layer (Q = 1) or a double-layer winding (Q = 2), N_s is the number of turns per stator coil, q_1 is the number of slots per pole per phase and a is the number of parallel circuits. The ratio of W_1 to p thus stays constant, which means that X_m as given in (2.1) stays constant for an increase in p for the same diameter machine. However it is known for the IG that

$$E_s = \sqrt{2}\pi f_1 k_w W_1 \phi_1 = I_m X_m \quad \text{and} \quad \phi_1 = B_{gpeak}\left(\frac{d_1}{p}\right). \tag{2.5}$$

B_{gpeak} is the peak value of the fundamental air gap flux density and ϕ_1 is the flux per pole per phase. For a grid connected system E_s and f_1 needs to stay constant. However from (2.5) it is observed that if d_1 stays constant as p and W_1 increase the flux per pole per phase will decrease, which means that E_s stays constant.

For the higher pole IG with d_1 constant the output power is given as

$$P_{gs} = T_{gr}\omega_{sm};\quad \omega_{sm} = \frac{4\pi f_1}{p}. \tag{2.6}$$

The output power (P_{gs}) of the IG is thus inversely proportional to p, with ω_{sm} the synchronous mechanical speed and T_{gr} the torque of the IG. As P_{gs} decreases with an increase in p, Q_m stays constant as X_m and I_m stay constant as observed from (2.1) and (2.2). The ratio of P_{gs} to Q_m thus worsens with an increase in p. Furthermore

$$Q_{gs} = Q_1 + Q_m;\quad \theta = \tan^{-1}\left(\frac{Q_{gs}}{P_{gs}}\right);\ \mathrm{PF} = \cos(\theta). \tag{2.7}$$

with Q_{gs} the total reactive power demand and Q_1 the reactive power demand of the stator winding. The decrease in power factor (PF) can thus be explained by (2.7), with θ the power factor angle.

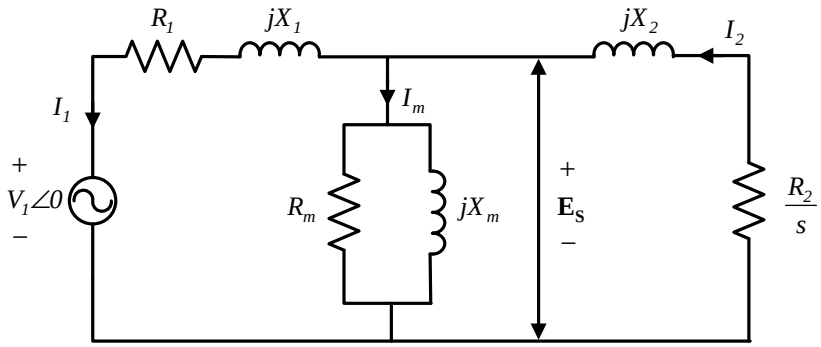

Figure 2.1: Equivalent circuit of a conventional IG.

2.2 PMIG operation and equivalent circuit

The basic operational principles of the C-PMIG are still very much the same as for conventional IGs. The only difference is that the flux is generated by the permanent magnets. This PM generated flux induces a voltage (E_1) in the stator winding that is modelled as a voltage source, in series with X_m and in parallel with (R_m). This is indicated in the per phase equivalent circuit shown in Fig. 2.2.

For the PMIG the magnetizing current is given by (2.8) as

$$\mathbf{I_m} = \frac{\mathbf{E_s} - \mathbf{E_1}}{jX_m}. \tag{2.8}$$

From (2.8) it is seen that if the internally induced voltage, E_1, of the PMIG can be closely matched to E_s, the magnetizing current can be significantly countered. In turn this will reduce the reactive power demand and improve the power factor of the machine to a large extent.

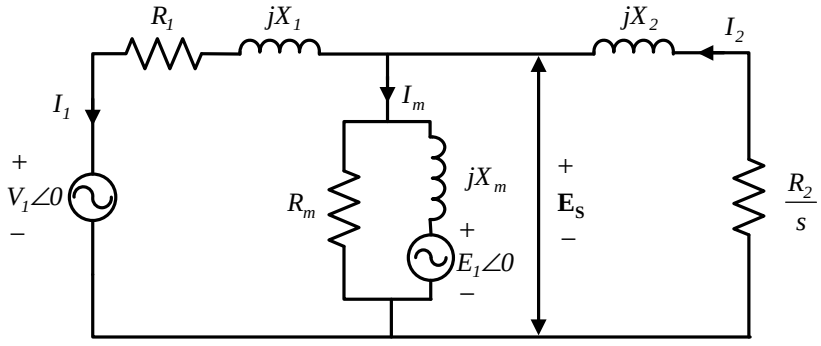

Figure 2.2: Equivalent circuit of a conventional C-PMIG.

2.3 Proposed implementation of a prototype PMIG

As the investigation in this Chapter is mostly experimental in nature, the same approach is followed as in most literature, namely by modifying a conventional induction machine to a PMIG.

An advantage of modifying an existing machine is that an adequate comparison can be made between the modified machine and the original IG. This comparison will give a clear indication on the effects caused by the PM-rotor. The IG used in the investigation in this Chapter is described in Table 1.

With the use of an existing IG, the only component which needs to be designed and manufactured is the PM-rotor. However, modifications have to be made to either the stator or the IG cage-rotor, to incorporate the PM-rotor within the machine. Each of the proposed topologies in Fig. 2.3 will have a different effect on the machine.

To select the most suitable configuration, each of these topologies needs to be evaluated. The first option is to place the PM-rotor between the IG cage-rotor and the stator as in Fig. 2.3(a). However, if using a radial flux machine as is currently the case, dimensional constraints become a limitation. If an axial flux machine is used as shown in Fig. 2.4 with the PM-rotor between the cage and stator, the topology in Fig. 2.3(a) is the best option. For the prototype under discussion with the PM-rotor between the cage and stator, either the inside diameter of the stator (D_i) needs to increase or the outside diameter of the rotor (d_o) needs to decrease.

By increasing D_i the machine becomes bigger and heavier, increasing the power density of the stator. If d_o is decreased the power density of the rotor will be decreased. Both of these modifications will result in the comparative study with the unmodified IG being no longer valid.

For a valid comparative study D_i and d_o need to stay fixed. This is only possible if the PM-rotor is placed on the inside of the cage rotor as shown in Fig. 2.3(b) or on the outside of the stator as shown in Fig. 2.3(c). If the PM-rotor is placed on the outside of the stator, the stator yoke must be removed. However, this back yoke is shifted to the PM-rotor and thus has little effect on the overall mass increase of the machine. If the PM-rotor is placed inside the cage rotor, a significant amount of the cage rotor yoke material must be removed. Unlike the option of placing the PM-rotor outside the stator, where the placement of the PM rotor is radially outward, the PM-rotor is placed radially inward. This means that the yoke material removed cannot be replaced. This will have a definite effect on the rotor parameters and the output characteristics of the machine.

Performance wise the best option, thus, seems to be to place the PM-rotor on the outside of the stator. Although the outside radius of the overall machine will increase, the only mass added will be the addition of the permanent magnets. The amount of yoke material in the machine should stay the same.

However, construction wise, the option of placing the PM-rotor on the outside proves to be the most difficult and expensive. Assembling the machine could also prove difficult in this case, as the large overhang created by the three phase windings could complicate the placing of the PM-rotor. When taking all the above mentioned constraints and design objectives into account, the most suitable option identified is to place the PM-rotor inside the cage rotor. A cross section of the proposed induction machine modification with the PM-rotor inside the squirrel cage-rotor is shown in Fig. 2.5(a), with the IG cage-rotor to be modified shown in Fig. 2.5(b). The conventional IG is shown in Fig. 2.5(c).

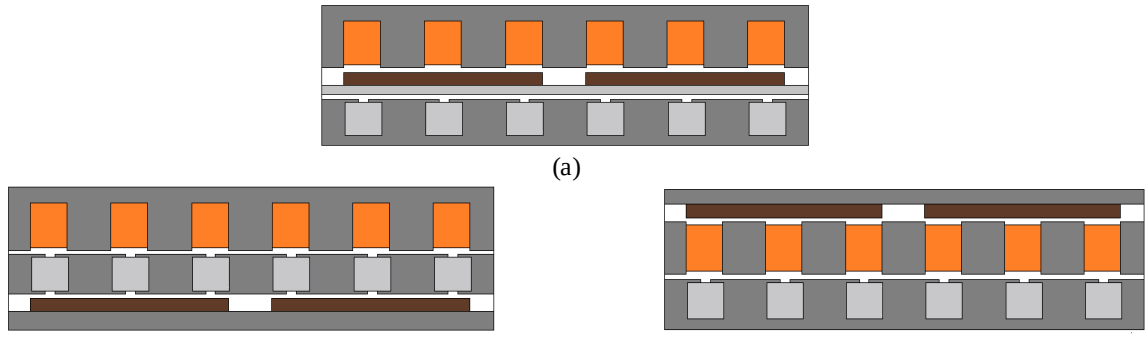

(a)

(b) (c)

Figure 2.3: Different PMIG configurations with (a) PM-rotor between IG cage and stator, (b) IG cage between PM-rotor and stator and (c) stator between IG cage and PM-rotor.

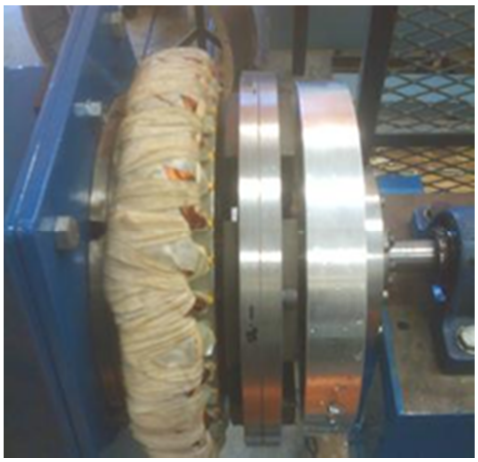

Figure 2.4: Example of an axial flux PMIG with PM-rotor between the cage and stator.

(a) (b) (c)

Figure 2.5: (a) Cross section of proposed implementation of the PM-rotor, with (b) the cage-rotor to be modified and (c) the conventional 9 kW IG to be converted to a PMIG.

Table 1: Parameters of the unmodified IG.

PARAMETER	VALUE	UNIT	PARAMETER	VALUE	UNIT
Stator outside diameter, D_o	210	mm	Rated torque, T_{gr}	30	Nm
Stator inside diameter, D_i	116	mm	Rated output power, P_{gs}	9	kW
Rotor outside diameter, d_o	114.9	mm	Operating voltage,V_1	440Δ /690Y	V
Rotor inside diameter, d_i	48	mm	Rated current,I_1	16.88 Δ / 9.74	A
Axial length of core,l_1	105	mm	No load current, I_m	6	A
Number of stator slots, S	30		Rated speed, n_r	2870	r.min^{-1}
Number of rotor slots, R	26		Synchronous speed, n_s	3000	r.min^{-1}
Number of poles, p	2		Operating frequency, f_1	50	Hz
Number of turns per coil, N_s	33		Power factor at full load PF	0.89	
Stator resistance, R_1	1.194	Ω	Efficiency at full load, η_t	86.3	%

2.4 FE design and analysis

In this section the FE design process followed to obtain an experimental PMIG design is dealt with. The aim was to keep the design process as simple as possible, as the only interest is the basic working characteristics of the machine from a practical perspective.

2.4.1 FE design approach

It would be insightful to analyse the unmodified IG of Table 1 first. It is deemed adequate to evaluate the no-load characteristics of the machine only. Three no-load output parameters are identified for FE analysis: the per phase flux linkage (λ_1), the phase voltage (V_1) and the air gap flux density (B_g). These parameters can be calculated by means of FE analysis by exciting the stator coils of the unmodified IG with the rated no-load magnetizing current.

By means of a second FE analysis the modifications added to incorporate the free rotating PM-rotor are taken into account. The final PMIG system obtained should match the no-load characteristics of the unmodified IG, i.e. with regard to λ_1, V_1 and B_g. Fig. 2.6 shows the FE field plots of the unmodified IG as well as of the modified PMIG. To obtain a PM design from FE analysis in as little as possible time, a very basic, iterative design process is followed.

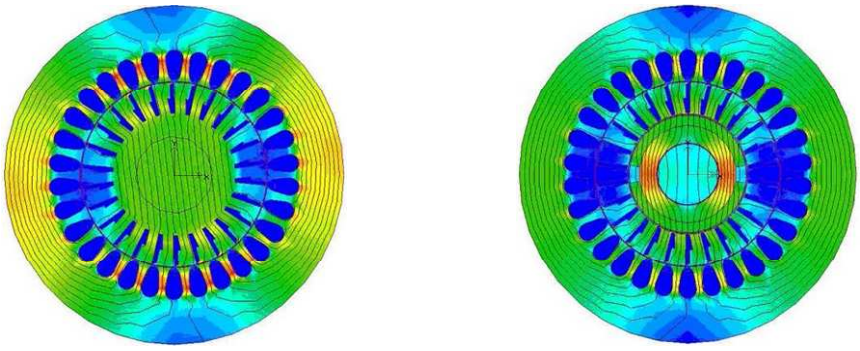

(a) (b)

Figure 2.6: (a) FE field plot of the unmodified IG and (b) IG with the PM-rotor incorporated.

Table 2 gives the design iterations followed, with the variable parameters being magnet height (h_m), magnet pitch to pole pitch ratio (σ_m) and the size of the secondary air gap between the cage-rotor and the PM-rotor (δ_2). All other machine parameters are kept fixed throughout the design process. The only other parameter added is a third air gap (δ_3), between the PM-rotor shell and the shaft. The mechanical tolerance is specified to ensure that the PM-rotor rotates absolutely freely on the main shaft, ensuring that it will always operate synchronously with the rotating stator field.

Nine simulations are iteratively done for different values of h_m and σ_m. The air gap δ_2, is varied slightly as well, but fixing δ_2 at 1 mm seems adequate. These small air gap variations have little effect on the overall machine performance, because δ is already considerably enlarged by including permanent magnets in the design. Specifying δ_2 at 1 mm also allows adequate space for a bandage to be applied to the magnets. For the 50 Hz 2-pole machine the PM-rotor rotates at a synchronous speed of 3000 r/min and a segmented magnet configuration is used as shown in Fig. 2.7. It is of extreme importance that the magnets are sufficiently fixed to the cylindrical shell it is located upon.

From Table 2 it is evident that the 2-pole machine is saturated to a large extent. An increase in magnet strength by increasing h_m does not improve the overall machine performance. This is due to a large amount of flux being forced into a small area if the PM-rotor is situated inside the cage rotor. From Table 2 the configuration selected is simulation-2, with h_m= 6 mm, σ_m = 0.73 and δ_2 = 1 mm.

Table 2: FE design iterations.

SIM	I_m (A)	h_m (mm)	σ_m (pu)	δ_2 (mm)	λ_{1peak} (Wb.t)	V_{1peak} (V)	B_{gpeak} (T)
1	6	0	0	0	1.657	372	0.86
2	0	6	0.73	1	1.247	260	0.67
3	0	6	0.78	1.2	1.140	255	0.67
4	0	6	0.9	1.2	1.356	253	0.69
5	0	6	0.9	1	1.385	258	0.7
6	0	6	0.97	1	1.424	253	0.72
7	0	8	0.9	1	1.415	264	0.73
8	0	8	0.9	0.8	1.448	270	0.73
9	0	10	0.9	0.8	1.448	270	0.7

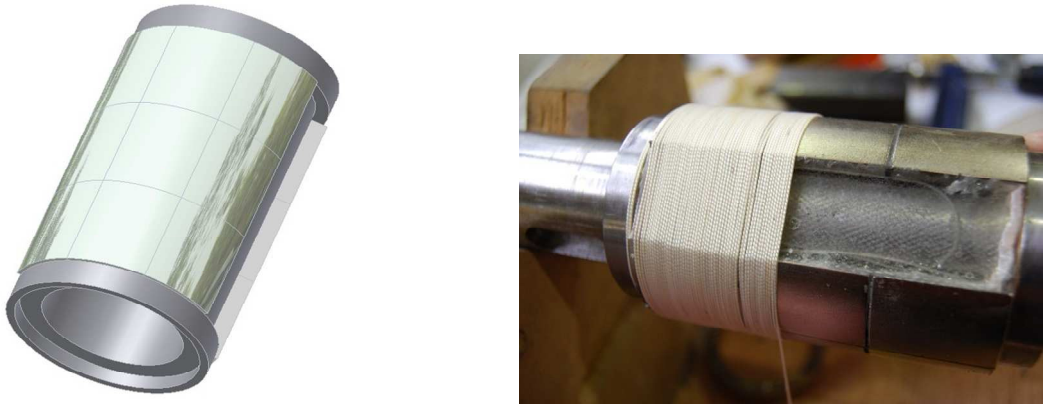

(a) (b)

Figure 2.7: (a) Assembled magnet configuration with (b) a bandage being applied.

Fig. 2.8 shows some of the different components of the new double rotor configuration incorporated within the conventional induction machine. Fig. 2.8(a) shows the machined cage in which the cylindrical shell shown in (b) with the PMs should fit. Fig. 2.8(c) shows the completed PM cylindrical shell mounted on the main shaft by means of a second set of bearings that allows it to rotate freely on the main shaft. Finally in Fig. 2.8(d) the PM-rotor shell is fixed within the cage. A new set of end rings are manufactured to fix the cage to the main shaft.

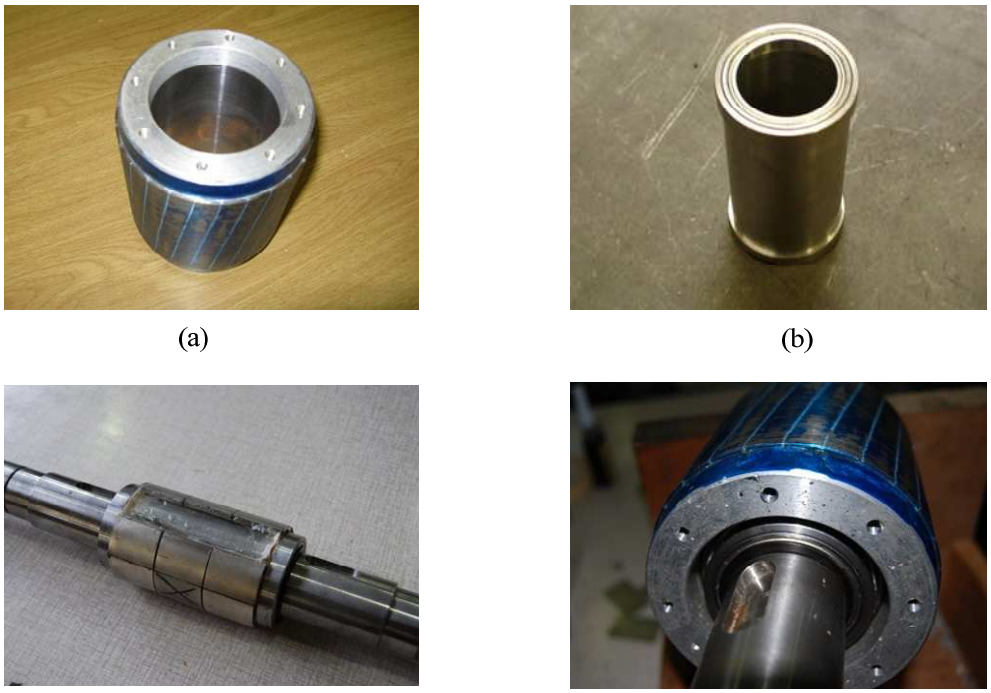

(a) (b)

(c) (d)

Figure 2.8: (a) Modified induction machine cage rotor; (b) PM cylindrical shell; (c) PM-rotor mounted on the main shaft; (d) PM-rotor assembled within the cage.

2.4.2 FE calculated results of the IG and PMIG

Fig. 2.9shows the per phase flux linkage and induced voltage for the unmodified IG and for the modified PMIG, in each case plotted against the electrical angle (θ_e). Fig. 2.10 shows the air gap flux density and its fundamental component for the IG and the PMIG.

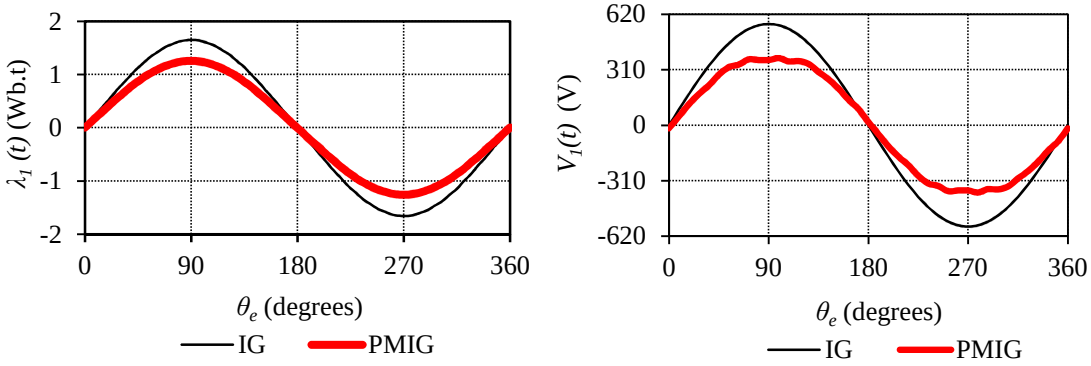

(a) (b)

Figure 2.9: FE calculated (a) per phase flux linkage and (b) per phase induced voltage for the magnetizing current excited unmodified IG and for the PM-excited modified PMIG versus electrical angle at 50 Hz.

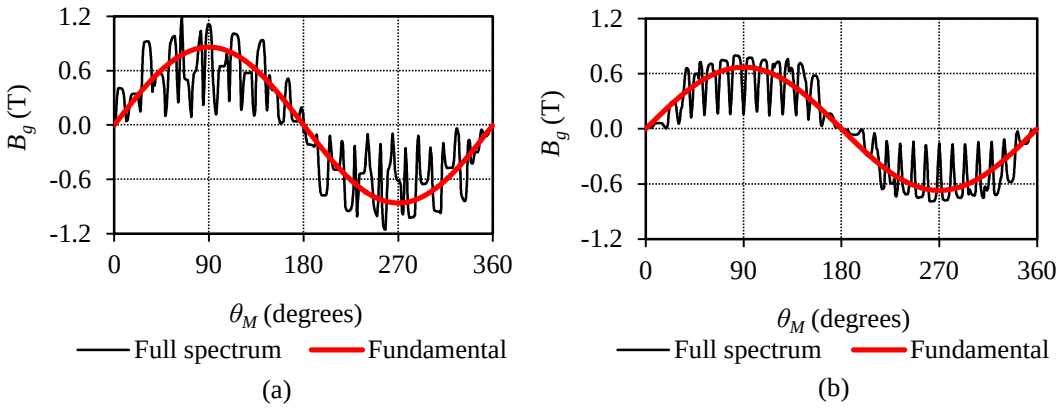

Figure 2.10: Flux density in the air gap together with its fundamental for (a) the unmodified IG and (b) the PMIG versus mechanical angle.

As in Table 2 it is seen from the FE results that it is impossible with the current 2-pole machine configuration to obtain the required output-parameter-matching regarding λ_1, V_1 and B_g.

2.5 Measured Results

To compare FE results with measured results, Fig. 2.11shows the FE-predicted and measured open circuit PMIG voltages. The measured grid voltage is also given as a reference. The PMIG no-load voltage is measured as 274 V_{rms}, which is about 70 % of the required grid voltage of 400 V.

It is known from the reviewed literature and from (2.8) that for the best performance of the PMIG the internally induced PM voltage should match the grid voltage. To match the grid voltage with the PMIG voltage of Fig. 2.11, the machine is connected to a variable voltage source by means of a three-phase variac. With the variable voltage source the effects of operating the PMIG at different values of V_1 than the rated value of E_1 can also be investigated. Tests at four voltage values 100 V, 200 V, 274 V and 400 V are used to characterise the performance of the PMIG. In each case the performance of the PMIG is compared with the conventional unmodified IG.

For the four mentioned voltage values Fig. 2.12 gives the output power (P_{gs}) against slip for both machines. The efficiencies and power factors of both machines are shown in Fig. 2.13 and Fig. 2.14 respectively.

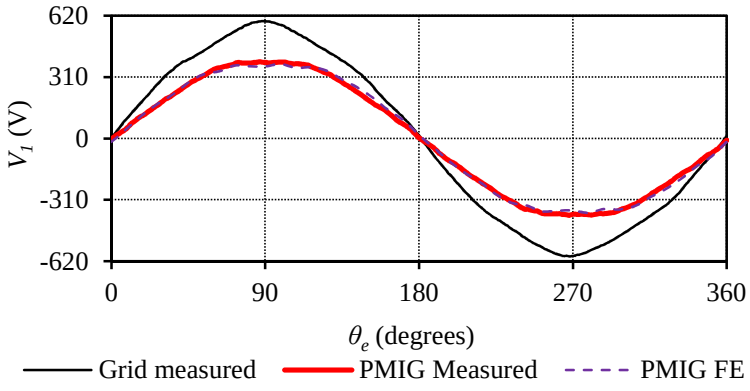

Figure 2.11: FE-predicted and measured PM open circuit induced voltage as well as the measured grid voltage plotted against electrical angle.

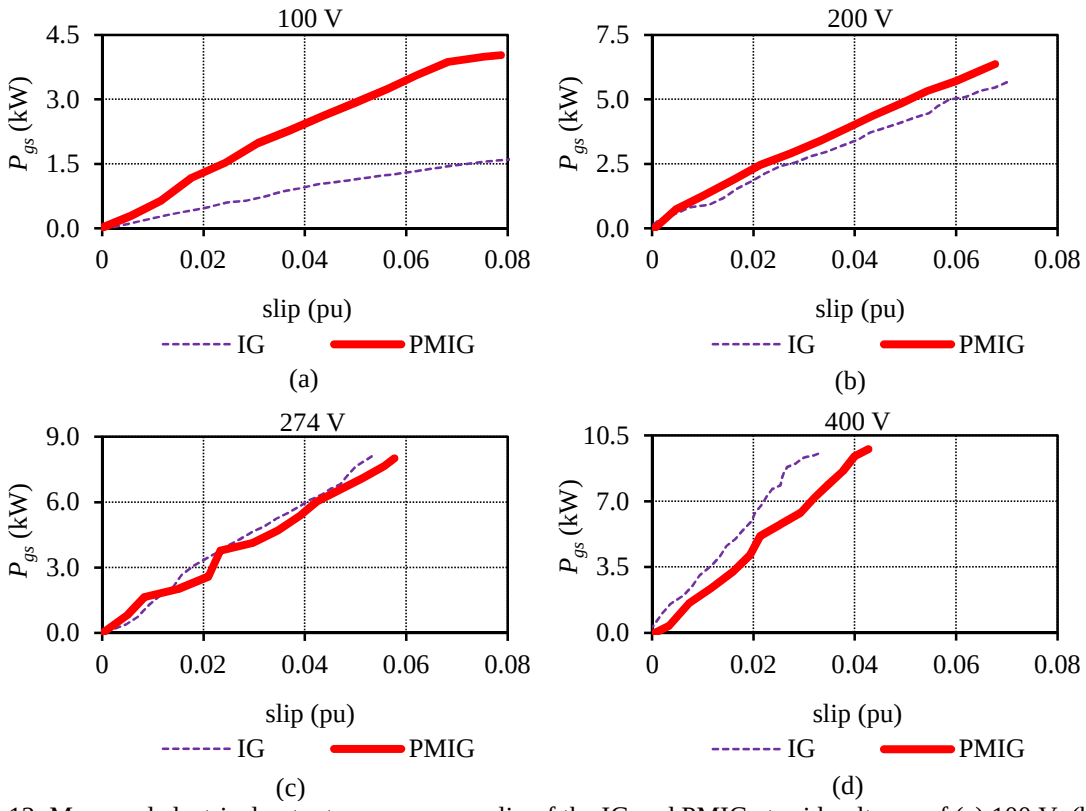

Figure 2.12: Measured electrical output power versus slip of the IG and PMIG at grid voltages of (a) 100 V, (b) 200 V, (c) 274 V and (d) 400 V.

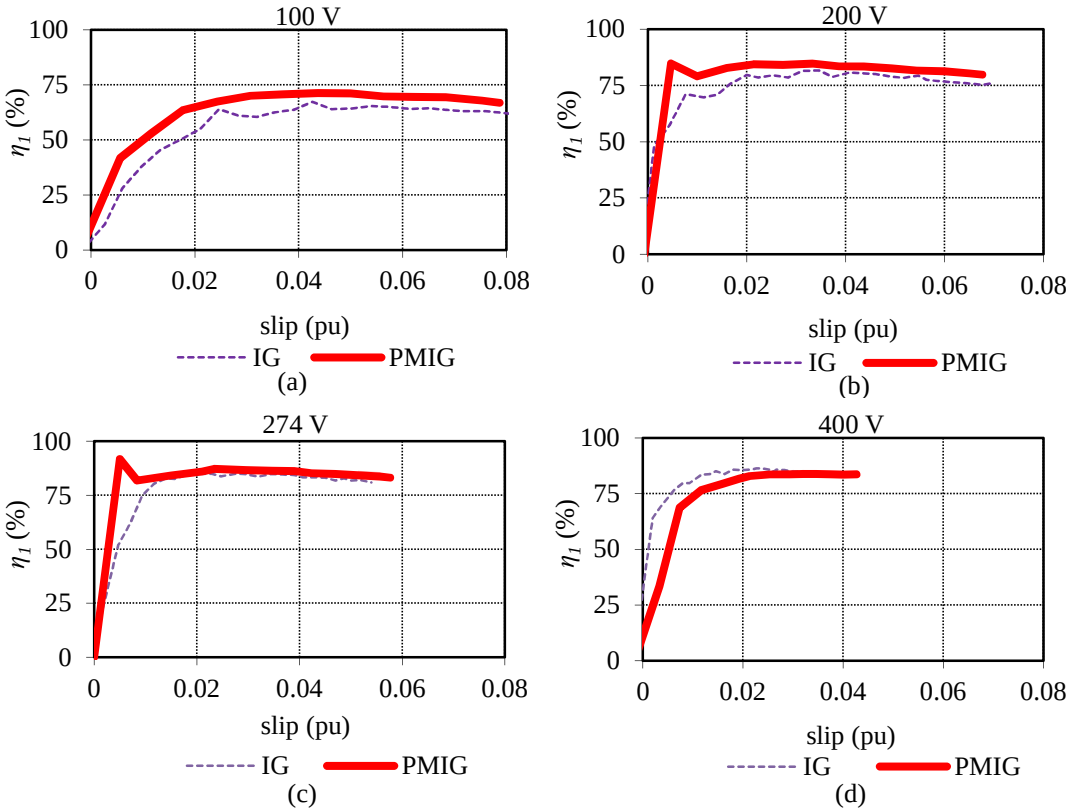

Figure 2.13: Measured efficiency versus slip of the IG and PMIG at grid voltages of (a) 100 V, (b) 200 V, (c) 274 V and (d) 400 V.

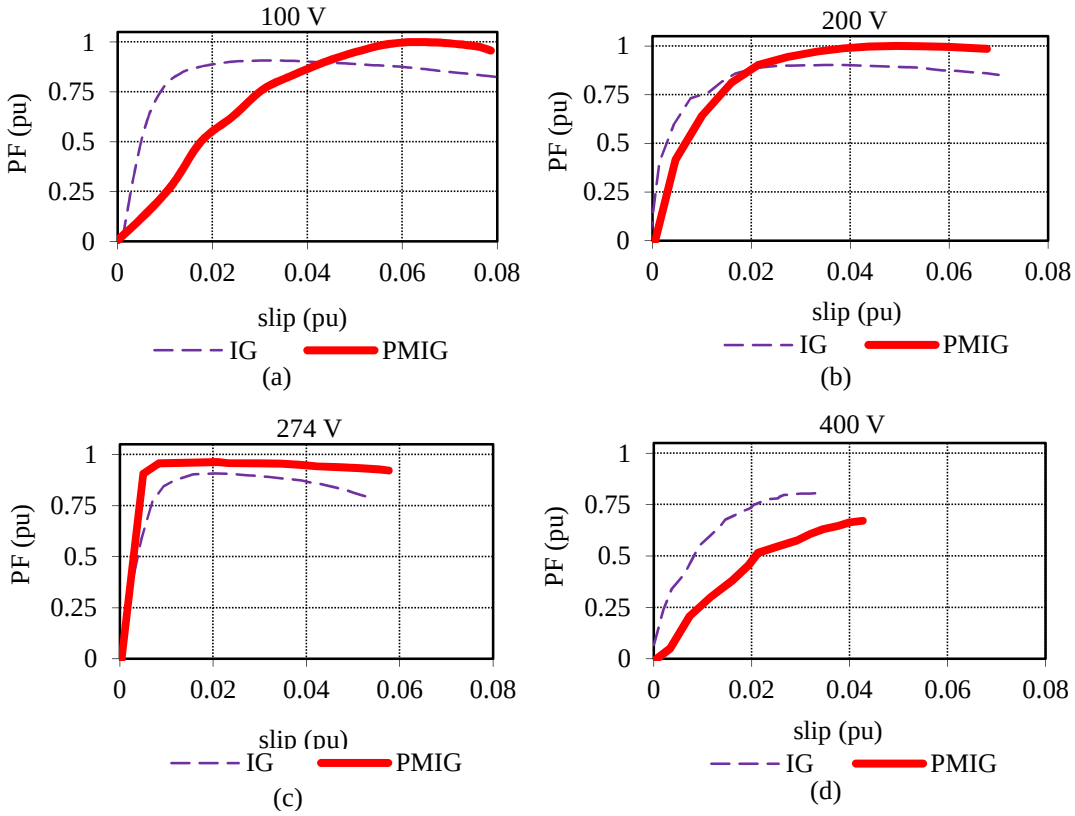

Figure 2.14: Measured power factor versus slip of the IG and PMIG at grid voltages of (a) 100 V, (b) 200 V, (c) 274 V and (d) 400 V.

From the results in Figs. 2.12 to 2.14 it can be seen that the PMIG performs better than the IG at lower voltage levels. Especially regarding the power factor a significant improvement is observed compared to the standard unmodified IG. The reactive power demand of the PMIG with a variation in V_1 can be explained by Fig. 2.15. In Fig. 2.15, at a voltage of 274 V the magnetizing current is reduced to zero, in turn reducing the reactive power demand to zero, thus explaining the improved power factor. When operating the machine at voltages less than 274 V, reactive power is delivered to the grid and above 274 V reactive power is drawn from the grid.

If the operating voltage differs from 274 V the magnetizing current of the PMIG rises sharply. This can be explained by (2.1) knowing that X_m is inversely proportional to the equivalent air gap δ. By adding the PM-rotor to the IG, the air gap is considerably enlarged. This is shown in (2.9) as

$$\delta = \delta_1 + \delta_2 + h_m . \tag{2.9}$$

For the original IG

$$\delta = \delta_1 = 0.55 \text{ mm} . \tag{2.10}$$

For the PMIG

$$\delta = 0.55 + 1 + 6 = 7.55 \text{ mm} . \tag{2.11}$$

This amounts to an increase in the air gap length of

$$\frac{\delta_{PMIG}}{\delta_{IG}} = \frac{7.55}{0.55} = 13.73. \tag{2.12}$$

This effect can clearly be seen in Fig. 2.15(a), where I_m of the PMIG has a much steeper curve than I_m of the unmodified IG. Fig. 2.15(b) gives the no-load reactive power demand of the IG and the PMIG.

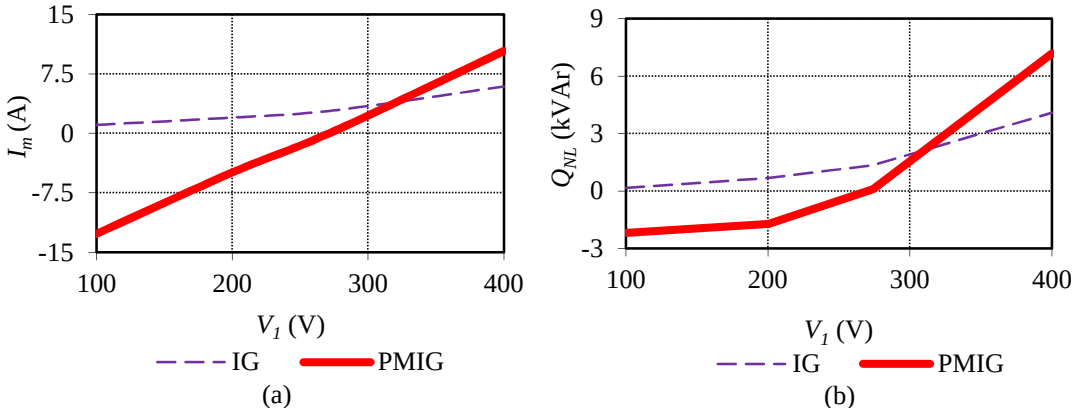

Figure 2.15: (a) Magnetizing current and (b) no-load reactive power demand of the IG and the PMIG versus grid voltage.

From (2.8) and all simulation and practically measured results it is clear that the most suitable operating point for the PMIG is at a terminal voltage of 274 V. Although the rated operating point of the unmodified IG is specified as 400 V and 9 kW it would be unfair to judge the performance of the PMIG at this point. A more legitimate comparison is made at a terminal voltage of 274 V and a reduced power level specified for both the IG and PMIG.

If a modification was possible to accommodate a PM configuration capable of providing the required air gap flux density, the performance of the PMIG would probably have been better than that of the conventional IG at the 400 V operating point as well. In this regard the modification of a higher pole IG to a PMIG would have given better results, especially if the PM-rotor was placed inside the cage rotor.

Stability and torque ripple

The PMIG mostly responds in a stable way to load changes being applied. Oscillatory behaviour was only observed during measurements at low slip values. This might be caused by the cogging torque effect between the PM-rotor and the cage-rotor. Although the cage-rotor is skewed, this only allows for a reduced cogging coupling with the stator. Fig. 2.16 shows the FE-predicted no-load cogging torque coupling, without skewing taken in to account for two operating cases. A first rotation rotates the PM-rotor and the cage-rotor at the same speed (zero slip), which simulates the cogging coupling with the stator. A second rotation rotates the cage-rotor and the PM-rotor at different speeds, thus at a relative slip speed with respect to each other. From the second rotation the cogging between the cage-rotor and PM-rotor can be estimated.

The peak to peak no-load cogging torque between the cage and the PM-rotor is predicted from FE as 1.24 Nm. This gives a per unit cogging torque of 0.04 pu (4%), if the rated torque value of 30 Nm is taken as the base value. It should also be noted that the cogging torque is usually more in a practical system due to manufacturing imperfections.

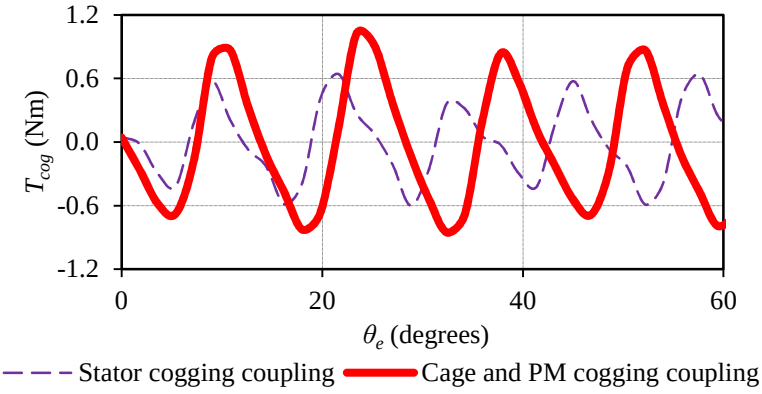

Figure 2.16: FE predicted cogging torque between the PM-rotor and stator as well as between the PM-rotor and cage versus electrical angle.

Fig. 2.17 shows a current response for a torque input step to the PMIG. The step results from a slip variation of 1 to 3 % by the drive system for the 274 V grid-connected PMIG. Some transient effects occur shortly after the step is applied, but as seen from Fig. 2.17 it is possible to obtain stability within a relatively short time. It should be noted that only the average torque and average current data is displayed in Fig. 2.17.

To shed some more light on the oscillatory behaviour at lower slip values, Fig. 2.18 shows the measured torque ripple at the lower slip operating region of the PMIG. This torque ripple is quite high at 5.5 Nm peak to peak which is 18.3 % of the rated torque value of 30 Nm. At zero slip almost no ripple is measured on the entire drive train and the high ripple values of Fig. 2.18 only occur as the machine starts to slip.

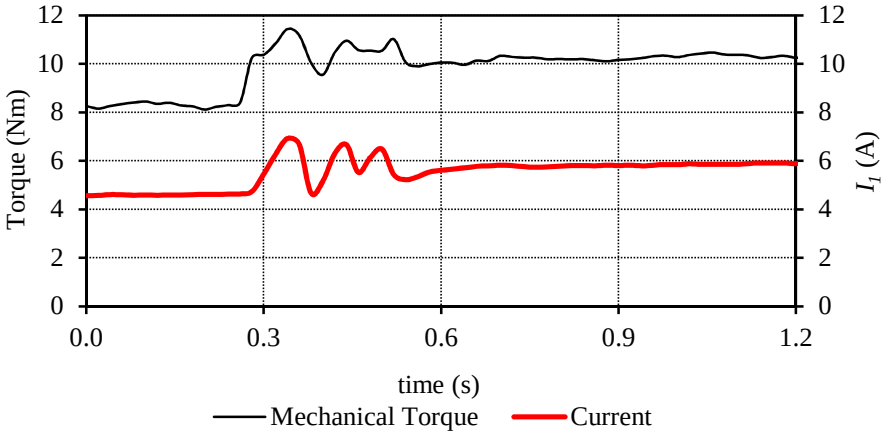

Figure 2.17: Average mechanical input torque step and the resulting average RMS current response plotted against time.

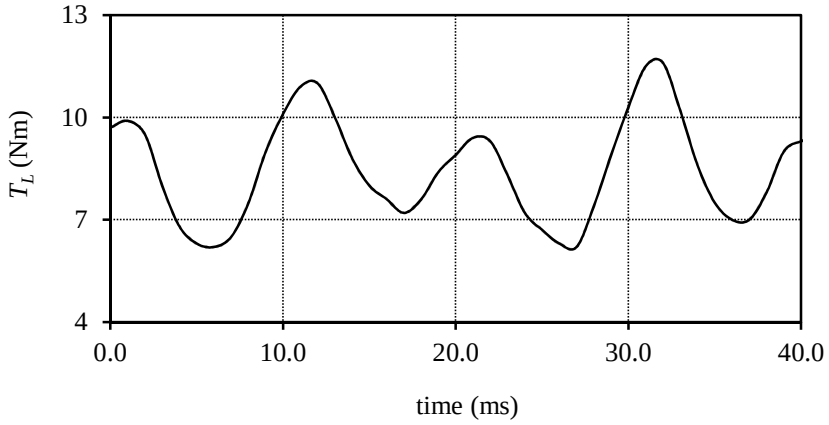

Figure 2.18: Measured torque ripple versus time at the lower slip operating region.

2.4 Summary and conclusions

Valuable knowledge is gained regarding the behaviour of the conventional coupled C-PMIG from this first experimental study. The performance of this machine is found to be consistent with the results obtained in the studied literature.

Several advantages and disadvantages are identified for the use of this machine type. One of the key advantages of the PMIG is the improved power factor over a conventional induction machine. However, to ensure the best performance of this machine type it is important for the grid voltage and internally induced PM voltage to match. The permanent magnets should be designed in order to support the required flux density in the air gap sufficiently. If this is possible it is expected that the PMIG will have a much better overall performance than the conventional IG.

The largest drawback of this machine is the constructional difficulties, which could hamper the implementation of the optimum machine structure. This can be observed from the experimental prototype under discussion, especially regarding the eventual placing of the permanent magnets. For a machine modification as done in this instance it might have been better to use an axial flux machine. An axial flux machine allows for more freedom regarding the placement of the PM-rotor, without altering the overall machine structure. A higher pole machine might have given better results for the same modification method as used in this case.

Observed as well, is the cogging torque issue which came into effect at low slip speeds. Although the cage rotor is skewed, cogging effects between the two rotors are still an issue. Methods should thus definitely be introduced in future studies to reduce this effect.

Finally, from this experiment the same conclusion can be drawn as from the reviewed literature, namely that this machine type definitely has potential for further implementation, especially for machines with higher pole numbers.

Chapter 3 – Split-PMIG: Design of the SG

With the design of the S-PMIG of which the equivalent circuit is shown in Fig. 3.1(a) divided into two modular units, the design of the SG unit based upon the equivalent circuit as shown in Fig. 3.1(b) is dealt with in this chapter. The design of the SG unit can be approached in the same manner as for a normal direct-drive PMSG.

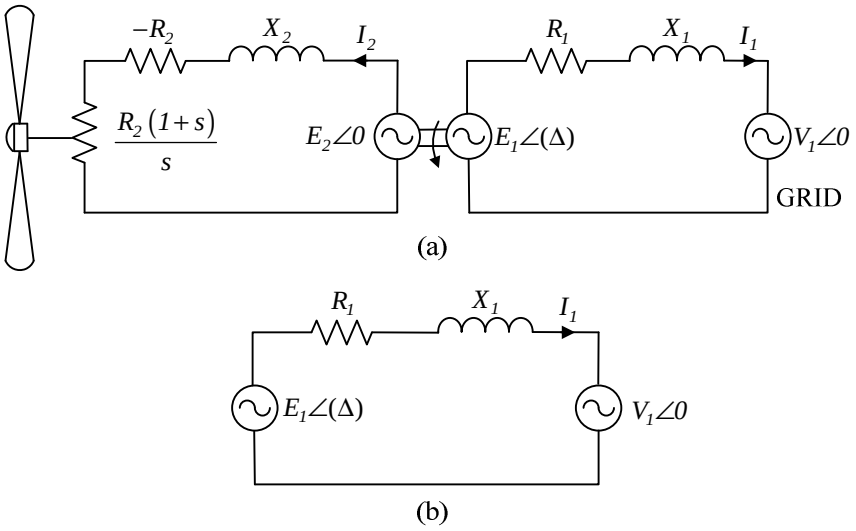

Figure 3.1: (a) S-PMIG equivalent circuit with (b) the SG unit equivalent circuit as used in this chapter.

3.1Machine design and simulation tools

For all design purposes a non-commercial FE program, which has an optimising procedure incorporated [33] and [34], is used. This FE software has several advantages over its commercial counterparts. It has a powerful optimising algorithm as well as an adaptive FE mesh program which eases the implementation of varying machine structures. To verify the results obtained from the non-commercial FE program, a commercial FE simulation package is also used to compare final machine performances.

3.1.1 Optimising algorithm

The optimising procedure as explained in [34] makes use of the direction set method of Powell [35] and the quassi-Newton gradient method [36]. These optimisation procedures are used directly with a FE model of the machine as shown in Fig. 3.2. Of the two mentioned optimisation methods, Powell's method was chosen. Although [34] finds the quassi-Newton method to be faster, no derivatives are required for Powell's method.

In the optimisation program as shown in Fig. 3.2, **Y** is the output performance parameter of the machine, e.g. the machine torque (T_{gs}) or the efficiency (η_1), with

$$\mathbf{Y} = \mathrm{F}[\mathbf{X}] \tag{3.1}$$

being maximised or minimised as a function of the multidimensional vector [**X**]. Contained in [**X**] are all the variable machine parameters which need to be optimised. With each iteration of *r* the algorithm determines the optimum search directions for [**X**] in a multidimensional space along which **Y** is minimised or maximised. Each time the FE program is called, a new mesh is generated based on the changed input dimensions included within [**X**].

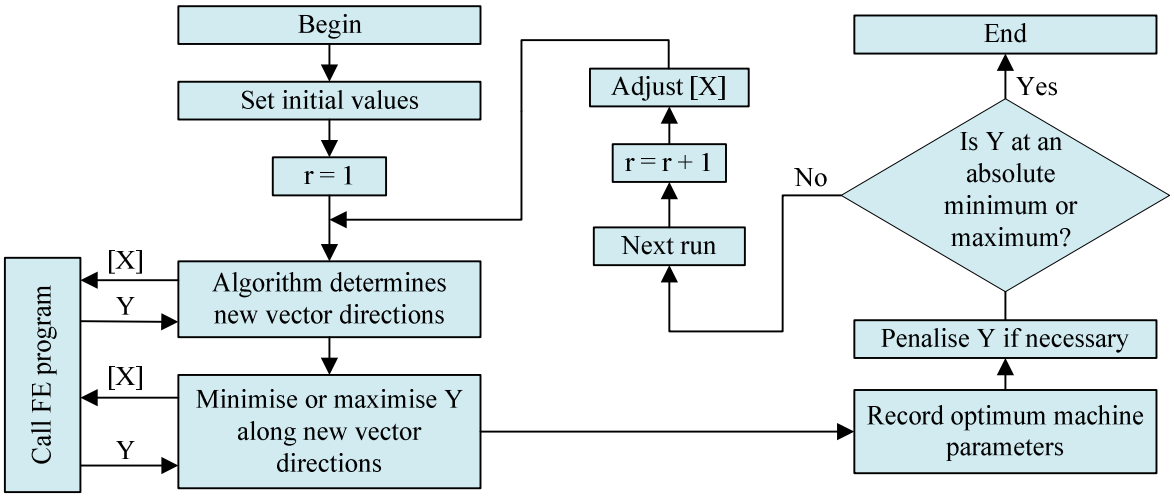

Figure 3.2: Optimisation algorithm with FE program incorporated [34].

To contain the parameters indicated by [**X**] within realistic boundaries, penalty functions are included in the design algorithm. The same can also be done for **Y**, by specifying certain constraints on for instance η_1 and T_{gs} to obtain the required machine performance. If these boundaries are violated the objective function, (F[**X**]), is penalised by

$$\mathrm{F}\left[\mathbf{X}, w\right] = \mathrm{F}[\mathbf{X}] - \sum_{i=1}^{n} w_i \varepsilon_i \,, \tag{3.2}$$

with the penalty function (ε) specified as,

$$\varepsilon = \begin{cases} 0 & : \; x \le x_0 \\ \left(x_0 - x\right)^2 & : \; x \ge x_0 \end{cases} \,. \tag{3.3}$$

In (3.3) x is a dimensional or performance parameter value violating the specific boundary (x_0) specified for the particular parameter. Although the value of ε will increase exponentially with continuous boundary violations, it might be necessary to adjust the weighting factor (w) to effectively address boundary violations.

3.1.2 FE modelling

The machine modelling in this chapter is done in the steady-state and in the *dq* reference frame fixed to the rotor. The steady state approximated *dq* equivalent circuits are shown in Fig. 3.3(a) and (b) with positive current taken as flowing out. The current and voltage relationships are shown in the vector diagram of Fig. 3.3(c).

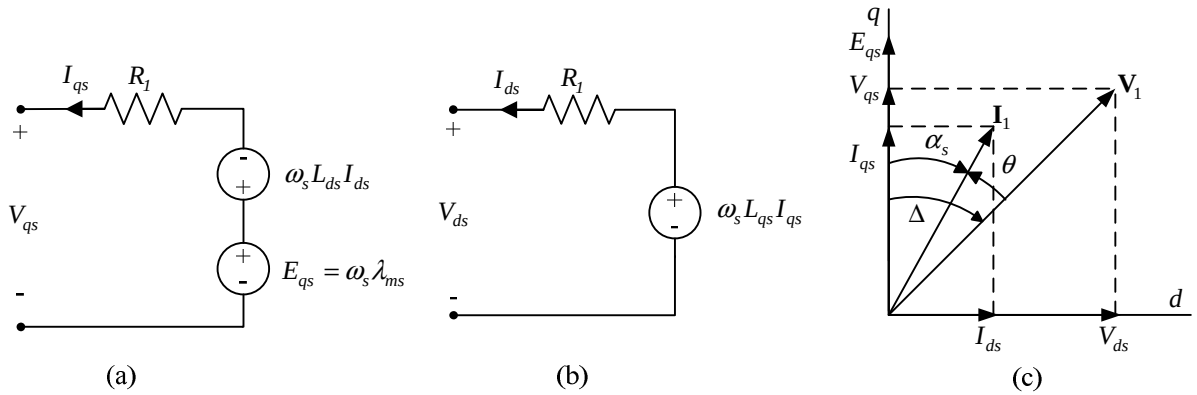

Figure 3.3: Steady-state *dq* equivalent circuits with (a) *q*-axis and (b) *d*-axis equivalent circuits and (c) current and voltage vector diagram.

V_{ds} and V_{qs} are the respective stator *d*-axis and *q*-axis voltage components for which the steady-state equations are given by,

$$V_{qs} = -R_1 I_{qs} - \omega_s L_{ds} I_{ds} + \omega_s \lambda_{ms}; \quad V_{ds} = -R_1 I_{ds} + \omega_s L_{qs} I_{qs}. \tag{3.4}$$

R_1 in (3.4) is the stator winding resistance per phase, and $\omega_s = 2\pi f_1$ gives the synchronous electrical speed, with $f_1$being the operating frequency. The *q*-axis and *d*-axis inductances used in Fig. 3.3 and (3.4) are given by

$$L_{qs} = \frac{\lambda_{qs}}{-I_{qs}}; \quad L_{ds} = \frac{\lambda_{ds} - \lambda_{ms}}{-I_{ds}}, \tag{3.5}$$

with λ_{ds}, λ_{qs} and λ_{ms} being the *dq*-axis and PM flux linkages respectively and I_{ds} and I_{qs} the stator *d*- and *q*-axis currents.

The angles used in the vector diagram in Fig. 3.3(c), are the load angle (Δ), the current angle (α_s) and the power factor angle ($\theta = \Delta - \alpha_s$). From the vector diagram the relationships for the voltage and current is given in (3.6) - (3.8) with

$$V_{qs}^{\ 2} + V_{ds}^{\ 2} = 2V_{1rms}^{\ 2}; \tag{3.6}$$

$$I_{qs}^{\ 2} + I_{ds}^{\ 2} = 2I_{1rms}^{\ 2}. \tag{3.7}$$

$$\begin{bmatrix} V_{qs} \\ V_{ds} \end{bmatrix} = \sqrt{2} V_{1rms} \begin{bmatrix} \cos\Delta \\ \sin\Delta \end{bmatrix}; \quad \begin{bmatrix} I_{qs} \\ I_{ds} \end{bmatrix} = \sqrt{2} I_{1rms} \begin{bmatrix} \cos\alpha_s \\ \sin\alpha_s \end{bmatrix}. \tag{3.8}$$

The stator current (I_1) and the current density (J_s) can be calculated if the copper loss for the machine (P_{cus}) is known with,

$$I_{1rms}^{\ 2} = \frac{P_{cus}}{3R_1} \tag{3.9}$$

and

$$J_s = \frac{I_{1rms}}{a a_{scs}}. \tag{3.10}$$

where a_{sc} is the active copper slot area for the stator winding and *a* is the amount of parallel circuits. If the *dq* currents and flux linkages are known the developed torque of the PM machine can be calculated from (3.11) as

$$T_{gs} = \frac{3}{4} p[(L_{qs} - L_{ds}) I_{ds} I_{qs} + \lambda_{ms} I_{qs}]. \tag{3.11}$$

The efficiency of the generator is then given by,

$$\eta_1 = \frac{T_{gs}\omega_{sm} - \left(P_{ecs} + P_{wfs}\right) - P_{cus}}{T_{gs}\omega_{sm}}. \tag{3.12}$$

P_{ecs} is the eddy current and core losses of the machine, which include the eddy current losses in the rotor yoke and permanent magnets. The stator core losses are calculated by means of an empirical formula using the air gap flux density data from FE analysis, while the eddy current losses in the magnets and PM yoke are determined from FE transient loss calculations as done in [37] and [38]. P_{wfs} is the wind and friction losses of the machine, which are approximated at a fixed value as machine changes in the design optimisation will have minor effects on this parameter.

Finally the reactive and active power flow of the machine is given by (3.13) as

$$\begin{bmatrix} P_{gs} \\ Q_{gs} \end{bmatrix} = 3V_{1rms} I_{1rms} \begin{bmatrix} \cos\theta \\ \sin\theta^* \end{bmatrix}. \tag{3.13}$$

3.1.3. FE operation

To calculate the equivalent machine output parameters, the per phase resistance is calculated from the given slot dimensions in **X** and a predicted maximum winding operating temperature, T_c. The machine current is then calculated from (3.9) by specifying a value for P_{cus}. When specifying P_{cus}, J_s as given in (3.10) should be kept below a certain threshold which corresponds to the cooling capacity of the generator.

To obtain the correct operating point of the machine the current angle, α_s needs to be known as well, this parameter can either be specified if the machine is under converter current control, or needs to be calculated if the machine operates directly connected to a grid. With I_1 and α_s known, FE analysis is used to calculate the three phase flux linkages (λ_{abc}).

As all machine modelling is done in the *dq* reference frame, the FE calculated flux linkages are transformed to the *dq* reference frame by means of Park's transformation ($\mathbf{K_s}$) as,

$$\left[\lambda_{dq}\right] = [\mathbf{K_s}][\lambda_{abc}]. \tag{3.14}$$

The machine output parameters are calculated by solving (3.11) - (3.13) using (3.4) - (3.8). The block diagram shown in Fig. 3.4 gives a clearer explanation of the FE process as used in this case.

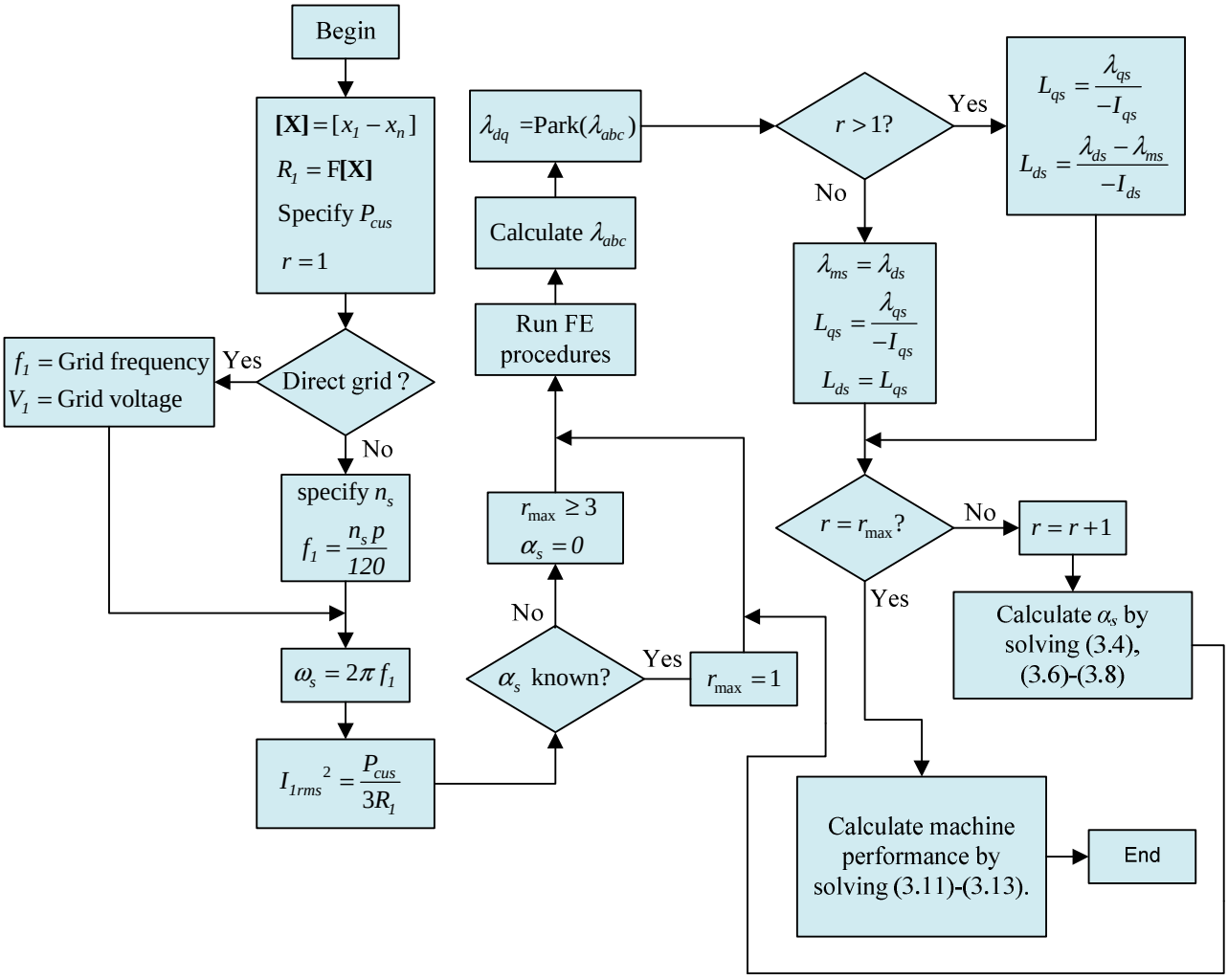

Figure 3.4: Working of the FE program to calculate machine performance parameters at the required operating point.

Due to the easier modelling, the FE design is done for the converter-fed system. In this particular case the current angle is specified as $\alpha_s = 0°$, which effectively reduces I_{ds} to zero. In this case the FE program only needs to be executed once and the machine output parameters are calculated as mentioned. For the modelling of the uncontrolled directly grid-connected system (3.4) to (3.9) need to be solved simultaneously in order to obtain the machine operating point. In this case more than one FE solution is needed.

For the directly grid connected case a first iteration is done as for the controlled system where the current angle is specified at $\alpha_s = 0°$ and I_1 is calculated as in (3.9). From this first FE iteration λ_{ms} is calculated with $\lambda_{ms} = \lambda_d$ in this case. To obtain more or less an operating point, V_d and V_q are solved as in (3.4) and Δ is obtained from (3.8). Also in this case it is assumed that $L_{ds} = L_{qs}$ and L_{qs} is calculated as in (3.5). With initial values for L_{ds} and L_{qs} as well as λ_{ms} known, I_{ds} and I_{qs} can be determined by solving (3.4) simultaneously and an initial value for α_s is predicted from (3.8). In this case (3.4) is solved, with new values for V_d and V_q calculated from (3.8), with the power angle Δ as previously obtained and V_{rms} in this case fixed to the grid voltage.

With this new operating point known for the machine another FE iteration is run. From this iteration new values for L_{ds} and L_{qs} are calculated as in (3.5). In this case L_{ds} and L_{qs} are not assumed the same. New values for I_{ds} and I_{qs} are calculated and a new value for α_s is specified, which provides a more accurate operating point. With all the required parameters known, (3.4) to (3.8) and (3.11) to (3.13) are solved in a third FE iteration to calculate the machine output performance. A fourth iteration can be executed for better accuracy, but for this design case three FE iterations are deemed adequate.

3.2 SG specifications and topology

In this section the specification of the SG design requirements and the selection of the optimum SG topology to comply with these requirements are dealt with.

3.2.1 Wind site and turbine specifications

The power curves for the turbine available are shown in Fig. 3.5. From these curves an optimum power level of 15 kW is selected. To select the most suitable turbine speed, information is needed on the specific wind sites where a system as such will be installed. It should be noted that a safe average operating speed of $n_t = 150$ r.min^{-1} is specified by the turbine manufacturer. It is not advisable to operate this specific turbine above this speed limit for long periods.

Fig. 3.6 shows the frequency of occurrence of the wind speed at two different wind sites. The PM machine design obtained from this study needs to perform adequately at both these wind sites. Site 1 [39], is an exceptionally good wind site with a very high average wind speed. Site 2 on the other hand has a significantly lower average wind speed. However, an average wind speed does not always give a clear indication of the best choice for the optimum turbine operating point. Figs. 3.7 and 3.8 give the annual energy contribution in kWh for the different wind speeds at Site 1 and Site 2, based upon the turbine power curves in Fig. 3.5. It is assumed for this turbine that the maximum turbine power is obtained at $v_w = 12.5$ m/s. For higher wind speeds the output power is clamped at the power output obtained at 12.5 m/s. From Fig. 3.7 for Site 1 it can be seen that the higher wind speeds in this case contribute to a higher annual energy yield. For Site 1 the optimum turbine speed would thus have been in the excess of 200 r.min^{-1}.However due to the limitations mentioned, operation at these speeds are not possible. Also from Fig. 3.8 it is seen that the higher wind speeds have a higher energy yield although less prevalent in Fig. 3.6. From Figs. 3.5 to 3.8 it is clear that a turbine speed of 150 r.min^{-1} is the most suitable choice. For the turbine speed region below the maximum allowed operating speed of 150 r.min^{-1}, variable speed operation is possible and maximum power point tracking can be done as shown in Fig. 3.5. For the higher wind speeds, with a maximum power output at a higher turbine speed, n_t is fixed at 150 r.min^{-1}.

The only other design requirement imposed by the turbine is the maximum allowable outside diameter of the machine to which the turbine is directly mounted. To avoid interference with the aerodynamic profile of the turbine rotor, the outside diameter of the machine is constrained at D_o = 670 mm.

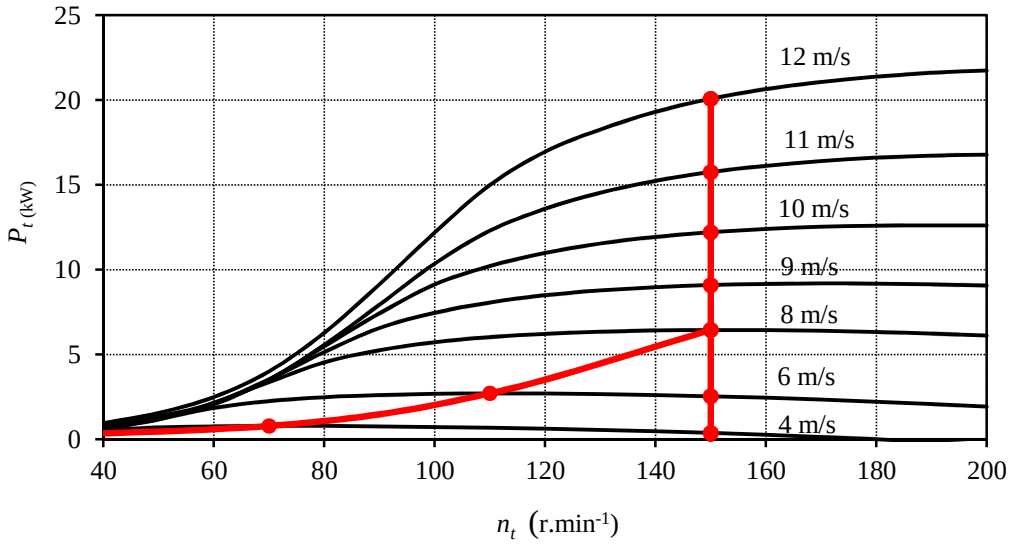

Figure 3.5: Turbine power curves with the proposed machine operating points.

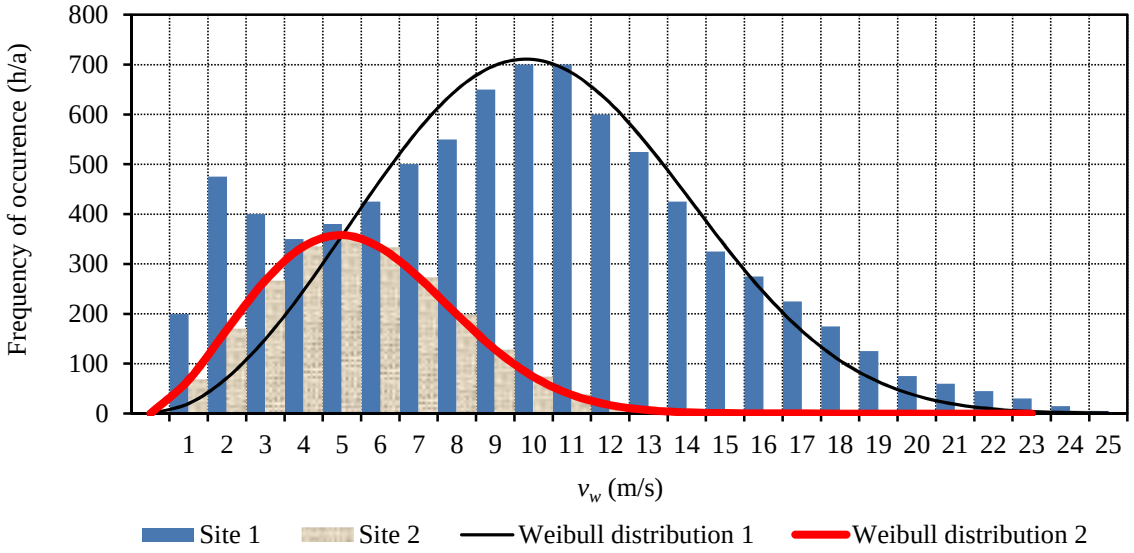

Figure 3.6: Wind speed distribution for two different wind sites.

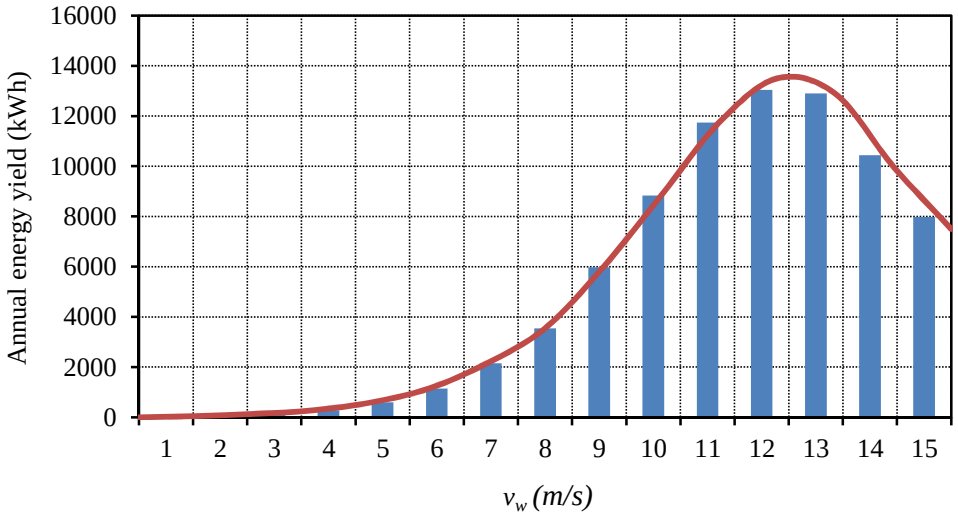

Figure 3.7: Annual energy yield calculated from Figs. 3.5 and 3.6 for Site 1.

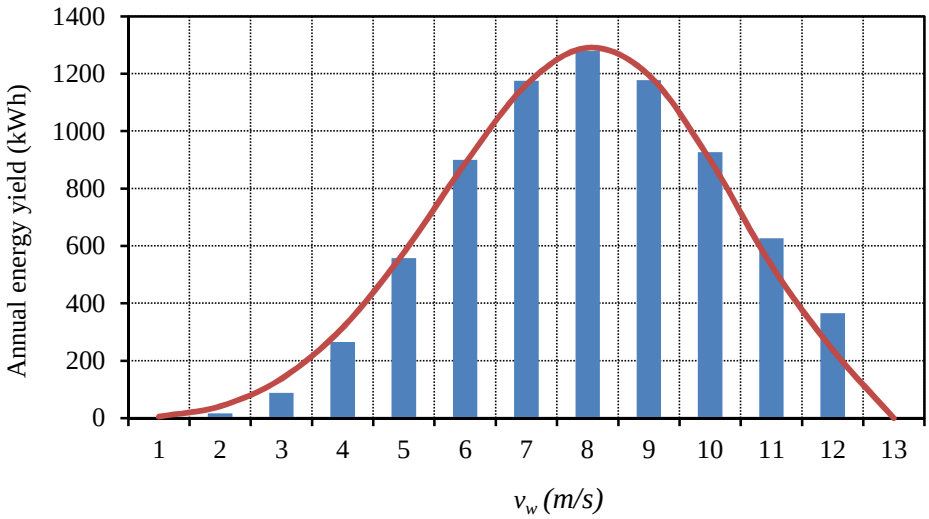

Figure 3.8: Annual energy yield calculated from Figs. 3.5 and 3.6 for Site 2.

3.2.2 Selecting the SG topology

With the design freedom obtained by axially separating the SG and IG, several choices are available for the type of machine to use for the SG unit. Basically any machine configuration can be used for the SG as long as it matches the rated torque and operating speed of the turbine. However in all direct-drive wind generator designs several aspects control the design process. These factors are cost, weight, maximum power output, ease of manufacturing, durability, as well as adequate quality of the machine's output parameters such as voltage and torque.

To improve the quality of the SG's outputs the voltage waveform should have a low harmonic content and the torque should be of high quality by having a low ripple content. Torque ripple can be a large source of vibration and acoustic noise in PM wind generators. A high enough cogging torque can also lead to the generator failing to start, as the wind turbine generates very low torque at low speeds. Cogging is thus identified as a very important design output parameter as stated in [40], where an analysis is done to investigate the effect of parameter changes on the cogging torque.

For the S-PMIG system it would be beneficial to have an easily constructible SG with a reasonable mass. This would lessen the impact of adding another direct-drive PM generator to the design by including the IG. To make the S-PMIG attractive for implementation within a wind generation setup, this generator must be presented as a low cost, easily constructible alternative to other wind generating systems.

Efficiency is important as well, because by using two PM machines in tandem, two efficiencies need to be multiplied. The overall efficiency needs to at least match or improve the efficiency of current wind generating systems. It should also be noted that the PMIG is a fixed speed system, which means that less energy will be harnessed at lower wind speeds. This further motivates the need for a more efficient generator configuration. It is however important to keep the overall machine mass increase to a minimum if the efficiency is to be improved.

The mentioned requirements lead to the selection of a non-overlap winding PM machine. Non-overlap winding machine topologies have a lower cogging torque and have fewer coils than the overlap winding PM machine. To reduce labour cost a single layer winding is proposed, which uses half the number of coils as opposed to double layer windings. A disadvantage of the single layer winding, however, is the large sub-MMF harmonic content. Furthermore if the slot lay-out of the machine is modified and if open slots are used, pre-formed coils can be used. Fig. 3.9 shows an example of preformed coils being used in a single layer non-overlap winding machine. By using preformed modular coils the winding and assembling process is simplified even more.

An evaluation is also done to investigate the economic and constructional feasibility of using solid rotor yokes and magnets in the design. In this study only a practical evaluation of these methods is done. Methods to reduce the losses in solid yokes and magnets are developed and investigated in [38].

It is also necessary to specify the optimum pole slot combination of the SG. The rated speed of the SG (n_s) is the same as the optimum turbine speed (n_t) selected in the previous section. With n_s= 150 r.min^{-1} known and the operating frequency specified as 50 Hz, the number of poles can be calculated from (3.15) as

$$p = \frac{120\, f_1}{n_s}\,. \tag{3.15}$$

From (3.15) p = 40, leading to three available, high winding factor, pole slot combinations which can be used for the required machine. These are the 40/36, 40/42 and 40/48 combinations as given in [41]. The 40/42 combination with only one winding section, W_s = 1, with W_s = gcd(p,Number of coils) and "gcd" the greatest common divisor as in [42], is discarded due to the unbalanced magnetic field in the air gap under load. The 40/36 combination also has a very low number of winding sections namely W_s= 2. The 40/36 combination, however, has a lower number of coils than for instance the 40/48 combination, but the ratio of the open-slot opening to the magnet pitch is larger, which is a disadvantage, and the winding factor is also lower. Another option with a low number of coils, if the turbine rated speed is slightly changed, is the 42/36 combination. The slot opening to magnet pitch ratio at no load of the 42/36 combination however is even worse than the 40/36 combination. The best option thus seems to be the 40/48 combination with W_s = 8. For this combination negative boundary conditions can be used in the FE program, which means only 5 poles and 6 slots need to be meshed [42].

Resulting from this discussion the final design specifications for the SG are summarised in Table 3.

(a) (b)

Figure 3.9: (a) Preformed coil being inserted; with (b) a complete single-layer non-overlap winding machine stator.

Table 3: SG design specifications.

Parameter	Value	Unit
Rated generator speed, n_s	150	r.min-1
Rated power, P_{gs}	15	kW
Rated torque, T_{gs}	1000	Nm
Operating frequency, f_1	50	Hz
Rated operating phase voltage, V_1	230	V
Number of poles, p	40	
Number of stator slots, S	48	
Maximum allowable machine outside diameter, D_o	670	mm

3.3FE design of the SG

In this section the focus is on the machine parameters to be optimised in the design and on the FE design optimisation of the SG.

3.3.1 Design optimisation parameters

The machine structure with the parameters to be optimised is shown in Fig. 3.10 and the parameters are summarised in (3.16). The machine is constrained volumetrically by keeping $D_o \leq 670$ mm and $D_i \geq 490$ mm and the axial length at $l_1 \leq 100$ mm.

$$\mathbf{X_1} = \begin{bmatrix} \sigma_m \\ \sigma_t \\ \sigma_g \\ h_r \\ h_s \end{bmatrix}; \quad \mathbf{X_2} = \begin{bmatrix} D_0 \\ D_i \\ l_1 \\ h_m \end{bmatrix}; \quad \mathbf{Y} = \begin{bmatrix} \tau_{ave} \\ \Delta\tau \end{bmatrix}. \tag{3.16}$$

In (3.16) h_m is the magnet height and h_r and h_s are the rotor and stator yoke heights respectively. The magnet pitch (θ_m), slot pitch (θ_t), and the slot width (θ_g) are expressed in pu values as in (3.17), with σ_m being the magnet pitch to pole pitch ratio, σ_t the slot pitch to the average slot pitch ratio, and σ_g the slot width to average slot pitch ratio.

$$\sigma_m = \frac{\theta_m}{\theta_P}; \quad \sigma_t = \frac{\theta_t}{\theta_S}; \quad \sigma_g = \frac{\theta_g}{\theta_S}, \tag{3.17}$$

where

$$\theta_S = \frac{2\pi}{S}; \quad \theta_P = \frac{2\pi}{p}, \tag{3.18}$$

and S is the number of stator slots.

The design output performance parameters are the per unit average torque, (τ_{ave}), and the per unit peak to peak cogging torque ($\Delta\tau$) with

$$\tau_{ave} = \left(\frac{T_{ave}}{T_{rated}} \right); \quad \Delta\tau = \frac{\Delta T_{cog}}{T_{rated}}. \tag{3.19}$$

T_{ave} and ΔT_{cog} are the average torque and the peak to peak no-load ripple torque respectively. T_{rated} is as specified in Table 3 at 1000 Nm. P_{cus} is initially set at 600 W, which allows for a current density of $J_s \leq 4$ A/mm^2, as well as a good efficiency.

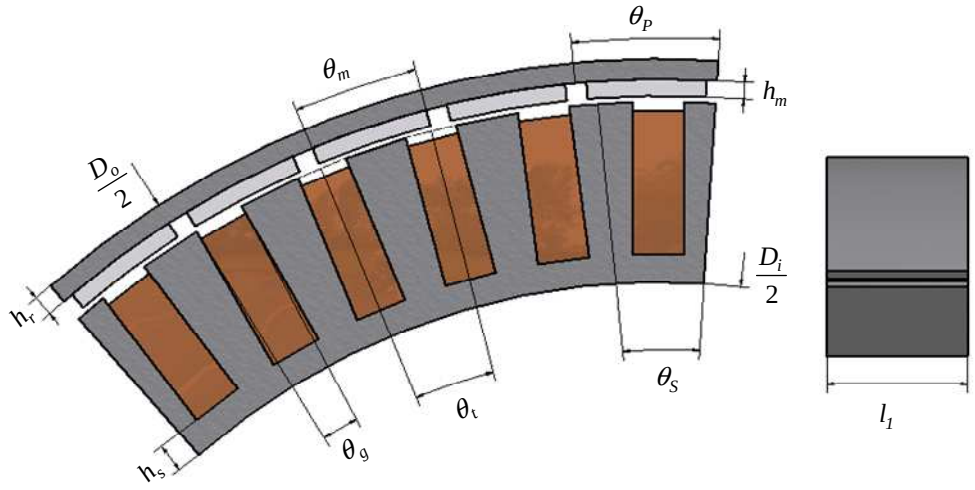

Figure 3.10: Machine section view with the design parameters for optimisation.

3.3.2 First design iteration

Fig. 3.11(a) shows the FE field plot for the used machine with the irregular paralleled slots to accommodate the preformed windings as shown in Fig. 3.9(a). Fig. 3.11(b) shows the FE field plot for an unmodified regular tapered slotted machine. The FE results from Fig. 3.11(b) are used for comparison reasons and to identify the effect of the irregular parallel slotting on the machine.

With the limits imposed upon the optimisation parameters as mentioned, a first design iteration focuses on the optimisation of $\mathbf{X_1}$ and $\mathbf{X_2}$ for the best average torque performance. The average torque is maximised, subject to the given copper loss of 600 W, by taking the objective function as

$$\mathbf{F}(\mathbf{X}) = \frac{\tau_{ave}}{P_{cus}}. \tag{3.20}$$

The results from this first optimisation are given in (3.21) as [see (3.16) for explanation]

$$\mathbf{X_1} = \begin{bmatrix} 0.98 \\ 1.00 \\ 0.53 \\ 14.0 \\ 8.00 \end{bmatrix}; \quad \mathbf{X}_2 = \begin{bmatrix} 667 \\ 496 \\ 100 \\ 6.00 \end{bmatrix}; \quad \mathbf{Y} = \begin{bmatrix} 1.13 \\ 0.26 \end{bmatrix}. \tag{3.21}$$

From (3.21) it is clear that the cogging torque is far too high at 26 % of the rated torque value. This high cogging torque definitely motivates a further design optimisation to minimise $\Delta\tau$.

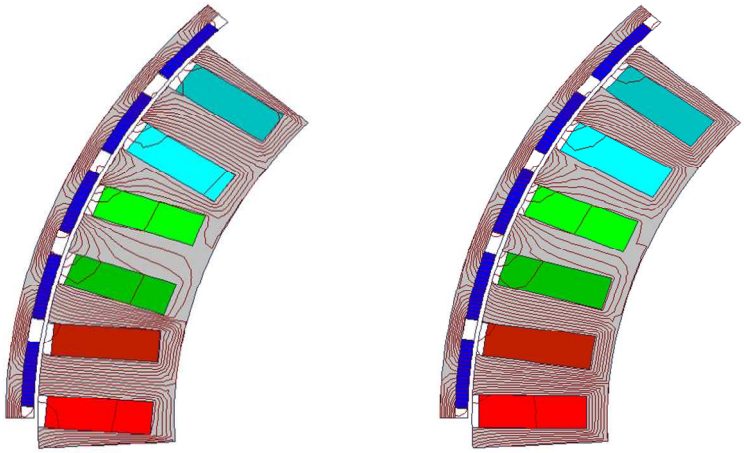

a) b)

Figure 3.11: FE model and field plot for (a) the irregular and (b) regular slotted PM machines.

3.3.3 Cogging torque analysis

The parameters in $\mathbf{X_1}$ are found to have the largest effect on the cogging torque. The cogging torque is also found to be extremely sensitive to even slight parameter changes in $\mathbf{X_1}$. The focus of the second design optimisation is thus to minimise $\Delta\tau$ by varying only the design parameters in $\mathbf{X_1}$, while keeping the parameters in $\mathbf{X_2}$ fixed. With the optimisation techniques as described, it proves difficult to find the absolute minimum value for $\Delta\tau$. The minimisation of the cogging torque thus requires, a more intensive and thorough analysis to avoid local minimum function values.

A. Single parameter variation

From $\mathbf{X_1}$ the three parameters having the largest effect on the cogging torque were identified as σ_m, σ_t and σ_g. To gain more knowledge on the effects of these parameters on $\Delta\tau$ and τ_{ave}, a single parameter variation for each of these parameters was done. This was done by keeping all other machine design parameters fixed, while varying separately each of the above mentioned parameters. The effect of these variations on $\Delta\tau$ and τ_{ave} of the machine in Fig. 3.11(a) are shown in Fig. 3.12.

The much more sensitive nature of $\Delta\tau$ compared to τ_{ave} can clearly be seen in Fig. 3.12. It is clear that the best cogging torque performance occurs at specific values of the above varied parameters σ_m, σ_t and σ_g. With τ_{ave} only changing slightly, these optimum values can thus be chosen as the optimum machine parameters without drastically affecting the rated average machine performance.

B. Multi-parameter variations

Due to the irregular and sensitive behaviour of $\Delta\tau$ toward parameter changes, a more thorough analysis is done by means of a multi-parameter variation. Fig. 3.13 shows the variations in cogging torque if the slot width and slot pitch are varied with σ_m a parameter. In each case a linear variation as in the previous section is done for σ_g and σ_t, but for different values of σ_m. It is thus evident that certain parameter values lead to a lower cogging torque irrelevant of other parameter changes. In Fig. 3.13(a) σ_t is fixed at 1.01 pu and in Fig. 3.13(b) σ_g is fixed at 0.44 pu. These values are obtained from Fig. 3.12(b) and (c).

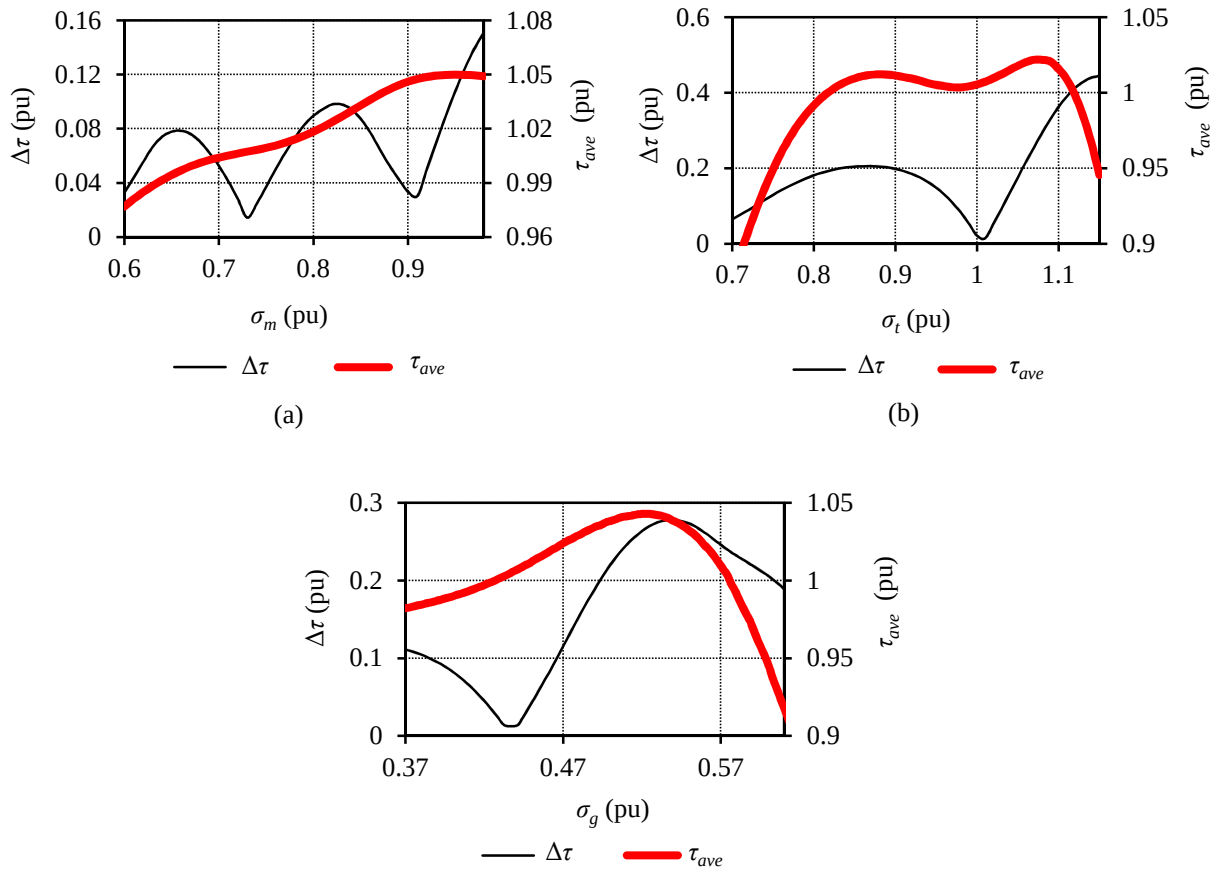

Figure 3.12: Per unit cogging torque and average torque of the irregular parallel slotted machine (Fig. 3.11a) versus (a) magnet pitch, (b) slot pitch ratio and (c) slot opening width ratio.

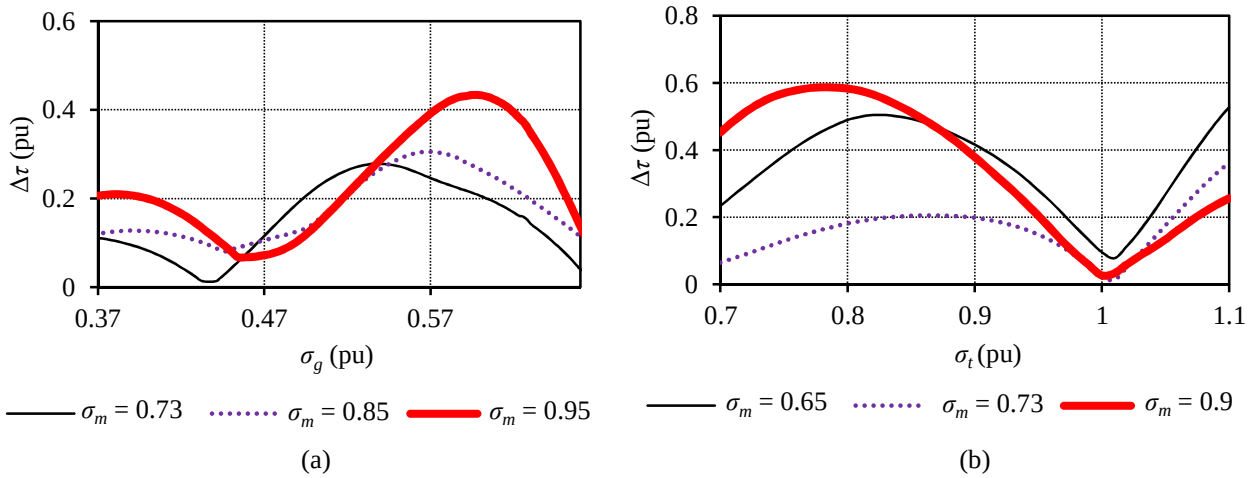

(a) (b)

Figure 3.13: Per unit cogging torque versus (a) slot width and (b) slot pitch with magnet pitch a parameter of the irregular parallel slotted machine (Fig. 3.11a).

Elaborating on Fig. 3.13 are the results shown in Figs. 3.14-3.17 with a more comprehensive multi-parameter variation. The visual representation obtained by doing these multi-parameter variations gives valuable information on the torque behaviour of the machine. With the proposed machine type having the irregular slotting as shown in Fig. 3.11(a), multi-parameter variations are done for the regular tapered slotted machine as in Fig. 3.11(b) as well. Fig. 3.14 shows the cogging and average torque behaviour of the irregular parallel slotted machine with a variation in slot width and magnet pitch. In Fig. 3.15 the same variation is done for the regular slotted machine. Figs. 3.16 and 3.17 show the cogging and average torque for a variation in magnet pitch and slot pitch for both the irregular and regular slotted machines. In each case all other machine parameters are kept fixed as for the single parameter variations.

With the more visual representation the effects caused by the irregular slotting can be clearly seen. From Figs. 3.14 - 3.17 it is clear that the regular taper slotted machine has a much smoother and overall lower cogging torque than the irregular parallel slotted machine. However with a careful selection of parameters a low cogging torque can still be obtained with this irregular slot-layout. Another important observation from Fig. 3.14 - 3.17 is that regions of high and low cogging torque exist. This can clearly be seen in Fig. 3.14(a) with a well defined “valley” for the slot width independent of changes in magnet pitch. Again as in Section A the smooth and less sensitive nature of the average torque is seen. Parameter selections can thus be made without a significant reduction in the average torque as shown in Figs. 3.14 - 3.17.

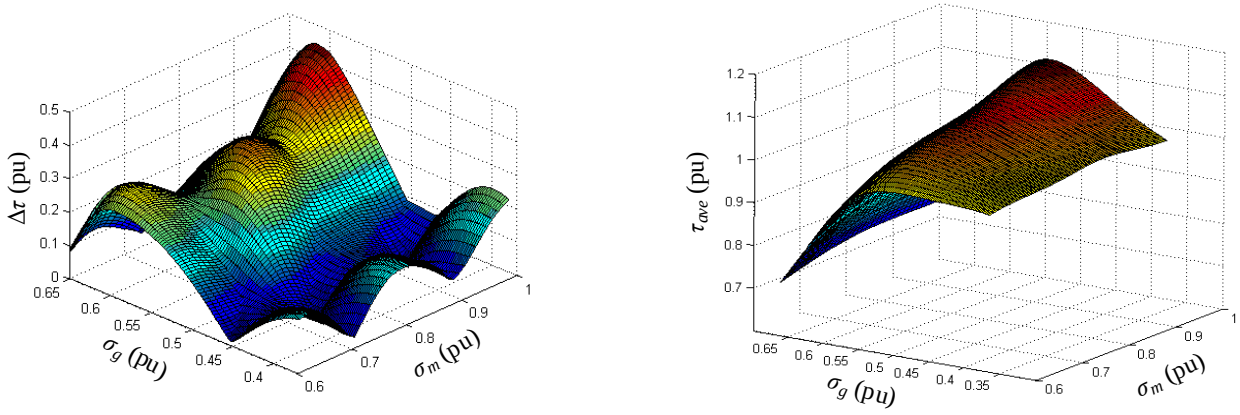

(a) (b)

Figure 3.14: (a) Cogging - and (b) average torque with a variation in per unit slot width and magnet pitch of the irregular parallel slotted machine (Fig. 3.11a).

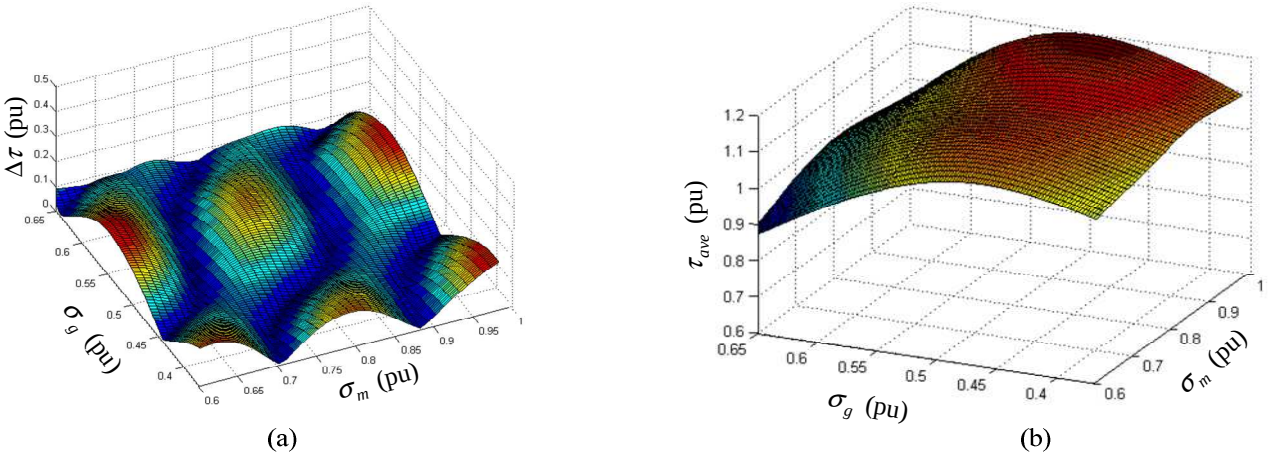

(a) (b)

Figure 3.15:(a) Cogging - and (b) average torque with a variation in per unit slot width and magnet pitch of the regular tapered slotted machine (Fig. 3.11b).

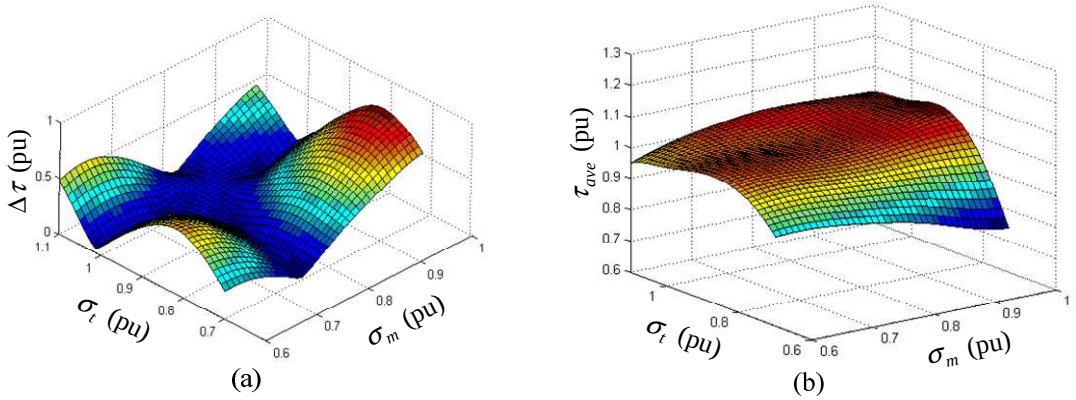

(a) (b)

Figure 3.16:(a) Cogging - and (b) average torque with a variation in per unit slot pitch and magnet pitch of the irregular parallel slotted machine (Fig. 3.11a).

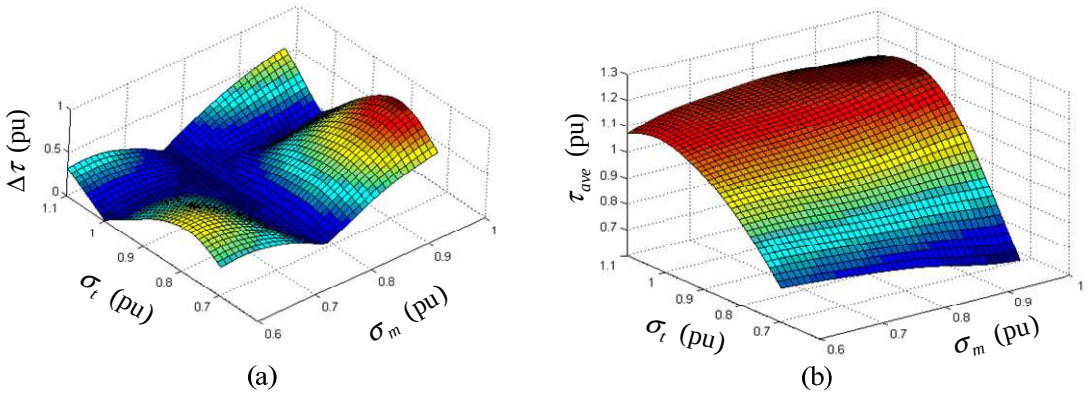

(a) (b)

Figure 3.17:(a) Cogging - and (b) average torque with a variation in per unit slot pitch and magnet pitch of the regular tapered slotted machine (Fig. 3.11b).

To obtain the plots shown in Figs. 3.14 - 3.17, several time-consuming FE simulations are needed. However, from Fig. 3.13 a prediction can be made as to where the low cogging torque regions are situated. As these are the only regions of interest, full parameter variations as done in Figs. 3.14 - 3.17 only need to be done for these regions. It should also be noted that the regions identified in Fig. 3.13 are very much independent of changes in the magnet pitch. This is important as the manufacturing accuracy of some parameters is more difficult to control. For instance the manufacturing tolerances associated with the magnets are much higher than those for the manufacturing of the laminations.

C Effect of stator and rotor yokes

Despite the dominant cogging effects caused by σ_m, σ_t and σ_g the yoke heights of the rotor (h_r) and stator (h_s) are also found to have effects on the cogging torque performance of the machine. This is seen in Figs. 3.18and3.19 with a variation in h_r and h_s with all other machine parameters fixed. Fig. 3.18 shows the variation in cogging torque and average torque for a variation in h_r for the irregular and regular slotted machines. In Fig. 3.19 h_s is varied for both machine types. Again the much less sensitive nature of the average torque is seen. Overall as for the other machine parameter variations in the previous sections, the much lower and less sensitive behaviour of $\Delta\tau$ of the regular slotted machine can be seen again.

Fig. 3.20 shows the cogging torque and average torque with a variation in the rotor yoke height with the stator yoke height a parameter. Again in Fig. 3.20(a) a well defined region where the minimum cogging torque can be found regarding a variation in the rotor yoke height is clearly observed and again only slight changes are imposed on the average torque. It is also seen that the cogging torque is overall less at larger yoke heights, but a low cogging torque region is also obtained in a smaller yoke height region, with a higher cogging torque region in between. The reason for this variation might be due to the change in reluctance as the yoke height is varied, which has the result of the air gap flux paths being changed, which in turn influences the cogging torque.

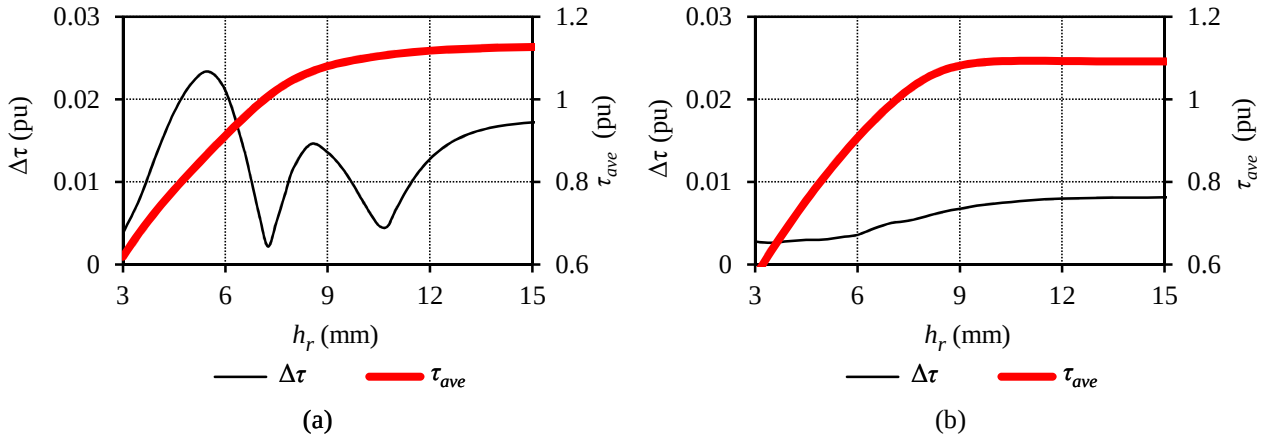

Figure 3.18: Per unit cogging torque and average torque versus rotor yoke height of (a) the irregular parallel slotted machine (Fig. 3.11a) and (b) the regular tapered slotted machine (Fig. 3.11b).

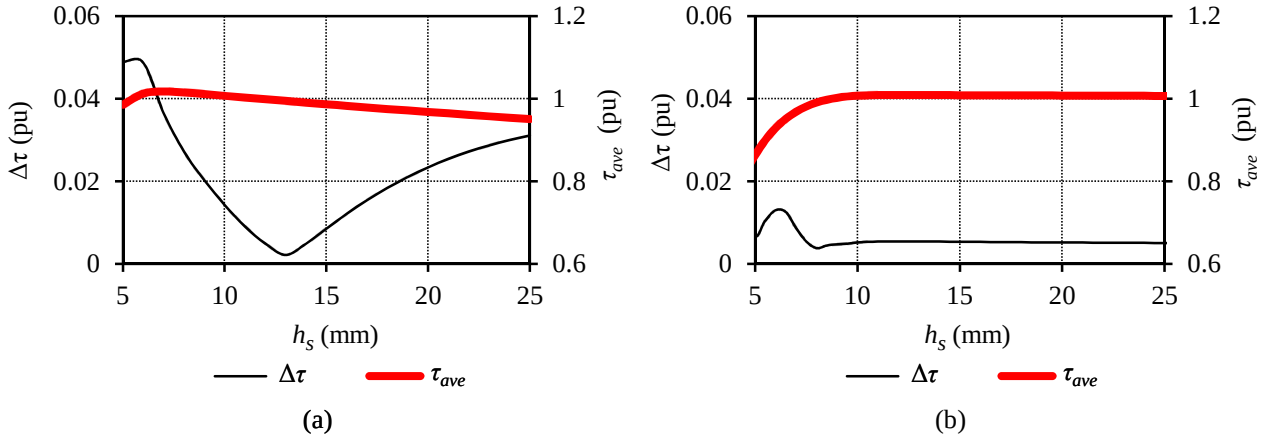

Figure 3.19: Per unit cogging torque and average torque versus stator yoke height of (a) the irregular parallel slotted machine (Fig. 3.11a) and (b) the regular tapered slotted machine (Fig. 3.11b).

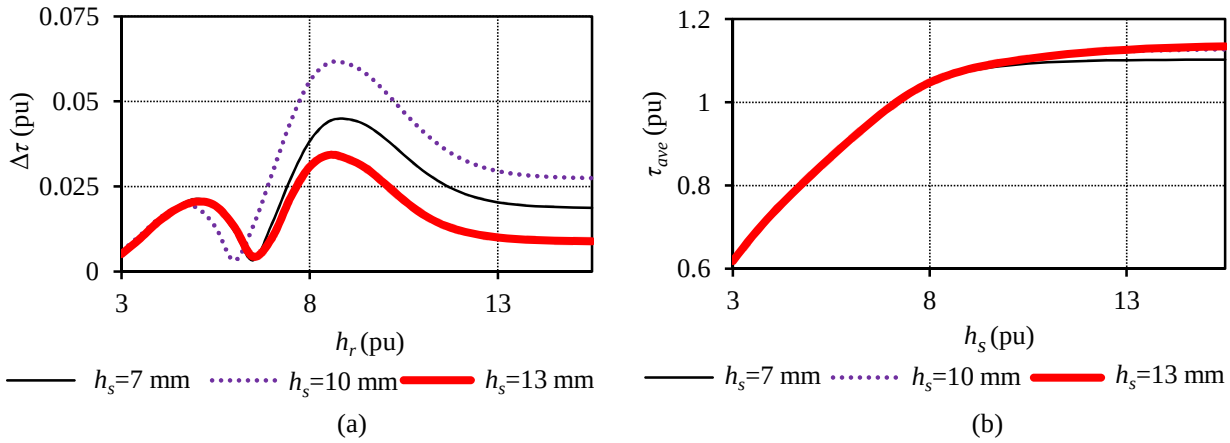

Figure 3.20: Per unit (a) cogging torque and (b) average torque versus rotor yoke height with stator yoke height a parameter of the irregular parallel slotted machine (Fig. 3.11a).

The much more sensitive nature of $\Delta\tau$ for the irregular parallel slotted machine can definitely be attributed to the slot layout. To more clearly show the effect of the paralleled slots on the cogging torque, the inside diameter is also varied. This is done for the irregular slotted machine in Fig. 3.21(a) and the regular slotted machine in Fig. 3.21(b). While the variation of D_i has a large effect on the irregular slotted machine almost no change can be observed in $\Delta\tau$ for the regular slotted machine. It is clearly seen in Fig. 3.21(a) that with an increase in D_i the cogging torque becomes significantly less for the irregular parallel slotted machine. Observing Fig. 3.11(a) it is seen that if D_i is increased, the distance between the two slots not parallel will increase and the effects imposed by the irregular slotting on the machine will be less.

Another interesting find is the effect of the lamination material. This is shown in Fig. 3.29(b) where the cogging torque waveforms are shown for two different lamination steels. An increase in the cogging torque amplitude is observed if the lamination steel is changed.

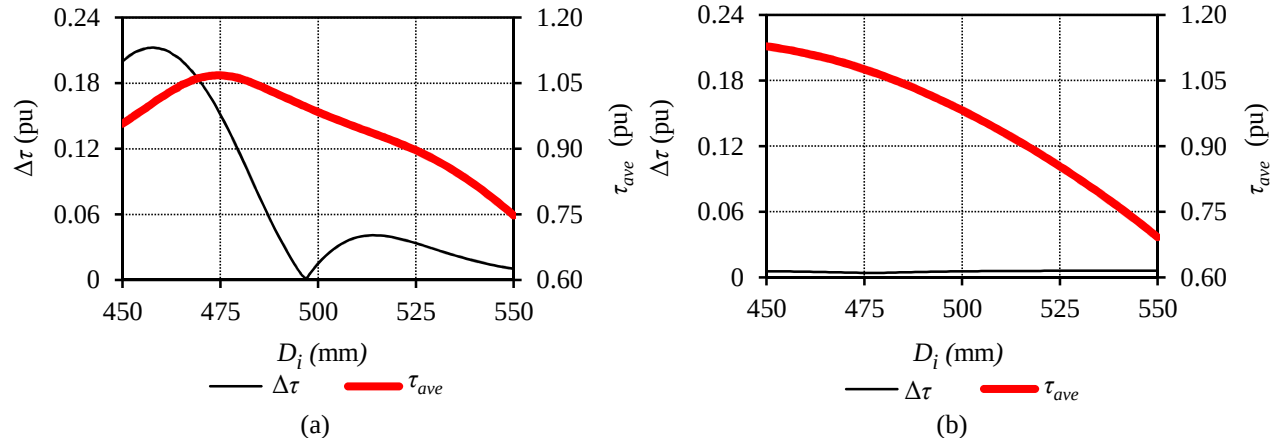

Figure 3.21: Per unit cogging torque and average torque versus the stator inside diameter of (a) the irregular parallel slotted machine (Fig. 3.11a) and (b) the regular taper slotted machine (Fig. 3.11b).

D Selection of optimum parameters

Taking all the above-mentioned design iterations into account the optimum parameters are obtained for the machine having the best cogging torque performance but with still a decent overall performance. Comparing the performance of the design in (3.21) with the optimised design in (3.22), there is a drop in average torque of 13 % but a cogging torque reduction from 26 % to 0.2 %. The active mass of the design in (3.22) is also less than that of the design in (3.21).

$$\mathbf{X_1} = \begin{bmatrix} 0.73 \\ 1.01 \\ 0.44 \\ 7.25 \\ 13.0 \end{bmatrix}; \quad \mathbf{X}_2 = \begin{bmatrix} 653.5 \\ 494.0 \\ 100.0 \\ 6.000 \end{bmatrix}; \quad \mathbf{Y} = \begin{bmatrix} 1.000 \\ 0.002 \end{bmatrix} \tag{3.22}$$

3.4FE performance evaluation of the prototype SG

The prototype SG evaluated in this section differs slightly from the optimum machine selection as given in (3.22). The prototype SG of which the dimensions and rated performance is given in Table 4, is evaluated, as this prototype is also practically implemented and evaluated in Chapter 6. The performance evaluation is done at the rated operating point of n_s = 150 r.min^{-1} and T_{rated} = 1000 Nm. To acquire confirmation on whether the results obtained by the non-commercial FE package (FE-1) are correct, a comparison is done with the performance results obtained from a commercial finite element package, Magnet v7 (FE-2).

Table 4: Parameters of the prototype SG

PARAMETER	VALUE	UNIT	PARAMETER	VALUE	UNIT
Stator inner diameter, D_i	494	mm	NdFeB magnet material type	N48H	
Stator outer diameter	623	mm	Number of stator slots, S	48	
Stator yoke height, h_s	10	mm	Number of poles, p	40	
Slot width, σ_g	0.44	pu	Number of turns per coil, N_s	424	
Slot pitch, σ_t	1.01	pu	Rated phase voltage, V_1	400/√3	V
Axial length of stack, l_1	100	mm	Rated current, I_1	23	A
Rotor inner diameter	627	mm	Rated output power, P_{gs}	15	kW
Rotor outer diameter, D_o	653.5	mm	Rated torque, T_{gs}	1000	Nm
Rotor yoke height, h_r	7.25	mm	Power factor, PF	0.95	
Rotor magnet height, h_m	6	mm	Efficiency, η_1	94.4	%
Magnet to pole pitch ratio, σ_m	0.73	pu	Rated speed, n_s	150	r.min^{-1}

3.4.1 Voltage quality

With the single layer non-overlap winding known to have a high harmonic content, it is important to evaluate the voltage quality of the prototype SG. Fig. 3.22shows the per phase flux linkage and voltage calculated at no-load plotted against the electrical angle (θ_e).With λ_1 known, V_1 is calculated knowing that,

$$V_1 = \frac{\lambda_1(t) - \lambda_1(t-1)}{\Delta t}. \tag{3.23}$$

It is clear from Fig. 3.22(b) that the voltage waveform has a significant harmonic content. To observe whether the harmonic content contained within the voltage waveform is acceptable for a grid connected system, the magnitude of the harmonic content of the voltage is calculated. Fig. 3.23 shows the magnitude of the first 22 harmonics. The first harmonic is omitted as this only indicates the amplitude of the fundamental voltage component. Also in Fig. 3.23 the maximum allowed amplitude of each individual harmonic component for a connection to the local utility grid is shown, as specified by [43]. To see whether the harmonic content of the single layer winding can be reduced with parameter changes, the effect of varying σ_m is also investigated, as shown in Fig. 3.23.

In [43] a limit of 8% is specified for the total harmonic distortion (THD) caused by the first 40 harmonics. The THD can be calculated from (3.24) as

$$\mathrm{THD} = \frac{\sqrt{\sum_{k=2}^{n} V_k^{\,2}}}{V_{1\,peak}}. \tag{3.24}$$

The THD of the used machine with σ_m = 0.73 pu amounts to 8.09%, while the THD for σ_m = 0.90 pu is 5.08 %. It is thus possible to design a single layer winding machine with an acceptable voltage harmonic content in the context of [43]. Specifying σ_m at 0.90 pu would be the better option with regard to the voltage harmonic content of the machine, but this will result in a machine having a slightly higher cogging torque as shown in Fig. 3.12(a). However, specifying σ_m at 0.90 pu is still in an overly low cogging torque region as seen in Fig. 3.12(a).

In the current design case, cogging torque is identified as a more important design aspect than voltage quality and σ_m is kept at 0.73 pu. Also, the first developed SG is connected to the grid via a solid state converter (SSC), where the voltage harmonic content as shown in Fig. 3.23 is less of an issue. For the directly grid connected SG a design can be finalised after a first practical analysis as done in Chapter 6. Although it is possible to obtain a SG design based on the non-overlap single layer winding to comply with the grid standards given in [43], there are more stringent grid codes, to which this SG design might not comply.

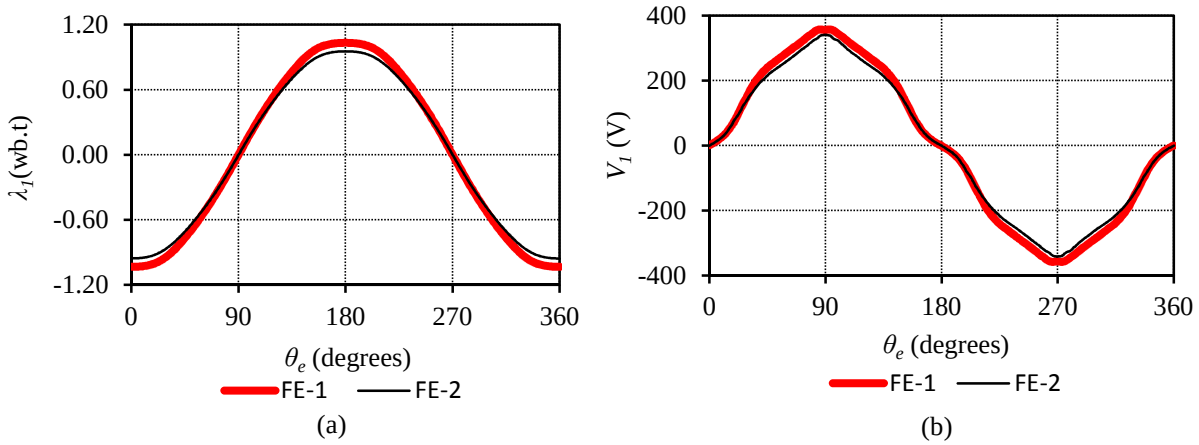

Figure 3.22: Calculated per phase (a) flux linkage and (b) induced voltage at no-load versus electrical angle for two FE packages.

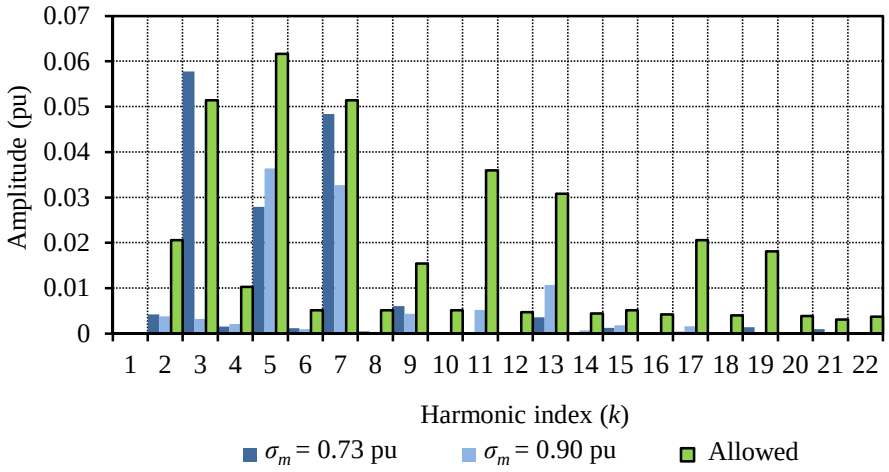

Figure 3.23: Amplitudes of the harmonics present in the voltage waveform.

3.4.2. Flux density and PM-rotor flux linkage

The next parameter observed is the magnetic flux density in the air gap of the SG shown in Fig 3.24 as calculated by the non-commercial FE package (FE-1) in (a) and the commercial FE package (FE-2) in (b). In both cases the air gap flux density data are shown together with the fundamental and plotted versus the mechanical position (θ_M). Overall the peak values of both the fundamental waves correspond very well for both FE packages.

To acquire an indication on the behaviour of the PM flux in the rotor, a one turn coil enclosing a permanent magnet is defined in the FE model as shown in Fig. 3.25. It is approximated that if the flux linkage (λ_3) of this magnet coil is calculated it will be a close indication of the PM flux behaviour in the magnets and rotor yoke. In Fig. 3.26 a clear ripple is observed in the flux linkage of the magnet coil versus rotor position. This ripple is caused by the stator slotting.

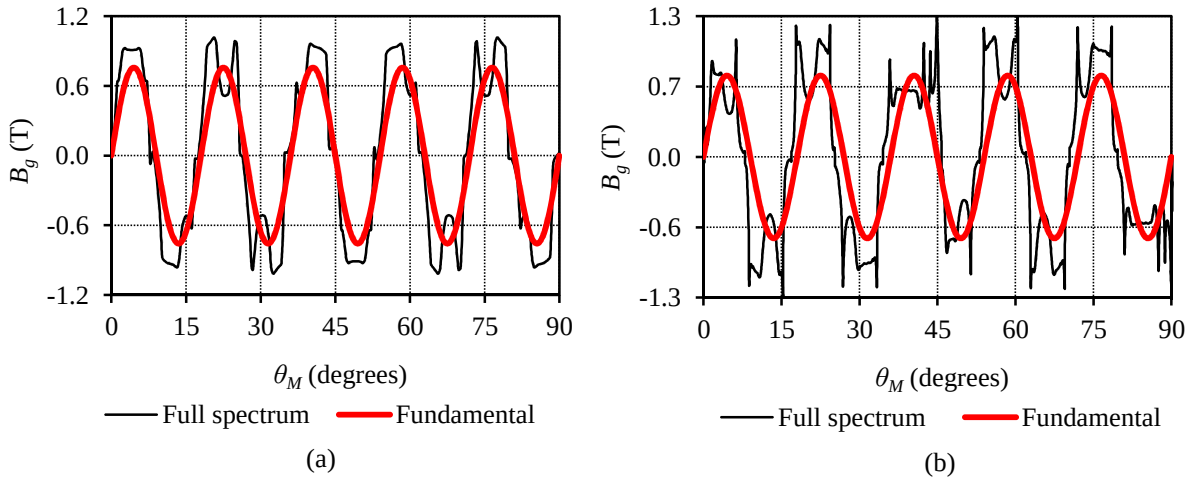

Figure 3.24: Per phase air gap flux density together with its fundamental versus mechanical air gap position calculated by (a) FE-1 and (b) FE-2.

Figure 3.25: Permanent magnet with a coil defined in the FE model.

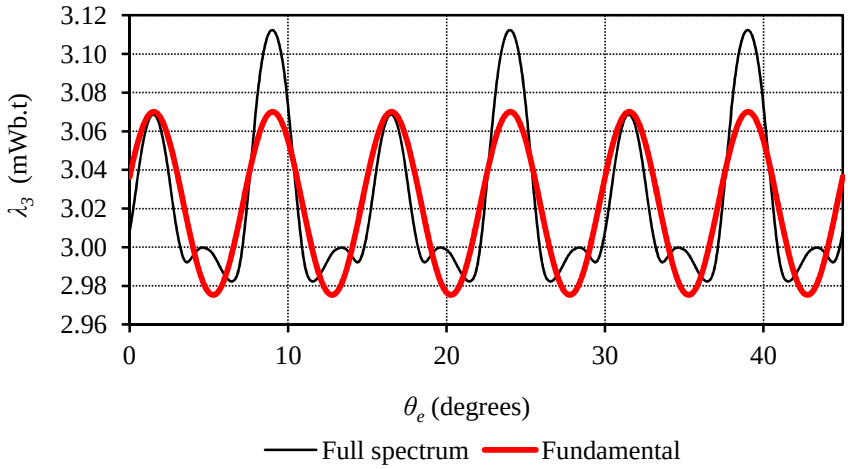

Figure 3.26: Magnet coil flux linkage and its fundamental versus rotor position at no-load.

To get an indication of the amplitudes of the harmonic components included in the magnet coil flux linkage waveform, a frequency analysis is done. The different flux linkage harmonics are shown in Fig. 3.27(a) at no-load. Also to get an indication of the behaviour of these harmonic components under rated load, the load frequency components are shown Fig. 3.27(b). It is clear that with the machine under load a large increase in the amplitude of the flux linkage harmonic components are observed.

From the work done in [38], a relationship between the magnet coil flux linkage ripple and the rotor eddy current losses (P_{er}), as calculated by FE loss analysis at no-load, is observed as shown in Fig. 3.28. In Fig. 3.28 P_{er} is compared against the amplitude of the first harmonic of Fig 3.27(a). It should be noted that P_{er} is the sum of the rotor-yoke eddy current losses as well as the rotor PM losses. An observation is thus made that with a decrease in the rotor yoke height, the eddy current losses in the yoke and permanent magnets decrease. The rotor yoke height of 7.25 mm as given in Table 4 is thus also the optimum choice regarding the rotor eddy current loss reduction.

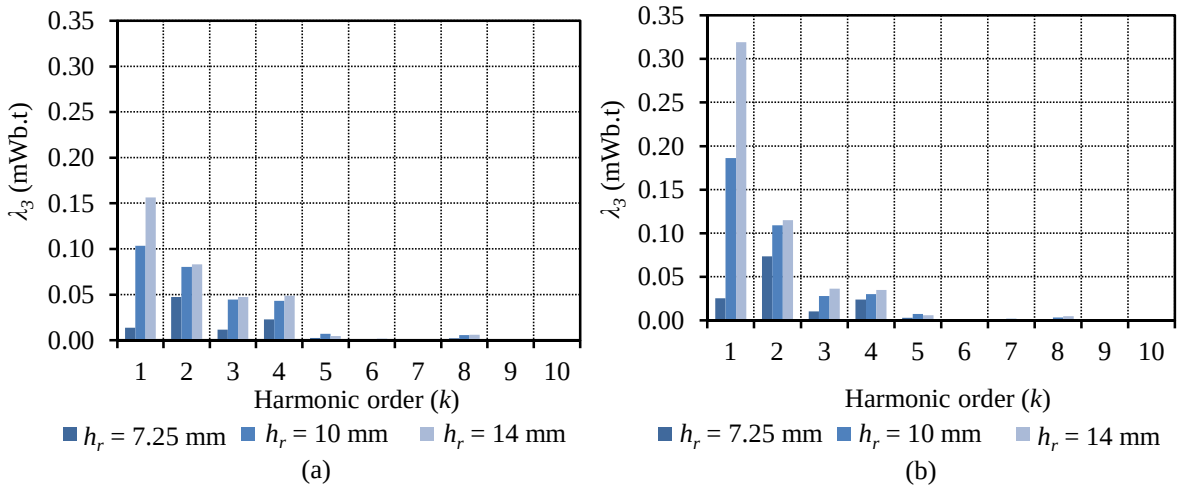

Figure 3.27: Harmonic components of the magnet coil flux linkage with rotor yoke height a parameter at (a) no-load and (b) rated load.

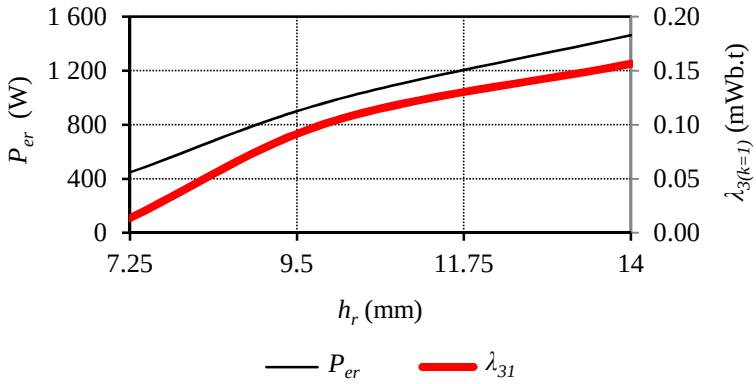

Figure 3.28: Rotor eddy losses and first harmonic magnet coil flux linkage versus rotor yoke height.

3.4.3 Torque quality

Fig. 3.29(a) shows the no-load torque (T_{cog}) of the prototype SG rotated through 360 electrical degrees. The results shown are calculated for both FE packages and are in good agreement. In Fig 3.29(b) T_{cog} is calculated for two different lamination steel types used in the SG. From this it can be seen that the lamination steel also contributes to the torque quality.

With the no-load torque characteristics known the torque quality of the machine at rated load is evaluated as well. Fig 3.30 shows the SG's torque at rated load versus electrical rotor position. Again the torque is calculated by both FE packages and also in this case FE-1 and FE-2 show good agreement. The load torque ripple is about 4 to 5 times higher than the no-load torque ripple.

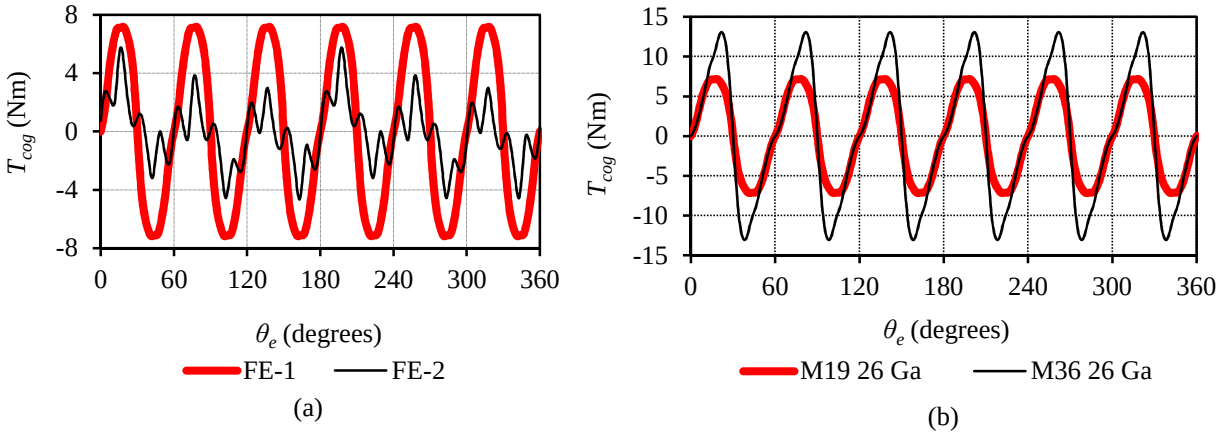

Figure 3.29: Cogging torque waveforms of the SG plotted in (a) for both FE packages and in (b) with the use of two different lamination steels using FE-1 versus electrical rotor position.

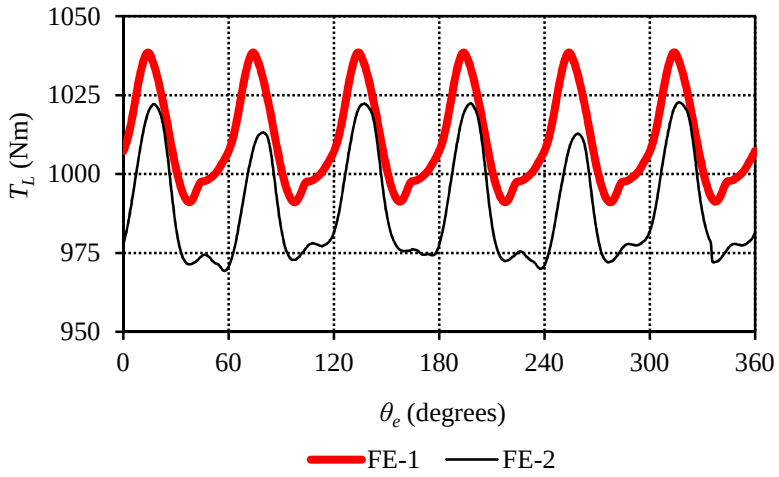

Figure 3.30: Torque waveform of the SG at rated load calculated by both FE packages versus electrical rotor position.

3.4.4 *dq*-Inductances

Shown in Fig. 3.31 is the variation in the *d* and *q*-axis inductances versus the I_{ds} and I_{qs} load currents, which differs significantly even for this surface mounted PM machine. The effects of cross magnetization and saturation can be clearly seen in Fig. 3.31. From Fig. 3.31 it is clear that the differences in the *dq* inductances need to be taken into account in the simulation models as discussed in sections 3.1.2 and 3.1.3.

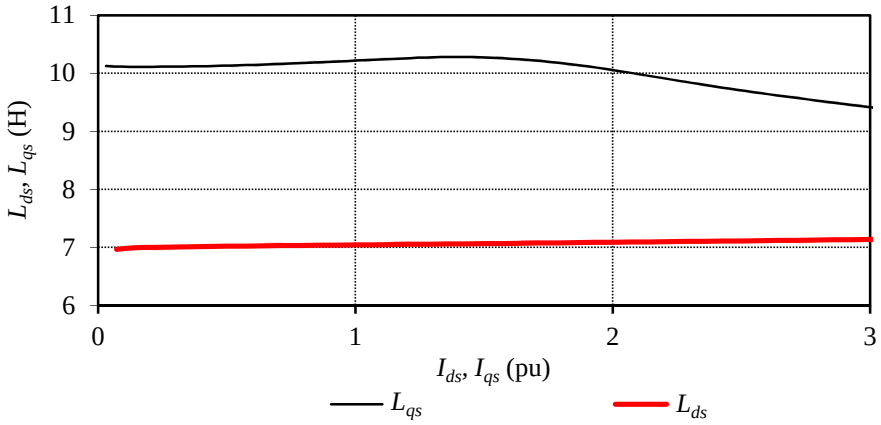

Figure 3.31: Variation of the *d*- and *q*-axis inductances against the *d* and *q*-axis currents at different load values.

3.4.5 Summary of FE-1 and FE-2 results

Table 5 summarises the FE results at the rated operating point as discussed. Overall the calculated results of the two FE packages agree fairly well for the different output parameters. A better indication on the accuracy of the FE simulation methods used can be obtained from practical measurements which are dealt with in Chapter 6.

Table 5: Machine output parameters of the SG calculated by two FE packages.

PARAMETER	UNIT	FE-1	FE-2
λ_1 (peak)	Wb.t	1.03	0.95
V_1 (peak)	V	358	342
$B_{g(k=1)}$ (peak)	T	0.746	0.741
τ_{ave}	Nm	1011	989
$\Delta\tau$	%	1.44	1.02
$\Delta\tau_L$	%	4.65	5.23

3.5SG design conclusions

Overall the goal of designing a low cost, low cogging torque, decent performing PMSG, is reached as described in this chapter, amongst others by selecting a non-overlap, single layer, pre-formed winding configuration. This generator can be operated in conjunction with a SSC as a variable speed device, or as a fixed speed generator in an S-PMIG setup.

The addition of irregular parallel stator slotting as opposed to the regular tapered slotting, posed some challenges in the minimisation of the cogging torque. The cogging torque is found to be extremely sensitive to slight parameter changes. However, it is shown that with a careful FE analysis a low cogging torque can be obtained for this machine. This minimum cogging torque is also obtained without significantly reducing the average torque performance of the SG. A method is also introduced to minimise the cogging torque of this machine with a much reduced amount of FE simulations. Interesting and important is the influence of yoke height variations and the lamination material on the cogging torque, where, with the selection of the correct parameter values, the cogging torque can be reduced to a further extent.

It is still a question if the high harmonic content of the single-layer winding is acceptable. In this regard it is shown that with certain parameter variations the harmonics in the voltage waveform can be decreased. It is also shown that the impact of the losses in the PMs and rotor yoke can be reduced by choosing the correct rotor yoke height. It is also shown that even for a surface mount PM machine design as used in this study, there is a significant difference between the *d* and *q* axis inductances.

Chapter 4 – Split-PMIG: Design of theIG

The design of the turbine connected IG unit of the S-PMIG system is very similar to the SG design covered in the previous chapter. The only difference is that the windings of this machine are short circuited and that solid bars are used. This chapter focuses on the optimal design of the short-circuited IG as shown in Fig. 4.1(b).

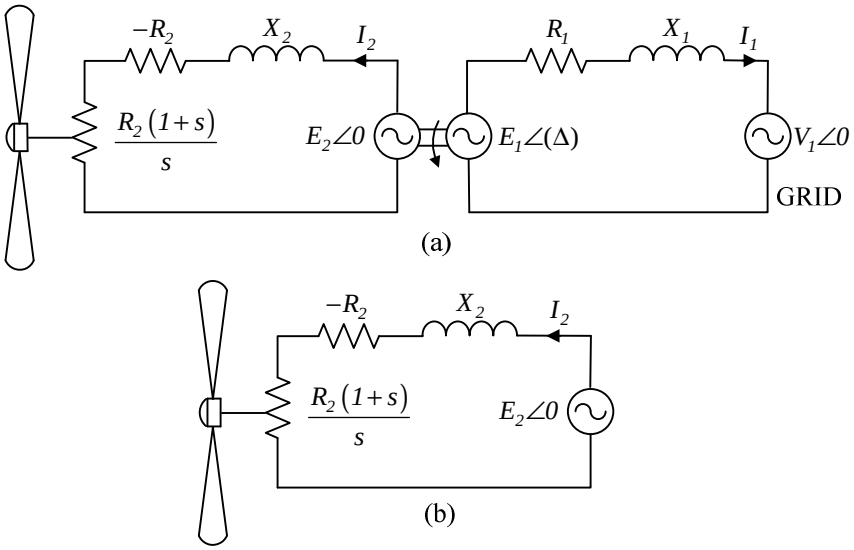

Figure 4.1: (a) S-PMIG equivalent circuit with (b) the IG unit equivalent circuit as used in this chapter.

4.1 Machine selection

As for the SG unit, by making use of the split-PMIG concept, a large degree of freedom exists for the selection of the IG machine configuration. An important design aspect to consider is whether to use normal overlap windings as used in conventional induction machines or to make use of non-overlap windings as used for the SG design. Overlap windings with a lower synchronous reactance than non-overlap windings might result in a better performance. However, with overlap windings cogging torque becomes a significant problem, as opposed to the much lower overall cogging torque of non-overlap windings. To limit the cogging torque, techniques like skewing might be needed, which can increase the mechanical complexity of the machine. Also overlap windings have a much higher number of coils than non-overlap windings, but with the use of solid conductive bars, more coils might pose less of a drawback. This, however, depends on the assembly methods.

With the emphasis being on keeping the design as simple as possible, as well as the importance of a low cogging torque, non-overlap windings are used. Furthermore due to the simplification of the winding process by using solid bars, double layer windings, which normally result in a better performance than single layer windings, are also proposed as a solution. With the speed and torque input requirements the same for the IG as for the SG, as well as a similar winding topology, many of the design procedures used in Chapter 3 can be used for the design of the IG. Furthermore if the same number of poles and slots are used as well, the design process can be significantly simplified.

4.2 FE modelling

By making slight modifications to the FE modelling procedures explained in sections 3.1.2 and 3.1.3, these methods can be applied to the design of the IG. To model the short-circuited windings of this machine the steady state *dq* equivalent circuits in Fig. 3.3,with the IG *dq* currents given by I_{dr} and I_{qr}, can be modified with $V_{ds} = V_{qs} = 0$ as shown in Fig. 4.2. The current angle is given by α_r and E_{qr} is the *q*-axis induced voltage.

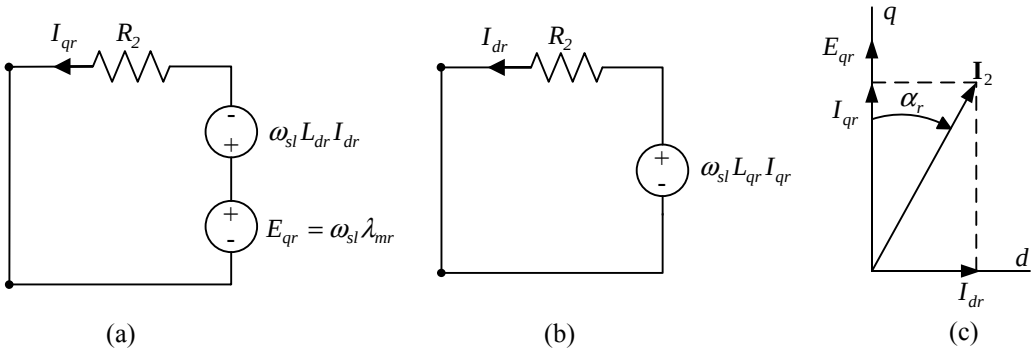

Figure 4.2: Steady-state *dq* equivalent circuits for (a) *q*-axis; (b) *d*-axis and (c) vector diagram of the IG.

From the circuits in Fig. 4.2 the steady state *dq* equations can be derived as given in (4.1) with

$$\begin{aligned} 0 &= -R_2 I_{qr} - \omega_{sl} L_{dr} I_{dr} + \omega_{sl} \lambda_{mr}; \\ 0 &= -R_2 I_{dr} + \omega_{sl} L_{qr} I_{qr}. \end{aligned} \tag{4.1}$$

The electrical speed of this machine is the relative speed of the turbine connected cage-rotor to the speed of the free rotating PM-rotor, which is given as the slip speed namely ω_{sl} = (p/2)ω_t – ω_s with positive slip indicating power being generated to the grid. The cage-rotor mechanical speed is equal to the turbine speed ω_t. The *dq* inductances are calculated in the same manner as in section 3.1.2, by using the FE calculated *q*-and *d*-axis flux linkages (λ_{qr} and λ_{dr}) and the FE calculated PM flux linkage of the IG (λ_{mr}).

The machine torque is calculated from (3.11) by using IG parameters. With the IG only operating at a relative slip speed of ω_{sl}, the PM-rotor eddy current and the induction cage-rotor core losses, as well as the wind and friction losses of the IG are practically zero. The only remaining losses are, thus, the rotor winding losses given by $P_{cur} = T_{gr}\omega_{slm}$. The subscript *m* indicates the use of mechanical speed. The efficiency of the IG is thus given by (4.2) as,

$$\eta_2 = \frac{P_{gr}}{P_t} = 1 - s\,. \tag{4.2}$$

P_{gr} is the output power of the IG transferred to the PM-rotor. P_{gr} and the turbine mechanical input power (P_t), is given by

$$P_{gr} = T_{gr}\omega_{sm}; \quad P_t = T_{gr}\omega_t\,. \tag{4.3}$$

Again, as in sections 3.1.2 and 3.1.3, the FE calculated parameters needed to solve the steady-state *dq* equations can be calculated by specifying a value for P_{cur}. Again R_2 is calculated by the given slot dimensions in [**X**] and thus I_{2rms} can be calculated with R_2 and P_{cur} known by (3.9). In this case again three FE iterations are needed to calculate the output parameters of the machine. For the IG modelling the unknown parameters are I_{dr}, I_{qr} and ω_{sl}. By solving (4.1) with the help of the vector diagram in Fig. 4.1(c) and (3.7), new values for I_{dr}, I_{qr}, and ω_{sl} can be calculated in the same manner as in sections 3.1.2 and 3.1.3. The current angle α_r can then be calculated from (3.8) and the machine output performance can be evaluated at this operating point.

4.3 FE design optimisation

The same approach is followed for the IG as for the SG FE design in Chapter 3 by first doing an average torque design optimisation, followed then by the cogging torque minimisation.

4.3.1 Design optimisation parameters

In a first design iteration the inside and outside diameters, d_i and d_o of the IG are sized to correspond with the SG, as the IG is mounted in front, onto the SG unit. Due to the much better fill factor obtained by using solid bar windings, the axial stack length of the IG (l_2) can be reduced. If it is approximated that the copper fill factor for the IG is about double the copper fill factor of the SG, the active copper area of the IG will be $a_{scr} = 2a_{scs}$. For a starting parameter the IG winding losses are specified as $P_{cur} = P_{cus}$. Thus with

$$P_{cur} = 3I_2^{\,2}R_2 \tag{4.4}$$

and

$$R_2 = \frac{\rho_{Cu} l_2}{a_{scr}} \approx \frac{\rho_{Cu} l_2}{2a_{scs}} \tag{4.5}$$

the stack length of the IG can be decreased by

$$l_2 = \frac{l_1}{2}. \tag{4.6}$$

This is valid if P_{cur} is to be kept the same as P_{cus} at rated load. This value of $l_2$for the IG is only a starting value and if a higher efficiency is required the stack length can be adjusted. Fig. 4.3 shows the proposed IG implementation with the use of solid rotor bars. The parameters used in the FE design optimisation are given in (4.7) as

$$\mathbf{X_1} = \begin{bmatrix} \sigma_m \\ \sigma_g \\ \sigma_w \\ h_t \\ h_r \\ h_s \end{bmatrix}; \qquad \mathbf{X_2} = \begin{bmatrix} d_o \\ d_i \\ l_2 \\ h_m \end{bmatrix}; \qquad \mathbf{U} = \begin{bmatrix} \tau_{ave} \\ \Delta\tau \end{bmatrix}, \tag{4.7}$$

with the per unit magnet pitch to pole pitch ratio (σ_m) and per unit slot width to average slot pitch ratio (σ_g) as defined in (3.17) and shown in Fig. 4.4. In this case the slot pitch to average slot pitch ratio (σ_t) is fixed at 1, due the fact that double layer windings are used as well. As shown in Fig. 4.4 the yoke height of the PM-rotor for the IG is indicated by h_r, while the IG cage-rotor yoke height is given by h_s, and h_m is the magnet height. With solid bars being used it is decided to investigate the effect of semi-closing the IG rotor slots. The dimensions for this enclosure as shown in Fig. 4.3 are the height h_t and the open slot to fully open slot ratio σ_w given as

$$\sigma_w = \frac{\theta_w}{\theta_g}. \tag{4.8}$$

In (4.8) θ_g is the slot width and θ_w is the slot opening width, both as angular dimensions. All the optimisation parameters in (4.7) are shown in Fig. 4.4.

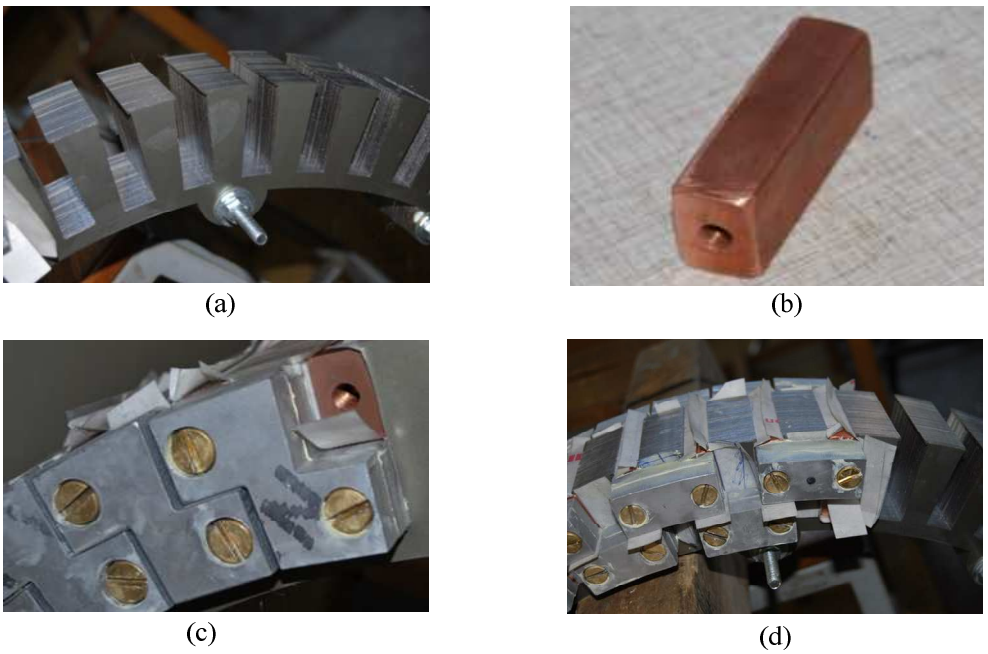

(a) (b) (c) (d)

Figure 4.3: (a) IG stack with (b) solid copper bars and (c) and (d) end connectors for a double layer IG winding.

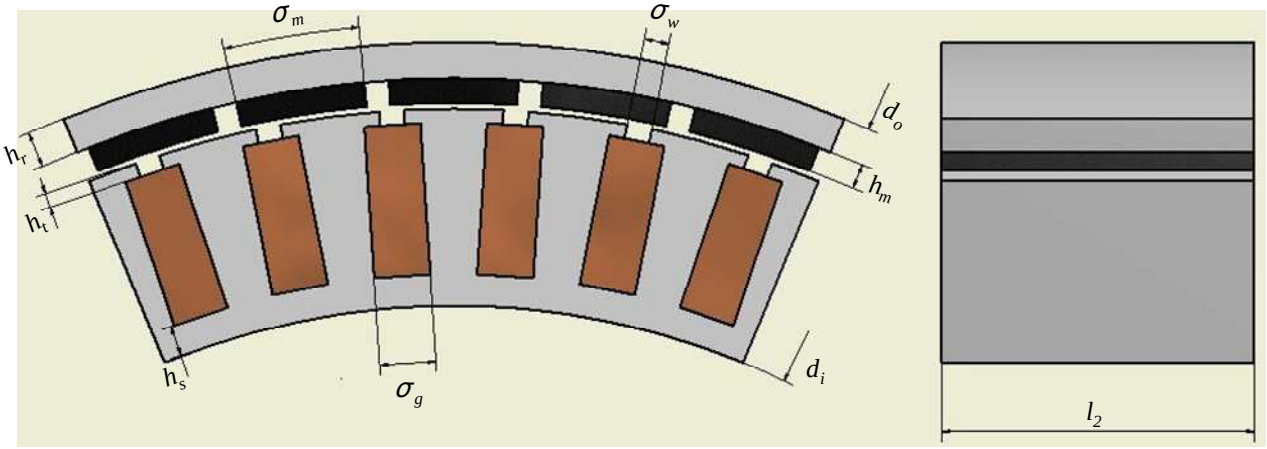

Figure 4.4: Design optimisation parameters for the IG unit.

4.3.2 Average torque design optimisation

The first FE design optimisation of the IG is done as previously, by maximising the machine torque per given copper losses, with the objective function to be maximised thus, given by

$$\mathbf{F}(\mathbf{X}) = \frac{T_{gr}}{P_{cur}}. \tag{4.9}$$

With the only loss component of the IG being the copper losses (P_{cur}), the efficiency of the IG is in effect being maximised. With the parameter values contained within **X** dependent on the required ratio of T_{gr} to P_{cur}, a required efficiency for the generator needs to be specified. To make the S-PMIG comparable with other wind generator systems currently in use an overall efficiency of η_t > 92 % is specified. With the efficiency of the SG given as about 94 % in Chapter 3, the corresponding efficiency of the IG is specified as $\eta_2 \approx 98$ %.The rated torque is specified as 1000 Nm corresponding to the turbine curves in Fig.3.5 and Table 3.The FE field plots for the two investigated winding configurations are shown in Fig. 4.5, with (a) the double layer winding and (b) the single layer winding configuration. The results of the first FE design optimisation of maximising the per unit average torque is given in (4.10).

$$\mathbf{X_1} = \begin{bmatrix} 0.98 \\ 0.45 \\ 0.82 \\ 0.50 \\ 20.5 \\ 9.00 \end{bmatrix}; \quad \mathbf{X_2} = \begin{bmatrix} 670 \\ 475 \\ 62.5 \\ 8.00 \end{bmatrix}; \quad \mathbf{U} = \begin{bmatrix} 1.051 \\ 0.054 \end{bmatrix}. \tag{4.10}$$

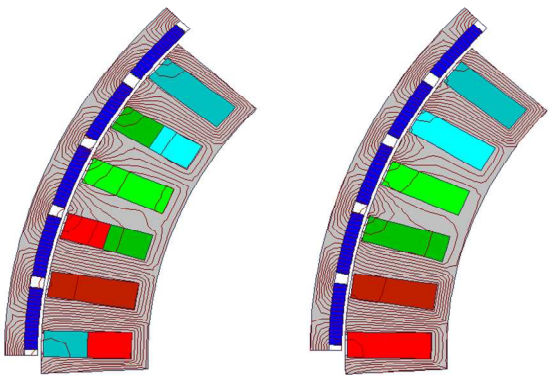

(a) (b)

Figure 4.5: FE field plot for (a) the double layer and (b) single layer IG.

4.3.3 Cogging torque minimisation

Although the cogging torque in (4.10) is not as high as found for the SG in Chapter 3 further minimisation techniques as in Chapter 3 can be used. With cogging torque an important parameter in wind generator design and to prevent any destabilising effects transferred to the common free rotating PM-rotor, an absolute minimum for this output parameter is essential.

In this case the three parameters having the largest effect on the cogging torque are identified as σ_g, σ_m and σ_w. With all other design parameters fixed these three parameters are each varied separately in the design as in Chapter 3. The effects of these variations on $\Delta\tau$ and τ_{ave} are shown in Fig. 4.6. Again the much more sensitive behaviour of $\Delta\tau$ to parameter changes as opposed to τ_{ave} is clearly seen. An attractive feature of this specific machine design is that the machine parameters resulting in a minimum value of $\Delta\tau$ are surprisingly close to the parameter values resulting in a maximum value for τ_{ave}.

From Fig. 4.6 it is clear that σ_m and σ_w have the largest effect on $\Delta\tau$. A multi-parameter variation in these two design parameters can give a very informative indication of where the optimum parameters should be selected. With σ_g and all other design parameters fixed the cogging torque and average torque results for a variation of σ_m and σ_w are shown in Fig. 4.7.

Fig. 4.7 gives valuable information on the optimum selections available for σ_m and σ_w. An interesting region is in the vicinity of σ_m = 0.84 pu and σ_w = 0.82 pu, where the cogging torque is extremely low and it is close to the optimum region for τ_{ave}. To reduce the amount of FE solutions, this region can again be easily identified as for the SG in Chapter 3 and as shown in Fig. 4.8.

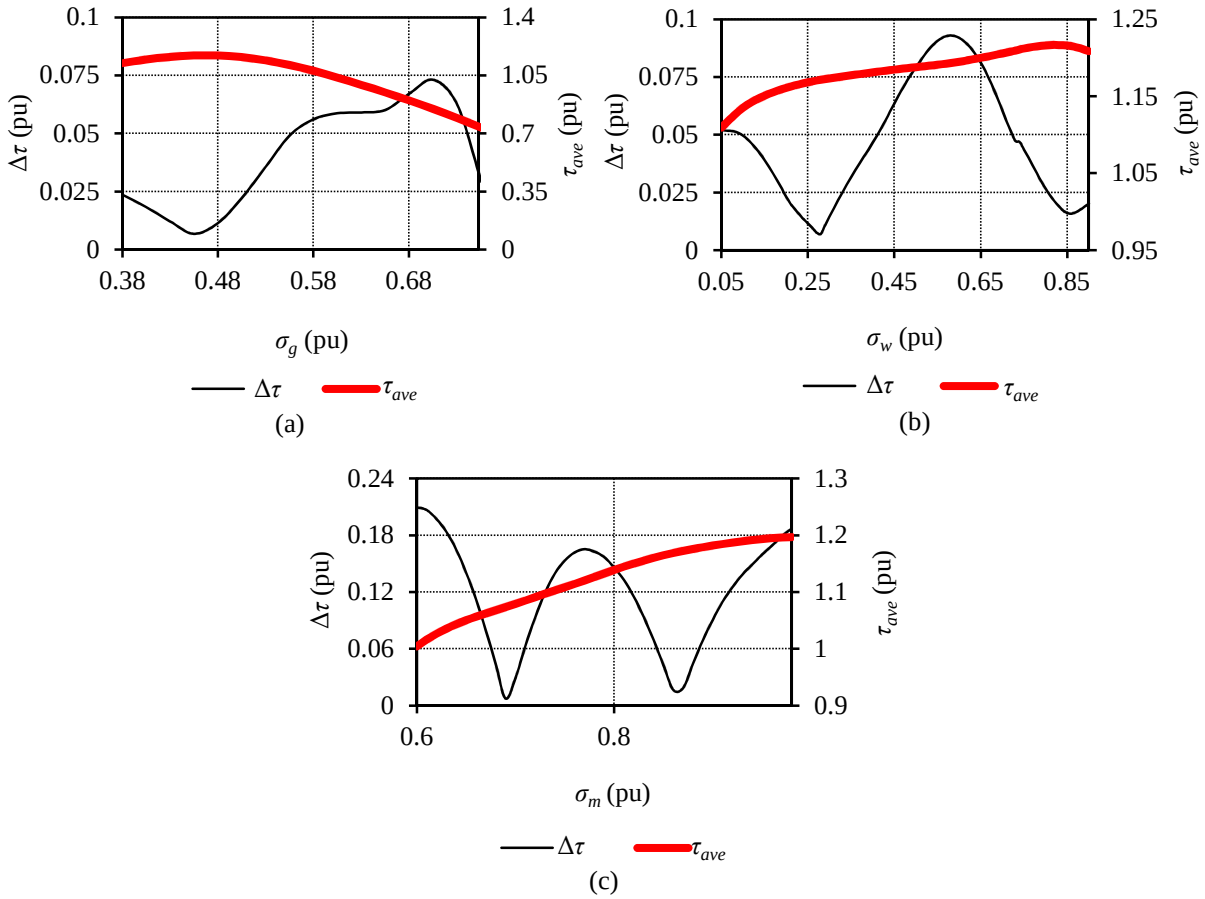

Figure 4.6: Per unit cogging torque and average torque of the IG for a variation in (a) slot width (σ_g), (b) slot opening width (σ_w) and (c) magnet pitch (σ_m).

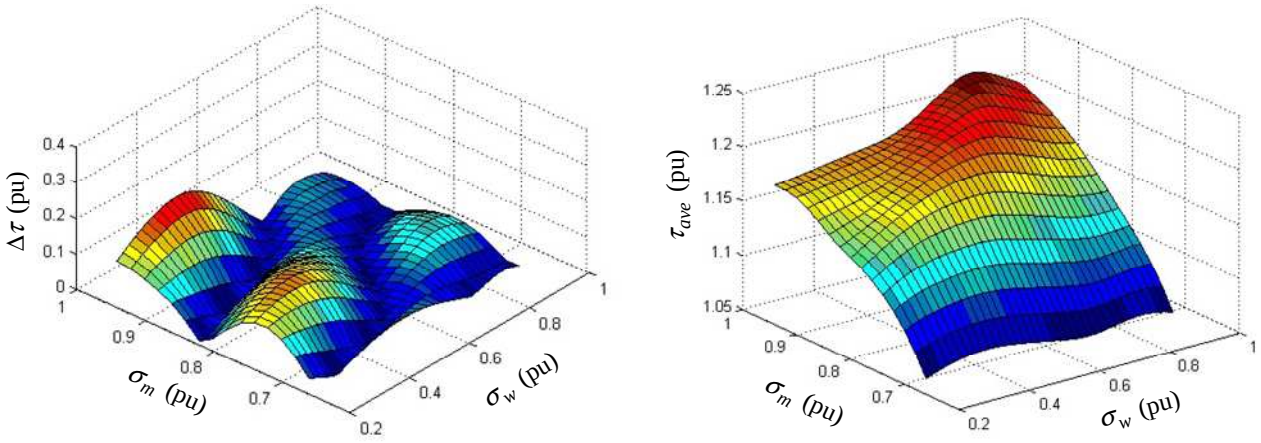

(a) (b)

Figure 4.7: (a) Cogging torque and (b) average torque of the IG for a variation in magnet pitch and slot opening width.

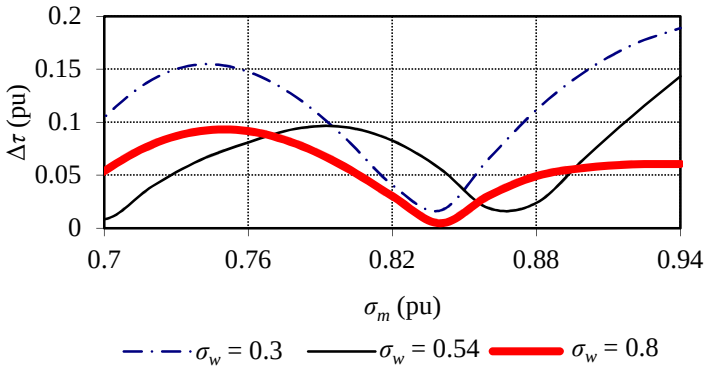

Figure 4.8: Per unit cogging torque of the IG for a variation in magnet pitch and slot opening width a parameter.

Other parameters which can be adjusted for a further reduction in $\Delta\tau$ are the height of the slot top enclosure (h_t), and the PM-rotor and IG cage-rotor yoke heights (h_r and h_s). The results for $\Delta\tau$ and τ_{ave} for the variations in h_t, h_r and h_s are shown in Fig. 4.9. Again an interesting observation is that the parameter selections for a minimum cogging torque coincide closely with the parameters resulting in the best average torque performance. Also in this instance the effects of the yoke heights are not as significant as with the design of the SG with the irregular slotting.

With some minor adjustments to the parameters contained within $\mathbf{X_1}$ the values corresponding to the optimum machine selection are given in (4.11). Comparing (4.10) and (4.11) it is seen that the cogging torque is reduced significantly, with only a slight reduction of 1.05 pu to 1.0 pu in the average torque. In this case the selection of the parameters in (4.11) also leads to a significantly lower overall mass than for the machine design given by (4.10).

$$\mathbf{X_1} = \begin{bmatrix} 0.84 \\ 0.44 \\ 0.81 \\ 1.20 \\ 11.5 \\ 10.0 \end{bmatrix}; \quad \mathbf{X_2} = \begin{bmatrix} 652 \\ 483 \\ 62.5 \\ 8.00 \end{bmatrix}; \quad \mathbf{U} = \begin{bmatrix} 1.000 \\ 0.003 \end{bmatrix}. \tag{4.11}$$

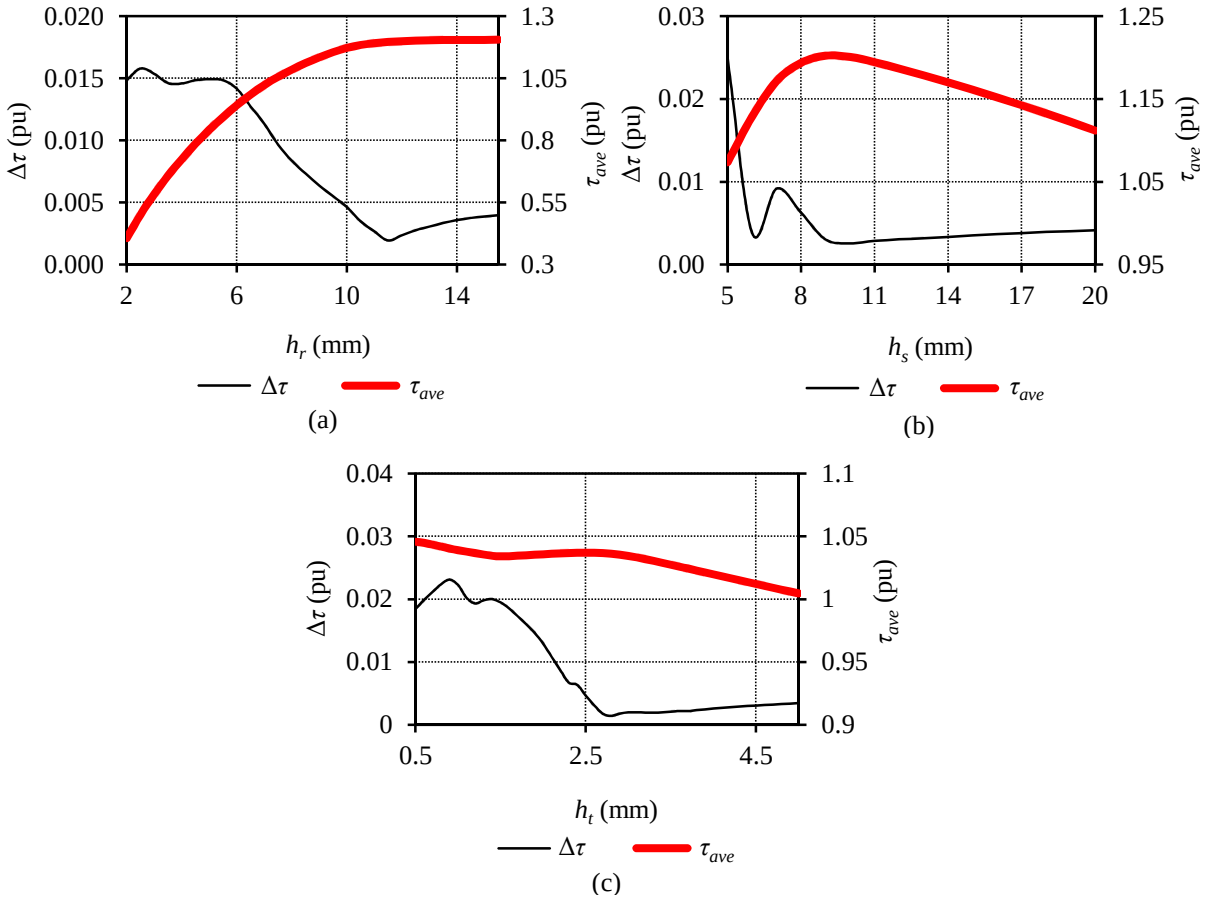

Figure 4.9: Per unit cogging and average torque versus (a) PM-rotor yoke height (h_r), (b) IG cage-rotor yoke height (h_s) and (c) the slot enclosure height (h_t).

4.4 IG performance

Table 6 gives a summary of the dimensions and the performance of the machine design proposed for implementation. The performance parameters in Table 6 are based on the double layer winding IG, but both the single layer and double layer winding configurations are considered for the machine evaluation.

Table 6: Dimensions and performance parameters of the IG.

PARAMETER	VALUE	UNIT	PARAMETER	VALUE	UNIT
Outside diameter, d_0	652	mm	NdFeB magnet type	N48H	
Inside diameter, d_i	483	mm	Number of IG cage slots, R	48	
IG cage-rotor yoke height, h_s	10	mm	Number of poles, p	40	
Slot width	17.5	mm	Rated torque, T_{gr}	1000	Nm
Slot opening to slot width ratio, σ_w	0.81	pu	Pull-out torque, T_b	2000	Nm
IG axial length, l_2	62.5	mm	Rated per phase current, I_2	6.3	kA
PM-rotor inner diameter	613	mm	Rated output power, P_{gr}	16	kW
PM-rotor yoke height, h_r	11.5	mm	Efficiency, η_2	98	%
PM height, h_m	8	mm	Synchronous speed, n_s	150	r.min^{-1}
Magnet to pole pitch ratio, σ_m	0.84	pu	Rated slip, s_r	1.7	%

4.4.1Induced voltage and torque quality

Fig. 4.10(a) shows the per phase flux linkage (λ_2) of the IG for both the single layer and the double layer winding configurations. With the number of turns for the IG coils fixed at N_r = 1, the double layer winding has a higher flux linkage and voltage due to the fact that two coils are connected in series. Fig 4.10(b) shows the voltage waveforms of the two different winding layouts. A quick observation of Fig. 4.10(b) shows that the harmonics present in the single layer winding are clearly much lower than those found for the SG in Chapter 3. However, in this case the voltage quality is irrelevant, as the IG only transfers torque to the SG unit.

Fig. 4.11 shows the FE prediction of the torque of the IG at no-load (T_{cog}) and at rated load (T_L). A no load torque ripple of 0.3 % is predicted while the rated load torque ripple is predicted as 2.60 %. The torque waveforms shown are for the double layer winding. The torque ripple of the single layer winding is predicted slightly higher at 3.73 %. The rated torque is 1000 Nm as given in Table 6.

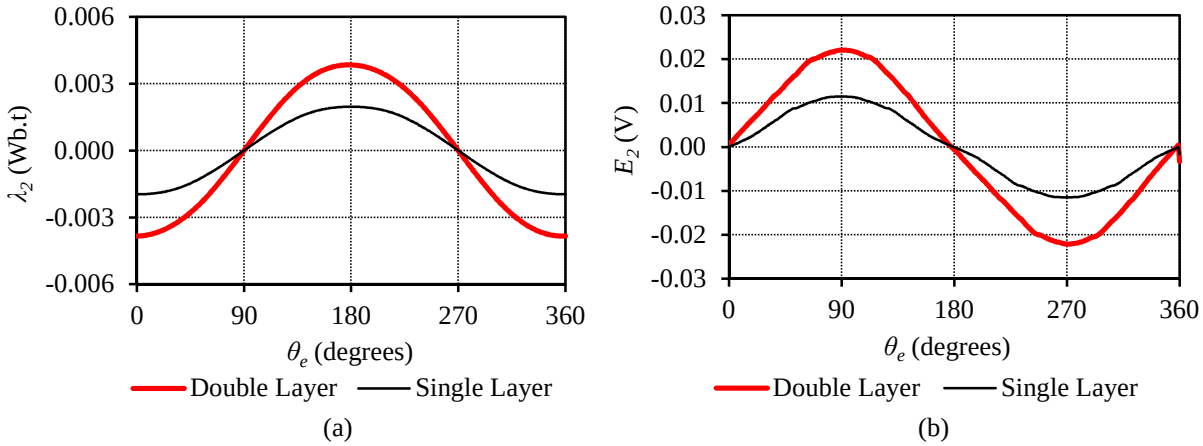

Figure 4.10: (a) Per phase flux linkage and (b) per phase induced voltage, versus electrical angle for the single and double layer windings.

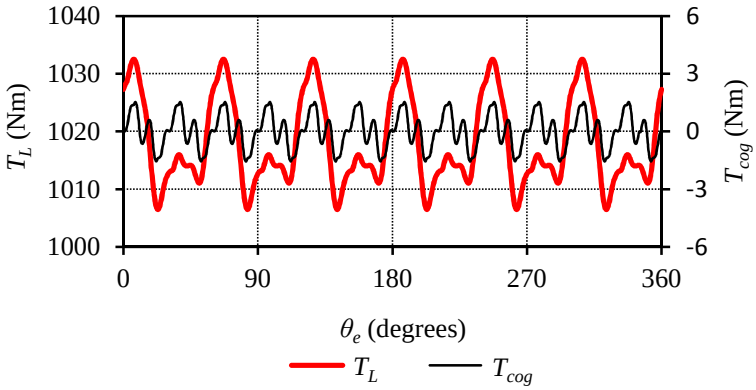

Figure 4.11: FE calculated no-load and rated load torque waveforms versus electrical rotor position.

4.4.2 Slip speed characteristics

The IG unit is evaluated under different load conditions by FE-calculating the output parameters against different slip values. The average torque of the IG is shown in Fig. 4.12(a), for the double and single layer windings. Only at higher slip values is a difference observed between the two winding configurations.

Fig. 4.12(b) shows the IG's output power versus slip, while the RMS induced voltage and the IG bar current is shown in Fig. 4.13 for both winding layouts. It should be noted that the per phase IG current (I_2) used in the equivalent circuit modelling of Fig. 4.1(b) and given in Table 6, is eight times the bar current, as one phase consists of eight bar coils. The efficiency of the IG versus the per unit load torque is shown in Fig. 4.14 where no real difference is observed between the single and double layer windings at the lower and rated load values.

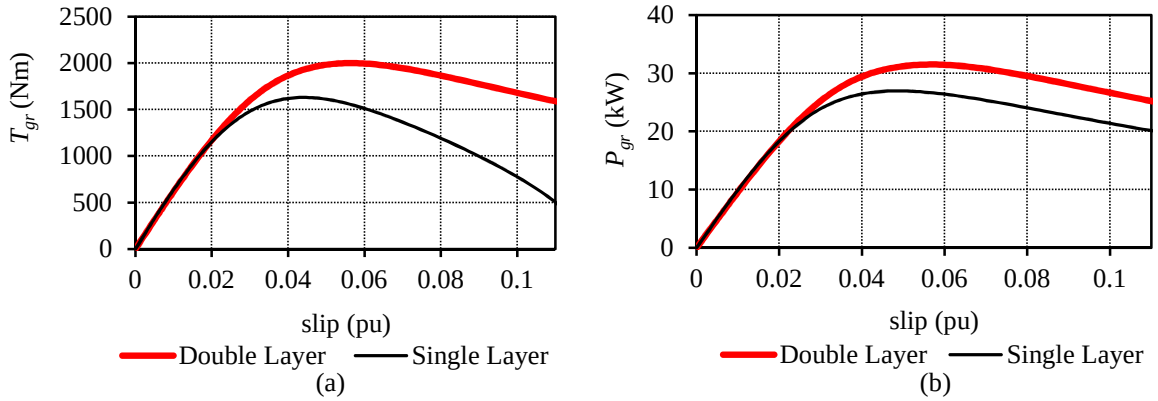

Figure 4.12: (a) IG torque and (b) power versus slip for the single layer and double layer winding configurations.

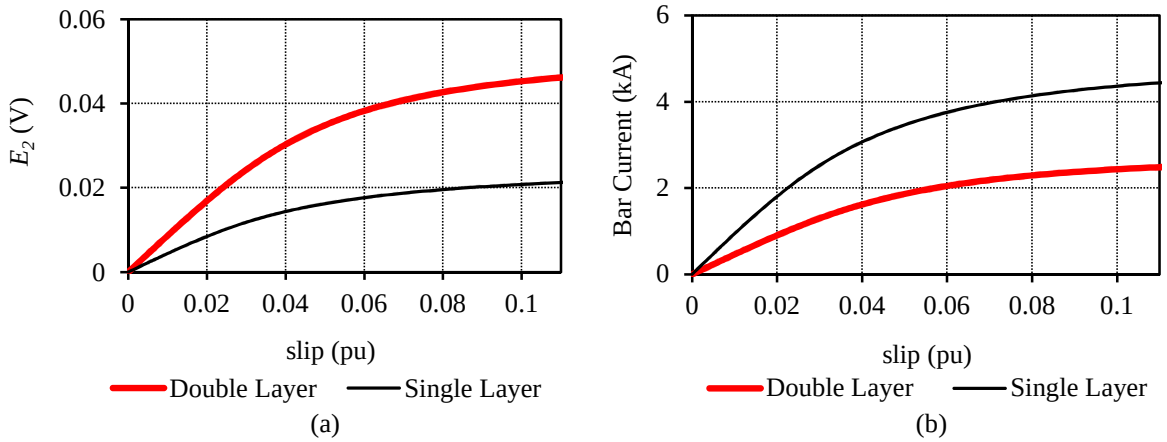

Figure 4.13: (a) IG induced voltage and (b) bar current versus slip for the single layer and double layer windings.

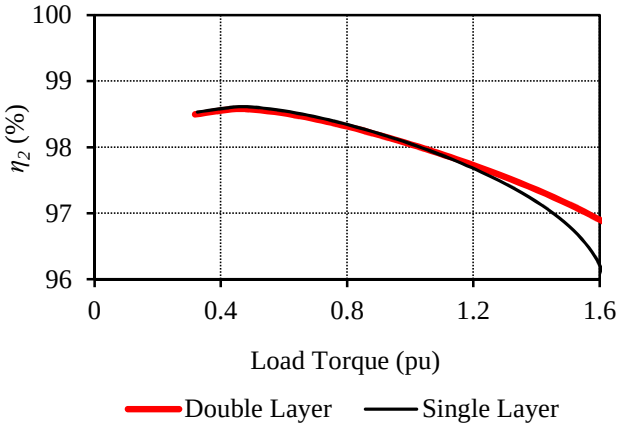

Figure 4.14: IG efficiency versus load torque for the single layer and double layer windings.

4.4.3 Single and double layer performance comparison

Table 7 gives some of the performance parameters of the IG for both the double layer and single layer windings. At the rated operating point there is no real difference between the two winding configurations. However, the double layer winding has a pull-out torque (T_b) of about 2.0 pu while the single layer winding can only attain a pull-out torque of about 1.6 pu. The latter can be attributed to the larger per unit inductance associated with the single layer winding.

Table 7: Single layer and double layer winding comparison for the IG at the rated operating point.

OUTPUT PARAMETER	UNIT	SINGLE LAYER	DOUBLE LAYER
Rated slip, s_r	%	1.71	1.69
Efficiency, η_2	%	98.02	98.03
Pull-out torque, T_b	Nm	1630	1999
Full load torque ripple, $\Delta\tau_L$	%	3.72	2.6
Per phase flux linkage, λ_2 (peak)	mWb.t	1.96	3.84
RMS induced per phase voltage, E_2	V	0.41	0.79
RMS induced bar current, I_2	kA	1.57	0.82
Per phase winding inductance, L_2	pu	0.35	0.29

4.5 IG design conclusions

The IG unit presented in this Chapter shows good performance under various load conditions. The rated torque of 1000 Nm is obtained at a slip value of about 1.7 %. Even though this machine is volumetrically smaller, it has a much higher efficiency, (η_2 > 98 %), than the SG unit. This results in an overall S-PMIG efficiency of higher than 92 %. The higher efficiency can be attributed to the use of solid bars instead of wound coils, which results in a much better filling factor.

As in the design for the SG, non-overlap windings are used to simplify the construction of the machine as well as to reduce the cogging torque. In addition single layer and double layer bar windings are investigated for the IG. At the rated operating point no real difference between the two winding configurations is observed. The single layer winding is especially attractive due to its much simpler construction. However, the double layer winding has a higher pull-out torque. It is still not certain what the required pull-out torque should be. With the IG operating at slip, short durations of over torque values higher than the machine's pull-out torque pose no real danger to the system. However, if the wind generator needs to shut down in high wind speed conditions the lower pull-out torque could pose a problem. The final system designed for in this particular case, is a fixed pitch system, which makes use of an electromagnetic brake by using a resistive dumping load. For this system it is, thus, necessary to specify a higher pull-out torque in order to ensure safe system operation.

If, however, a wind generator system is used with full pitch control and/or with a mechanical braking system, a lower pull-out torque can be specified. If a lower pull-out torque is specified, the single layer winding poses no real disadvantage. It is also observed that if a lower pull-out torque and efficiency is specified the size of the IG unit can be reduced significantly. For future applications, other winding configurations must also be investigated. Conventional overlap windings might have a better torque performance, which might lead to an even further reduction in the machine size, lessening the impact of adding a second direct-drive machine.

Chapter 5 – PMIG Dynamics

If the split S-PMIG is to be proposed as a directly grid-connected wind generation system, it is of extreme importance that this generator operates in a stable way under all wind speed conditions. In this next chapter the dynamic performance of the S-PMIG grid-connected system is evaluated.

5.1Per phase equivalent modelling

To gain a better understanding of the dynamic behaviour of the S-PMIG, a basic per phase equivalent circuit approach is first followed. For comparison reasons the same modelling is also done for a directly grid-connected PMSG, by removing the IG unit from the modelling procedures. From this analysis the differences between the behaviour of a directly grid-connected PMSG and the directly grid-connected S-PMIG can be more clearly understood. From this first approach it is also much easier to derive an approximate transfer function to explain the machine behaviour.

Several assumptions are made in order to represent the S-PMIG in a per phase equivalent model. First it is assumed that the mechanical time constant of the system is much longer than the electrical time constant. For the SG unit it is also assumed that the synchronous reactance is the dominant part of the impedance and the per phase resistance is, thus, neglected. For the IG part it is assumed that the machine operates in the linear torque slip region at small slip values. For a better understanding of the modelling done in this Chapter, Fig. 5.1 sheds some light on the mechanical and electrical interaction of the generator and the wind turbine. The per phase equivalent electric circuit for a directly grid and turbine connected PMSG is shown in Fig. 5.2(a). Fig. 5.2(b) shows the per phase equivalent electric circuit for the S-PMIG grid and turbine connected system.

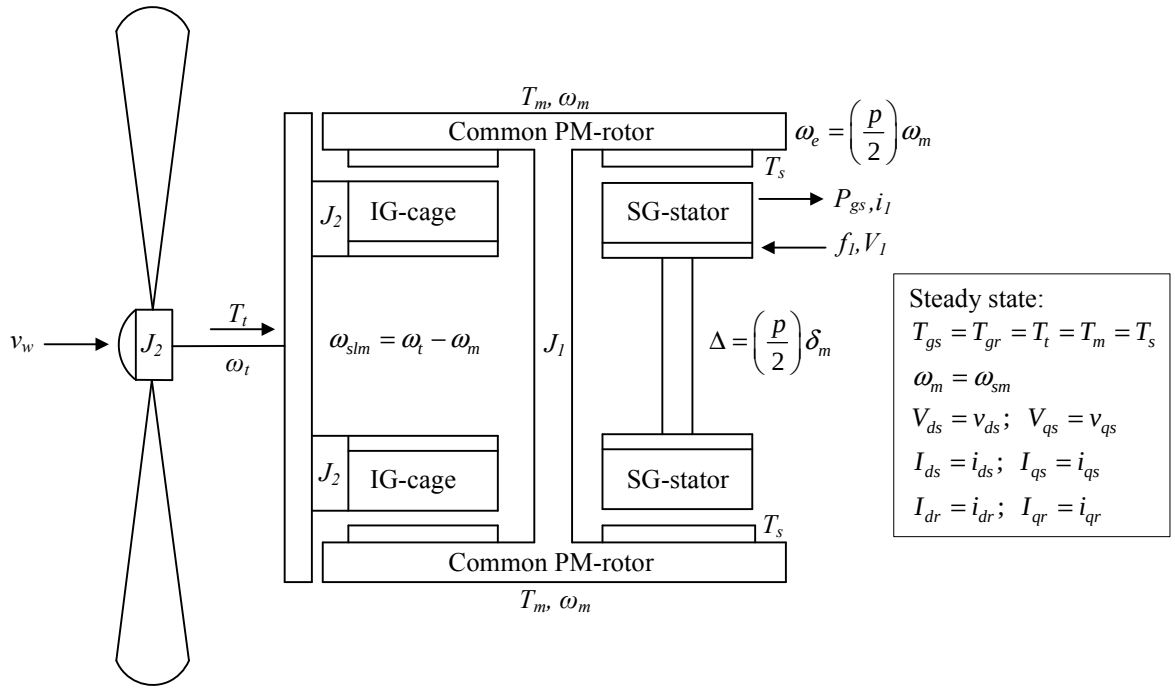

Figure 5.1: Overview of the mechanical and electrical interaction of the turbine and the generator.

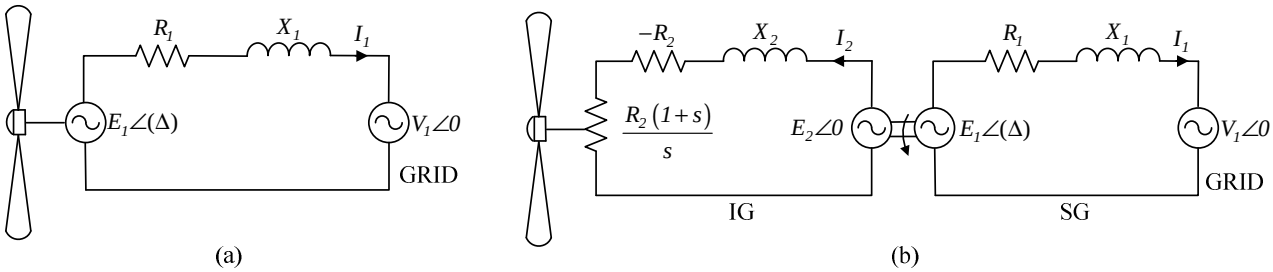

Figure 5.2: Per phase equivalent circuits: (a) directly grid-connected PMSG and (b) directly grid-connected S-PMIG.

5.1.1 Directly grid-connected PMSG

The effects of directly coupling a PMSG to the grid and turbine are investigated first. In this case the wind turbine shown in Fig. 5.1 is directly mounted to the PM-rotor and $T_m = T_t$. For the modelling of the PMSG, the turbine motion is described by (5.1) as

$$T_t - T_s = J_1 \frac{d\omega_t}{dt} \ . \tag{5.1}$$

In (5.1) T_t is the turbine torque and T_s is the electrical generator torque response. In this case the inertia (J_1) includes the inertia of both the turbine and the PM-rotor. The inertia of the turbine is found to be far more than that of the PM-rotor. The turbine speed which is also the speed of the PM-rotor if the PMSG is directly connected to the turbine, is given by ω_t. The turbine torque can be estimated as a function of the wind speed (v_w) and ω_t as,

$$T_t = f\left(v_w, \omega_t\right). \tag{5.2}$$

By omitting the per phase resistance the developed power of the PMSG can be approximated as

$$P_{gs} \approx \frac{E_1 V_1}{X_1} \sin(\Delta). \tag{5.3}$$

With power and torque directly equivalent the developed generator torque response is given by,

$$T_s \approx K_1 \sin(\Delta). \tag{5.4}$$

For small values of the power angle, Δ, $\sin(\Delta) \approx \Delta$ and if it is assumed that

$$E_1 \approx V_1 = \sqrt{2}\pi f_1 N_1 \phi_1 \text{ and it is known that } X_1 = 2\pi f_1 L_1, \tag{5.5}$$

the machine constant K_1 can approximately be expressed as,

$$K_1 \approx \frac{3pN_s{}^2\phi_1{}^2}{4L_1} \ . \tag{5.6}$$

In (5.6) ϕ_1 is the SG flux per pole and L_1 is the per phase winding inductance. Furthermore the power angle (δ_m = mechanical power angle in this case) dynamics are described by

$$\omega_t - \omega_{sm} = \frac{d\delta_m}{dt}; \quad \omega_{sm} = \frac{4\pi f_1}{p}; \ \Delta = \left(\frac{p}{2}\right)\delta_m. \tag{5.7}$$

From the above mentioned machine and turbine relationships, the basic dynamic block diagram in Fig. 5.3 is derived. From the block diagram in Fig. 5.3 it is possible to derive a steady-state transfer function as

$$\frac{T_s(s)}{T_t(s)} = \frac{\frac{K_1}{J_1 s^2}}{1 + \frac{K_1}{J_1 s^2}}. \tag{5.8}$$

To evaluate this transfer function it is written in the standard form for a second order system which is given by (5.9) as

$$\mathrm{H(s)} = \frac{\omega_n{}^2}{s^2 + 2\zeta\omega_n s + \omega_n{}^2} \tag{5.9}$$

which, for this particular case leads to the transfer function in (5.10) given as

$$\frac{T_s(s)}{T_t(s)} = \frac{\frac{K_1}{J_1}}{s^2 + 0s + \frac{K_1}{J_1}} \ . \tag{5.10}$$

Usually for conventional grid connected synchronous machines, damper windings are incorporated within the design to obtain a stable grid-connection. This is also the main focus of [8] where the spring and damper system is proposed to provide system damping. However in this case no additional damping is available and the damping coefficient ς is assumed as $\varsigma = 0$. This can be seen in (5.10) with $0 = 2\varsigma\omega_n$ and $\omega_n{}^2 = K_1/J_1$,

where ω_n is the undamped natural frequency. There will however be slight damping if the copper losses (P_{cus}), wind and friction losses (P_{wfs}), and the core and eddy current losses (P_{ecs}) of the machine are taken into account. This slight damping, however, has very little effect on the machine stability. From (5.10) it is, thus, clear that this is an undamped system, which means that oscillations will continue indefinitely. It is, thus, evident that the directly grid-connected PMSG will be very unstable if directly connected to a grid in a dynamically loaded system.

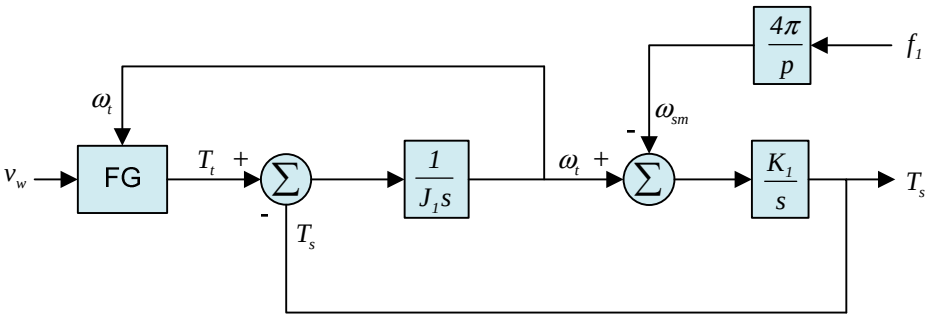

Figure 5.3: Per phase equivalent modelling of a PMSG directly connected to the turbine and the grid.

5.1.2 Directly grid-connected S-PMIG

The second case investigated is the directly grid-connected S-PMIG system. The grid-connected SG unit of the S-PMIG system can be modelled similarly to the grid connected PMSG described above. However, the turbine in this case is disconnected from the PM-rotor and the only inertia experienced by the SG unit is that of the common free rotating PM-rotor. The inertia of the turbine is moved to the IG unit, with J_2 including the inertia of both the turbine and IG cage-rotor. The torque relationships are now given as

$$T_t - T_m = J_2 \frac{d\omega_t}{dt} \text{ and } T_m - T_s = J_1 \frac{d\omega_m}{dt}. \tag{5.11}$$

In (5.11) T_m is the torque response of the common PM-rotor to changes in T_t. For the IG a linear relationship between the machine torque and slip is derived, which is assumed as

$$T_m = K_2 \omega_{slm} \text{ with } \omega_{slm} = \omega_t - \omega_m . \tag{5.12}$$

In [28] an expression for K_2 of (5.12) is derived as

$$K_2 = \left(\frac{3p^2 {N_r}^2}{8R_2} \right) {\phi_2}^2 \tag{5.13}$$

where ϕ_2 is the flux per pole of the IG unit. From (5.1) to (5.13) the approximate dynamic block diagram of the S-PMIG system is acquired as shown in Fig. 5.4. For the block diagram in Fig. 5.4 a steady-state transfer function for the S-PMIG is derived, with the resulting third order transfer function given in (5.14) as

$$\frac{K_1 K_2}{J_1 J_2 s^3 + K_2 J_1 s^2 + K_1 J_2 s + K_1 K_2}. \tag{5.14}$$

If all the closed loop poles of the transfer function in (5.14) are situated in the left half of the *s*-plane the system will be stable. From (5.14) it can, thus, be concluded that a stable directly grid-connected system is possible if the IG unit is incorporated within the design.

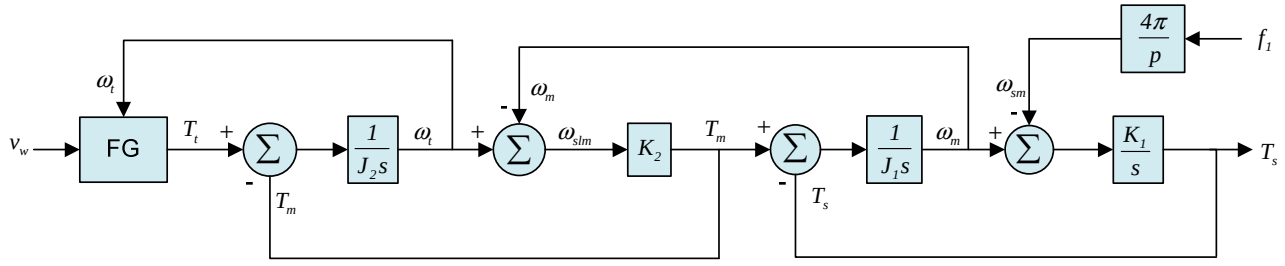

Figure 5.4: Per phase equivalent modelling of anS-PMIG system directly connected to the turbine and the grid.

5.2 Modelling in the *dq* reference frame

Although section 5.1 already shows that the S-PMIG can offer a stable grid connection, a more accurate system response is calculated by modelling the S-PMIG system in the *dq* reference frame. Again for comparison the same modelling is done for a directly grid and turbine connected PMSG, with the *dq* equivalent block diagram of the directly grid and turbine connected PMSG system shown in Fig. 5.5.The block diagram for the dynamic modelling of the S-PMIG system is shown in Fig. 5.6(a) with the *dq* equivalent model of the IG shown in Fig. 5.6(b). For the SG modelling in the S-PMIG system the PMSG model in Fig. 5.5 is used with ω_t replaced by ω_m and T_t replaced by T_m.

The steady-state *dq* equivalent modelling of the SG and IG is already extensively described in Chapters 3 and 4 where it is used for the FE design and analysis of these machines. These models are also used for the dynamic modelling as shown in Figs. 5.5 and 5.6. The *dq* current and voltage response of the SG is given by i_{ds}, i_{qs}, v_{ds} and v_{qs} and the *dq* current response of the IG is given by i_{dr} and i_{qr}.

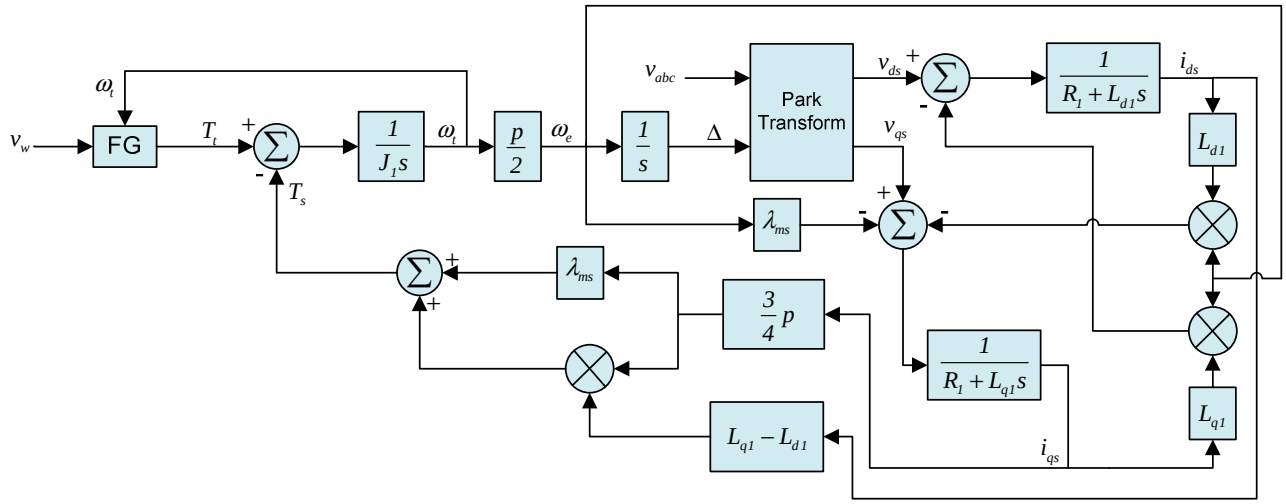

Figure 5.5: Dynamic modelling of a PMSG directly connected to the turbine and the grid in the *dq* reference frame.

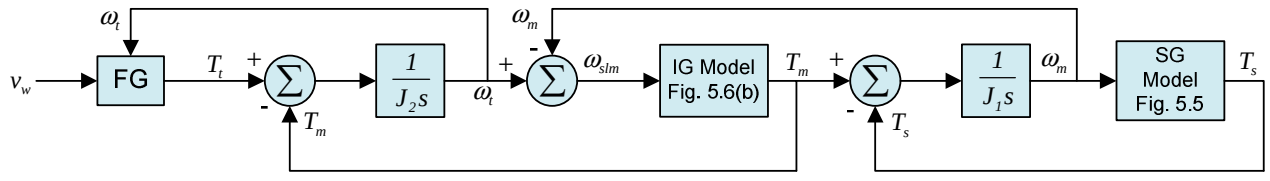

(a)

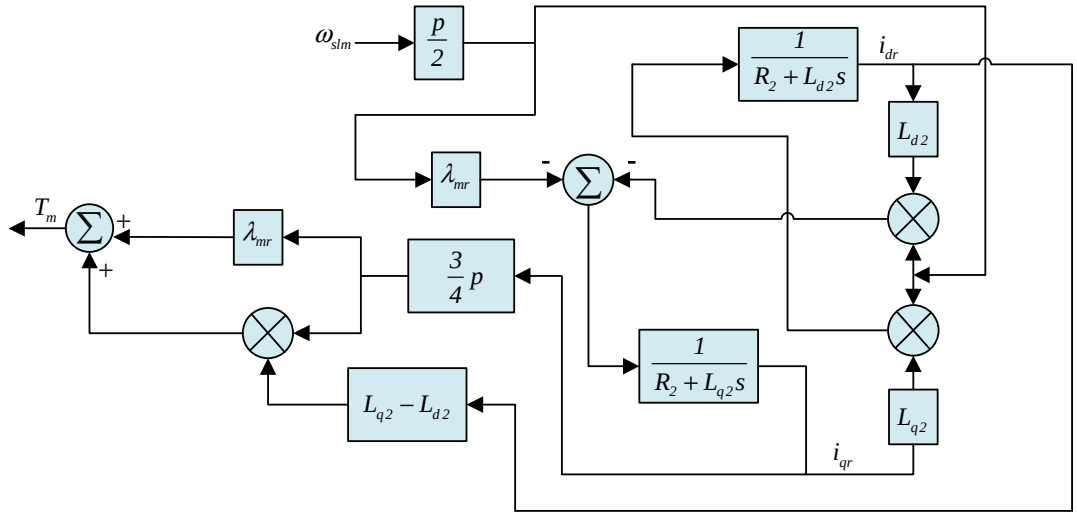

(b)

Figure 5.6: (a) Dynamic modelling of the S-PMIG directly connected to the turbine and the grid, with (b) the IG model in the *dq* reference frame.

5.3 System response results

The grid-connected system response is evaluated by applying a step input in the wind speed, which corresponds to a step input in the applied turbine torque. In this investigation a worst case scenario is taken where the torque step input applied is from zero to the rated machine torque. In a real case scenario the torque step will seldom be as instantaneous as used in this case. System response results are shown for both the PMSG and the S-PMIG directly connected to the grid and turbine.

5.3.1 Directly grid and turbine connected PMSG

Fig. 5.7 shows the torque step response of the directly grid-connected PMSG. Clearly seen in Fig. 5.7 is the undamped nature of the directly connected PMSG with a settling time of $t_s > 200$ s. Shown in Fig. 5.8 is the electrical speed response of the PM-rotor (ω_e).The variation of the per phase RMS grid current is shown in Fig. 5.9. Due to the transient nature displayed by the directly turbine and grid-connected PMSG, it would be impossible to connect such a system directly to the grid in a wind generation setup. The oscillations in speed and torque will put a tremendous load on the mechanical supporting systems, while the grid current variations will be unacceptable in a grid-connected system.

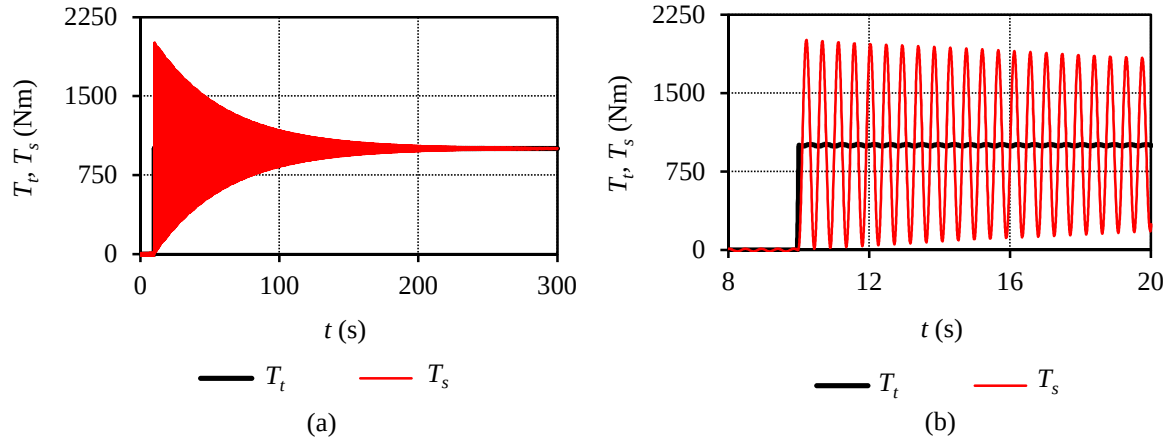

Figure 5.7: (a) Torque response of the directly grid connected PMSG to a step input in wind speed, with (b) showing the response up until the first 10 s after the step is applied.

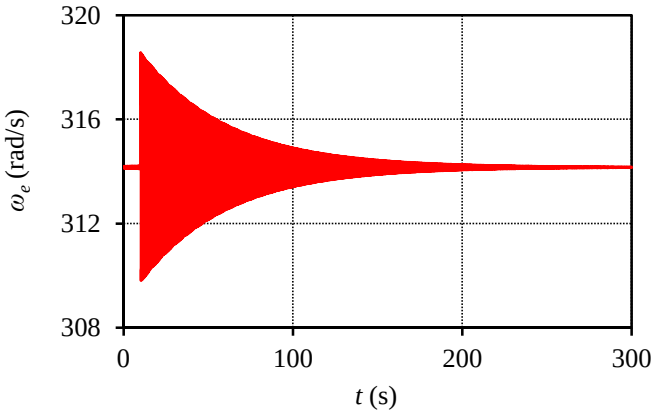

Figure 5.8: Electrical speed response of the PM-rotor of a directly grid connected PMSG to a step input in wind speed.

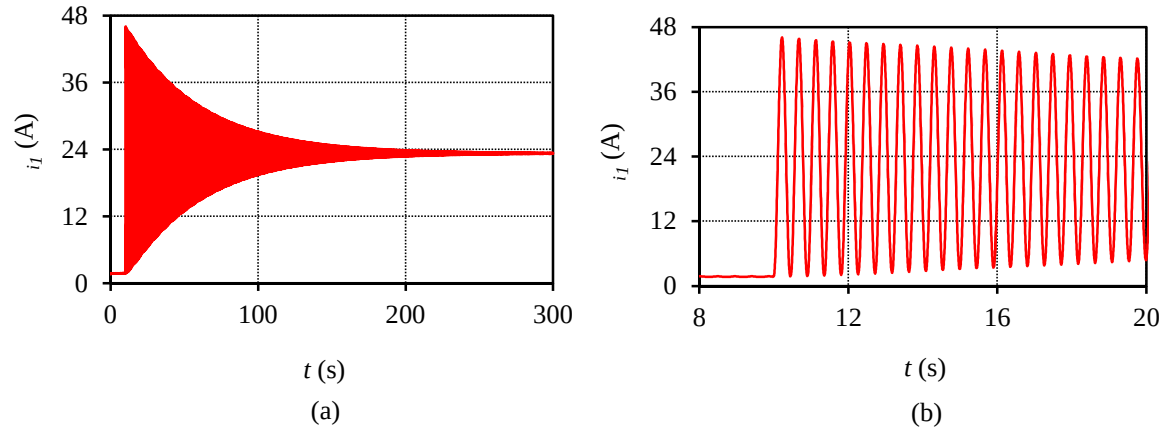

Figure 5.9: Per phase RMS current response of the directly grid connected PMSG to a step input in wind speed, with (b) showing the response up until the first 10 s after the step is applied.

5.3.2 Directly grid and turbine connected S-PMIG

Fig. 5.10(a) shows the torque response of the directly grid-connected S-PMIG system. In this case the torque input of the turbine (T_t), the response of the PM-rotor torque (T_m) and the SG torque response (T_s) are shown. The much more stable behaviour of the system as opposed to the directly turbine and grid-connected PMSG system is clearly seen. A significantly reduced overshoot, as well as a much shorter settling time of $t_s < 1$ s is obtained. Fig. 5.10(b) shows the S-PMIG torque response for an increase in the IG cage-rotor resistance, which in turn increases the rated slip of the machine. In this case aluminium instead of copper is used for the IG cage-rotor bars. With the increase in resistance an overshoot of almost zero occurs, as shown in Fig. 5.10(b).

Fig. 5.11(a) shows the electrical speed response (ω_e) of the common free rotating PM-rotor linking the two machines. The response of the electrical power angle (Δ) is shown in Fig. 5.11(b) and the per unit slip response of the IG cage-rotor is shown in Fig. 5.12. The response of the phase current fed into the grid by the S-PMIG is shown in Fig. 5.13. With no oscillatory behaviour and no sudden current increases, the current characteristics shown in Fig. 5.13 should be acceptable within a grid connected system.

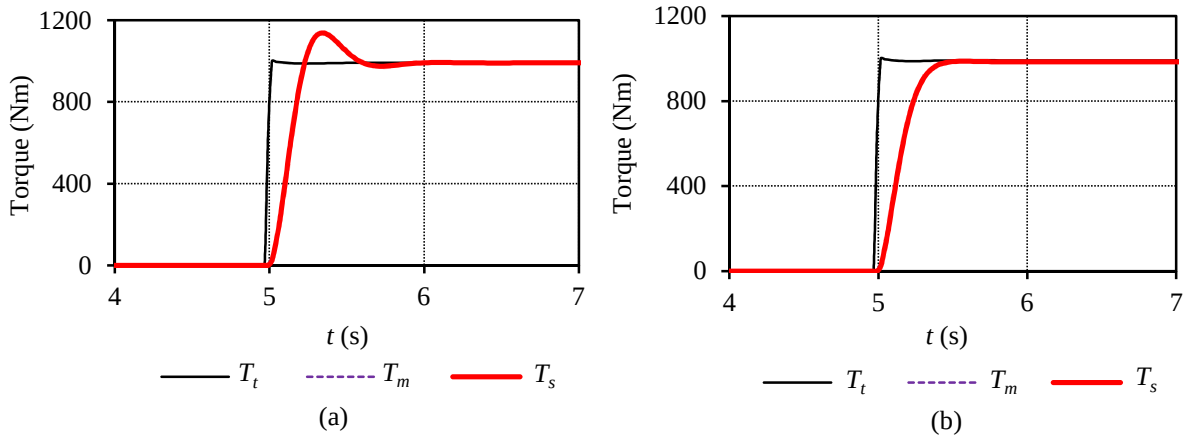

Figure 5.10: Torque response of the directly grid-connected S-PMIG system with (a) copper rotor bar windings and (b) aluminium rotor bar windings for a step input in wind speed.

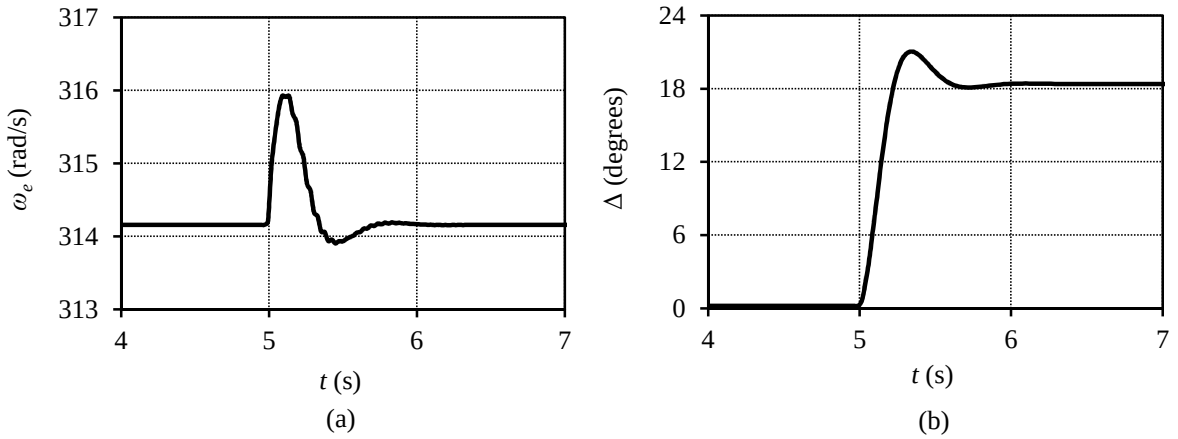

Figure 5.11: (a) Electrical speed and (b) electrical power angle response of the directly grid-connected S-PMIG system to a step input in wind speed.

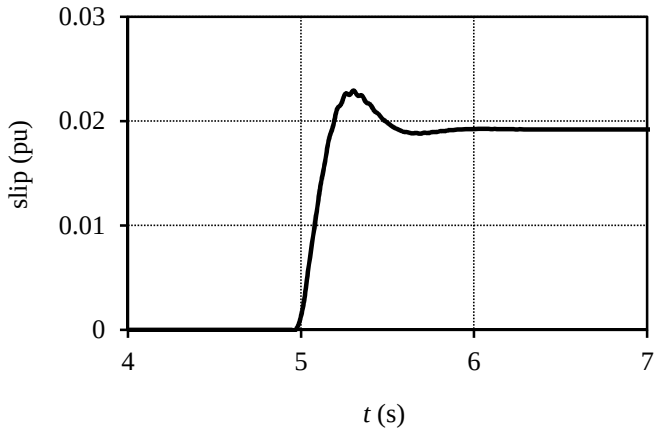

Figure 5.12: Slip response of the IG cage-rotor of the directly grid connected S-PMIG system to a step input in wind speed.

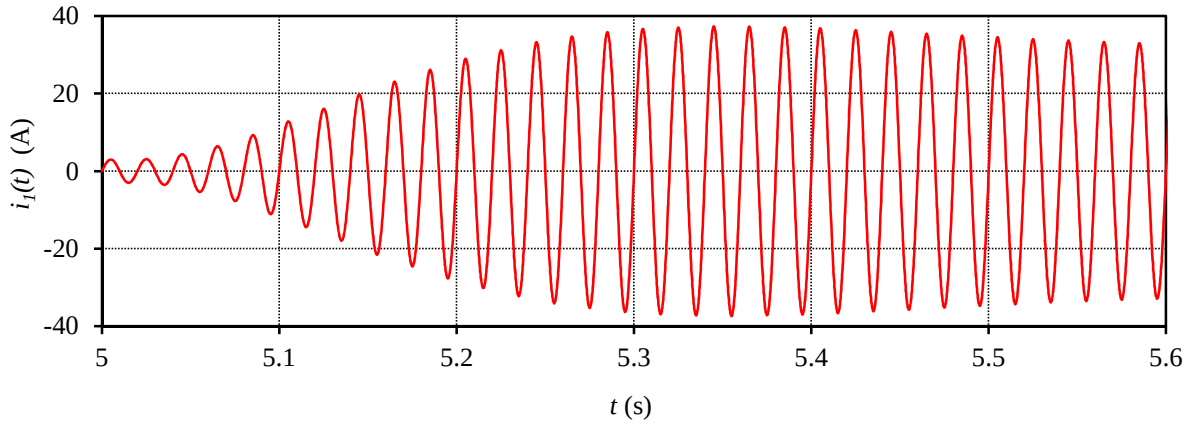

Figure 5.13: Response of the grid current to a step input in wind speed for the directly grid connected S-PMIG system.

5.4 More grid connection aspects

From the data presented thus far it is evident that the S-PMIG will operate in a much more stable way as a directly grid-connected system. However, several other grid connection factors, like low voltage ride through capability during grid faults and reactive power control should be looked at as well.

With the use of the S-PMIG system, the grid will in effect "see" a directly connected PMSG. If a drop in supply voltage occurs the synchronous machine will immediately attempt to support the terminal voltage by providing capacitive reactive power to the grid. However, with a sudden dip in the voltage the reactive currents induced by the PM machine could be very large, which could pose a grid stability problem. On the

other hand the SG design proposed in this study makes use of a non-overlap single layer winding, which is known to have a large inductance. The larger synchronous impedance due to this inductance could act as a buffer during low voltage conditions and limit the current flow from the machine during these conditions. Further studies, however, are still needed to confirm this. The voltage supporting capabilities of the directly connected PMSG are also mentioned in [7] where a synchronous machine is directly connected to the grid by means of a hydro-dynamically controlled gearbox. In this study the concept displayed favourable characteristics regarding grid stabilization during fault conditions.

By decoupling the turbine from the SG as in an S-PMIG, several wind turbine oscillatory effects which cause voltage flickering, can be eliminated as well. The S-PMIG system was found to damp several of these unwanted frequency bands occurring in a wind generating system, like tower shadowing and yawing error effects. This is shown in Fig. 5.14, where an approximated tower shadowing effect is added to the mechanical input torque of the system. From Fig. 5.14 it is seen that this effect is almost completely filtered out by the simulated S-PMIG system.

To start-up the S-PMIG in a wind generation system, the IG-cage rotor is brought up to synchronous speed by the turbine. With no load connected to the SG, the common PM-rotor follows the cage-rotor at almost zero slip. To synchronise the S-PMIG with the grid a synchronising controller is employed, which is currently being developed. As soon as the common PM-rotor reaches synchronous speed, the controller maintains the S-PMIG at this speed by connecting it to a resistance load through an active switch. The moment the induced voltage of the S-PMIG and the grid voltage are in phase the S-PMIG is synchronised with the grid. A very basic overview of the S-PMIG with the synchronising controller is shown in Fig. 5.15.

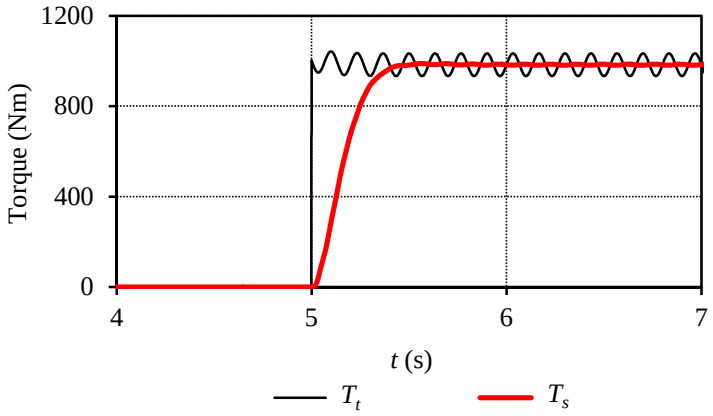

Figure 5.14: Torque response of the directly grid connected S-PMIG system with aluminium rotor bar windings for a step input in wind speed and with an approximated tower shadowing effect incorporated in the simulated torque input.

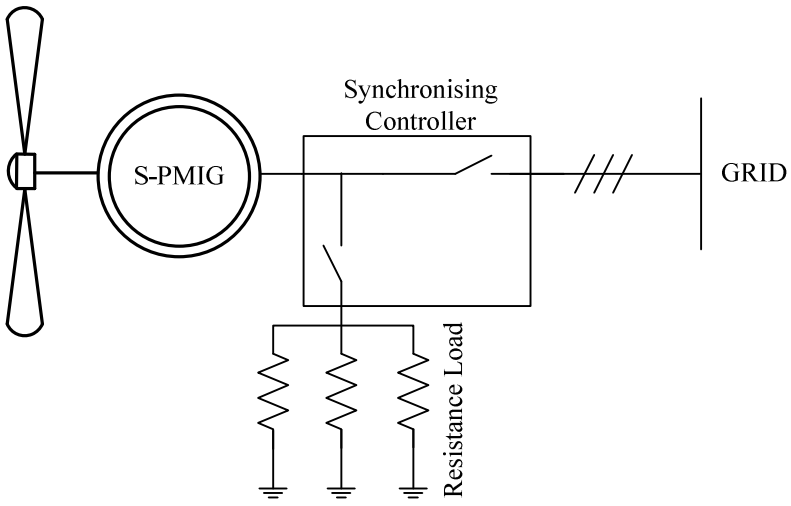

Figure 5.15: Synchronising controller used to synchronise the S-PMIG with the grid.

Chapter 6 – Practical Measurements

The practical measurements presented in this chapter are an attempt to validate the prototype generator designs proposed in Chapters 3 and 4 as far as possible. The laboratory testing is done in two iterations. As a first investigation the SG unit is tested as a conventional PMSG. This includes the tests done on the PMSG in combination with a solid state converter (SSC). For the second investigation the IG unit is mounted to the front of the SG and the S-PMIG concept is evaluated to a further extent.

The laboratory measurement setup is shown in Fig. 6.1. A 75 kW induction machine (shown in Fig. 6.2) is fed by a frequency inverter to allow for variable speed operation. A gearbox is used to match the torque and speed characteristics of the low speed PM wind generator, and a torque transducer is fixed between the electrical generator and the drive system to measure the simulated wind turbine torque. As shown in Fig. 6.1, the tested generator can be connected directly to the grid, or to the grid via the SSC or to a resistance load. Fig. 6.3 shows the PMSG mounted on the test bench, which is connected to the grid via the SSC shown in Fig. 6.4. To assemble the S-PMIG, shown on the test bench in Fig. 6.5, the IG unit shown in Fig. 6.6 is mounted to the front of the SG unit in Fig. 6.3. Shown in Fig. 6.7 is the field testing of the PMSG directly connected to the wind turbine and to the grid via the SSC.

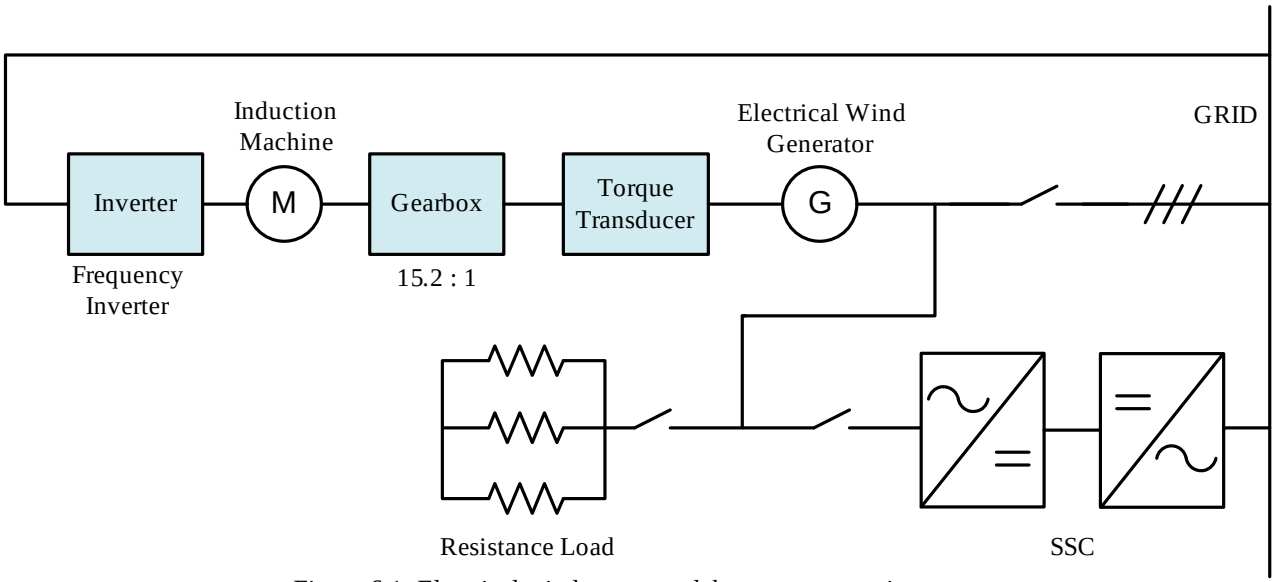

Figure 6.1: Electrical wind generator laboratory measuring setup.

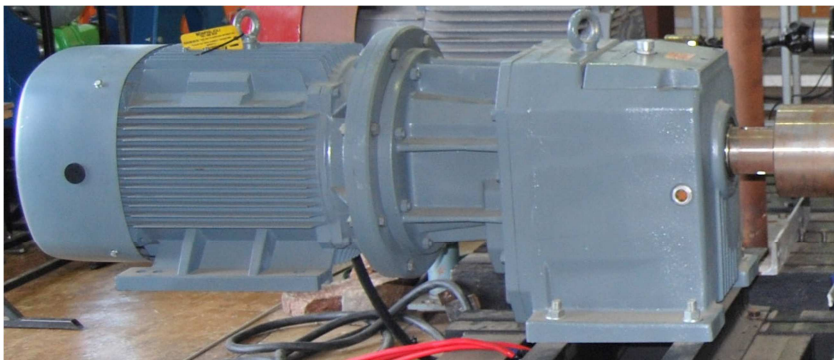

Figure 6.2: 75 kW 4-pole Induction machine, with 15.2:1 ratio gearbox used as a prime mover.

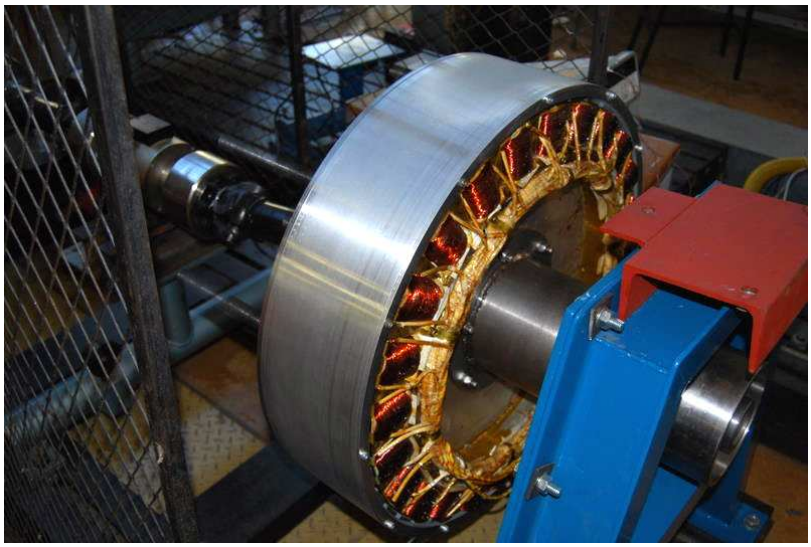

Figure 6.3: PMSG on the test bench.

Figure 6.4: Solid state converter (SSC) used to control the direct-drive PMSG.

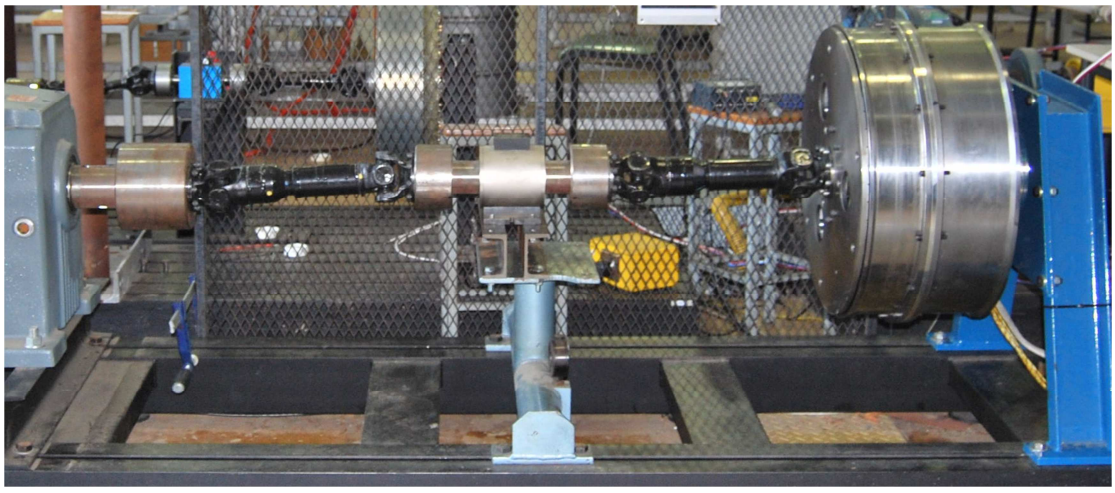

Figure 6.5: S-PMIG on the test bench, shown on the right, connected to the gearbox, shown on the left, through the torque transducer shown in the middle.

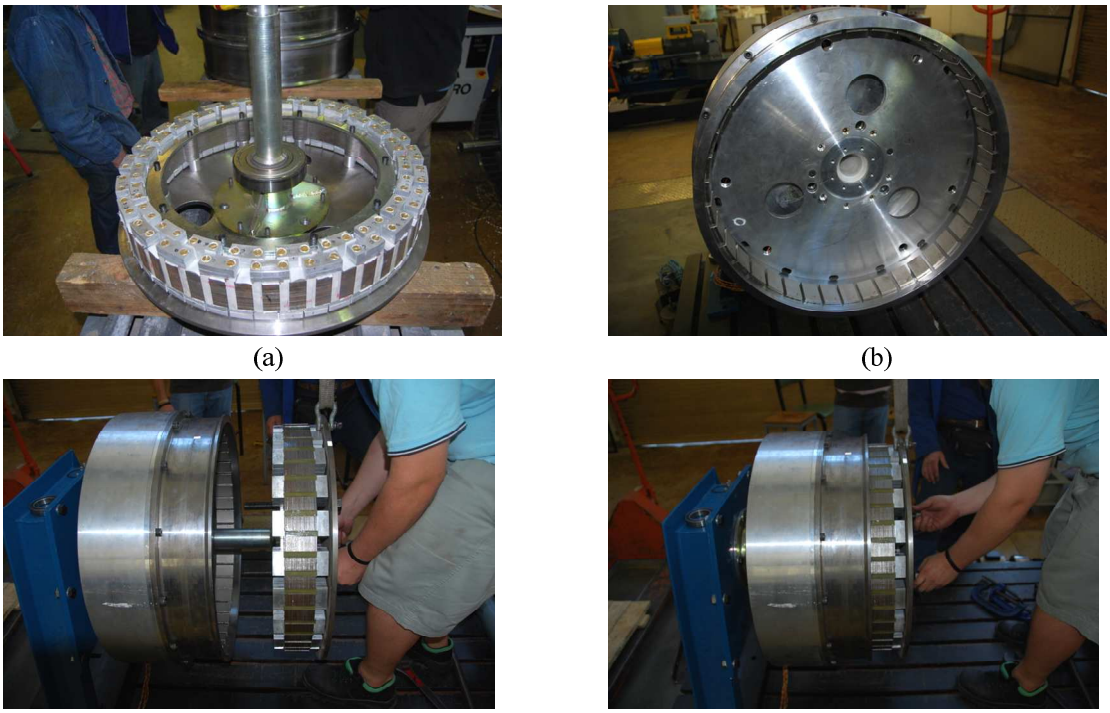

(a) (b)

(c) (d)

Figure 6.6: Assembling of S-PMIG: (a) IG cage-rotor; (b) IG side of common PM-rotor fixed to the SG PM-rotor; (c) and (d) IG cage-rotor being mounted to the front of the SG unit.

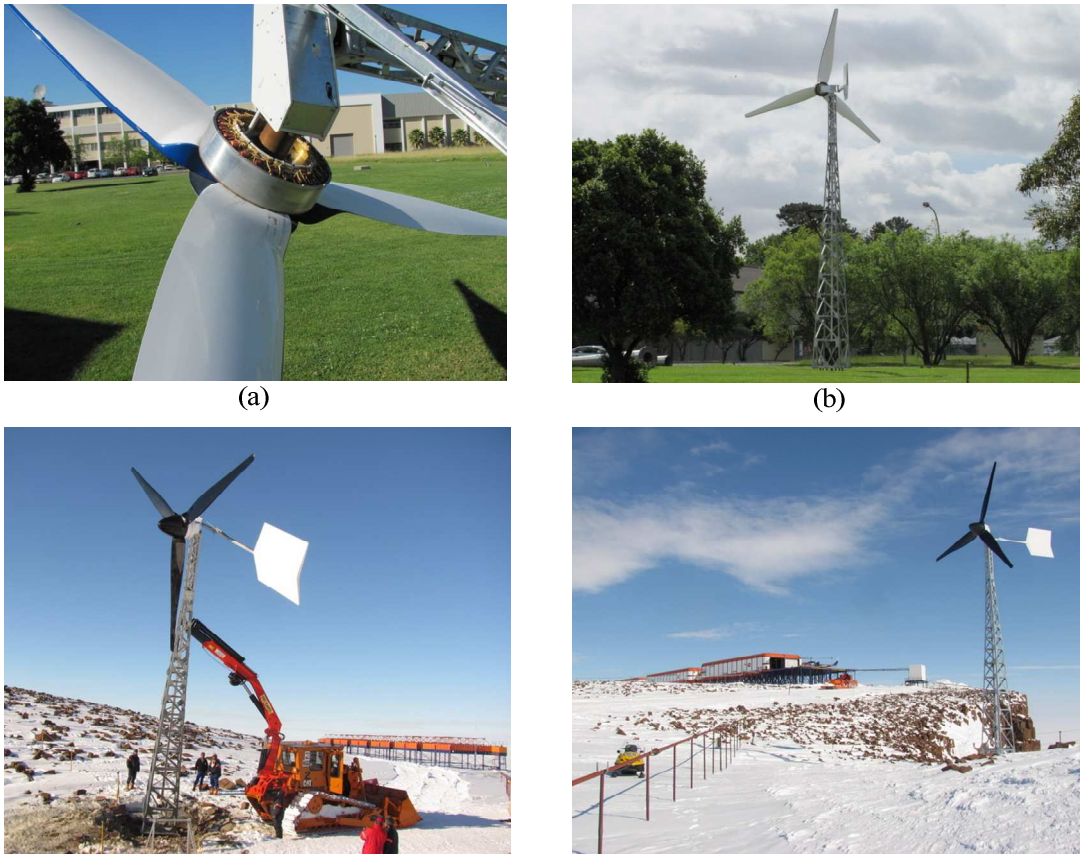

(a) (b)

(c) (d)

Figure 6.7: Field testing of SSC-fed PMSG wind generation system with, (a) wind turbine blades mounted directly to PM-rotor of PMSG, (b) testing of PMSG system at the University of Stellenbosch wind turbine site and (c) and (d) final SSC-PMSG wind turbine system installed at the South African National Antarctic Base (SANAE IV).

6.1 SG open and short-circuit measurements

Fig. 6.8(a) shows the open-circuit per phase RMS voltage measured at the SG stator terminals, where good correlation between the FE predicted and the measured voltage is obtained. The current versus speed with the SG stator terminals shorted are shown in Fig. 6.8(b). From Fig. 6.8(b) it is seen that the FE predicted short-circuit current is far more than the measured short-circuit current. In this case a third FE package, Maxwell v13 (FE-3), is also used for verification. In Fig. 6.8(b) it is shown that all three FE packages predict this much higher short-circuit current.

From the short circuit test an approximate value for X_1 is calculated with $Z_1 = R_1 + jX_1$ and $Z_1 \approx V_{oc}/I_{sc}$. The per phase resistance at no load is measured as R_1 = 0.3 Ω and at the rated operating temperature it is measured as R_1 = 0.38 Ω, which is predicted the same by FE calculations. With Z_1 and R_1 known the per phase inductance (L_1) can be calculated knowing that $X_1 = 2\pi f_1 L_1$. From the short-circuit inductance calculations Fig. 6.9 shows the measured - and the FE calculated per phase inductance. FE calculations predict L_1 at a bit more than 10 mH, while the short-circuit measurements give L_1 as about 15 mH on average. The actual per phase inductance of the machine is thus, about 1.5 times the FE predicted inductance.

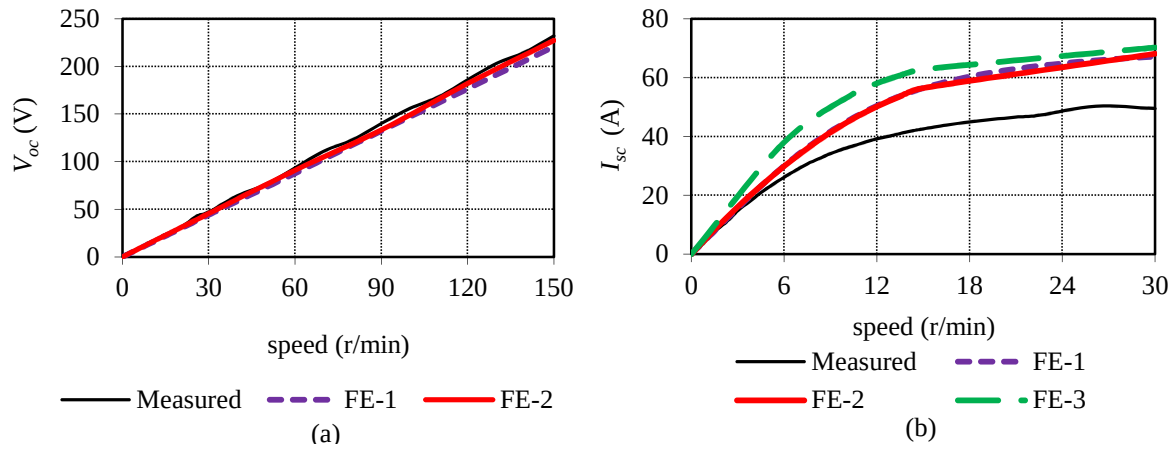

Figure 6.8: FE calculated - and measured PMSG (a) open-circuit voltage and (b) short-circuit current versus rotor speed.

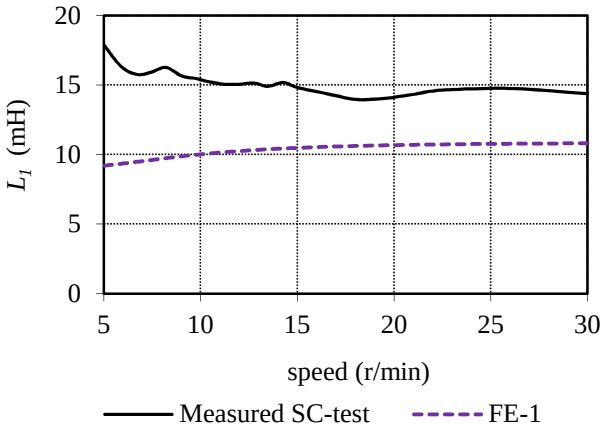

Figure 6.9: FE calculated and measured PMSG per phase inductance (SC-test).

6.2 Voltage quality

With the use of a non-overlap single layer winding configuration for the SG, a large harmonic content is present in the voltage waveform. The harmonics are clearly seen in the open-circuit voltages shown in Fig 6.10, with (a) the phase voltage and (b) the line voltage measured at the SG terminals. The harmonics present in the phase and the line voltage waveforms are shown in Fig. 6.11, with the limits for each of the different harmonics imposed by the local utility also shown. From Fig. 6.11 it can be seen that although a significant harmonic content is present in the voltage waveforms, the machine complies with the limits specified by the local utility as given in [43]. The THD of both the phase and line voltage waveforms are calculated at 4.29 % and 3.79 % respectively, which is well below the limit of 8 % imposed by [43] and also much less than predicted in Chapter 3.

Fig. 6.12shows the phase and line voltage waveforms measured at rated load, with the SG connected to a resistance load. Also shown in Fig. 6.12(a) is the per phase rated load current. From Fig. 6.12 it can be seen that the voltage waveforms are significantly less distorted under load, especially the line voltage in Fig. 6.12(b).

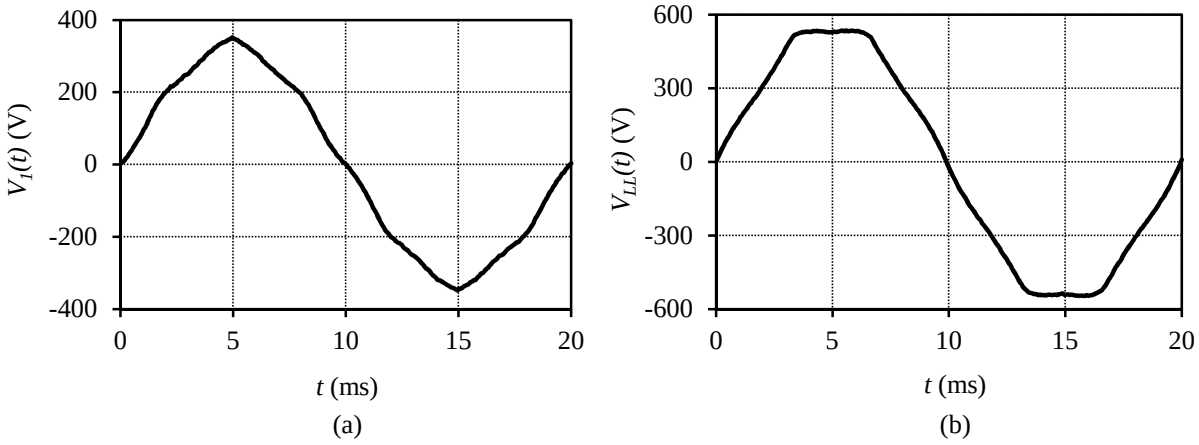

Figure 6.10: Measured open circuit (a) phase and (b) line voltage waveforms measured at the SG terminals.

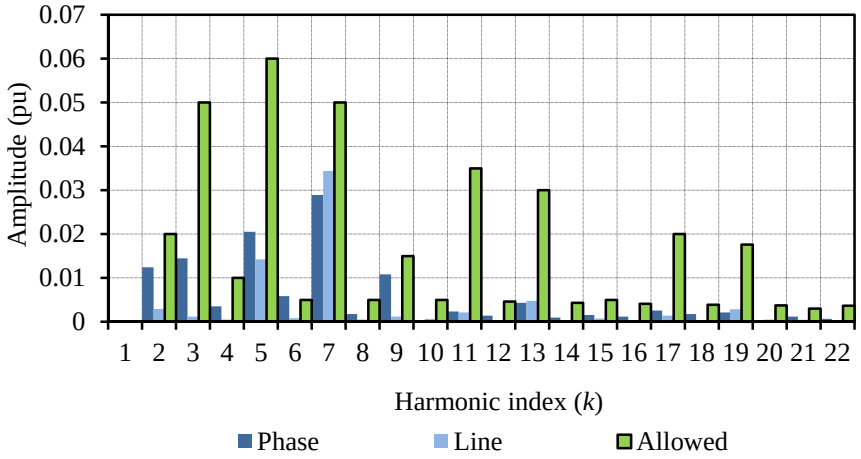

Figure 6.11: Harmonic components in the open circuit line and phase voltage waveforms measured at the SG terminals.

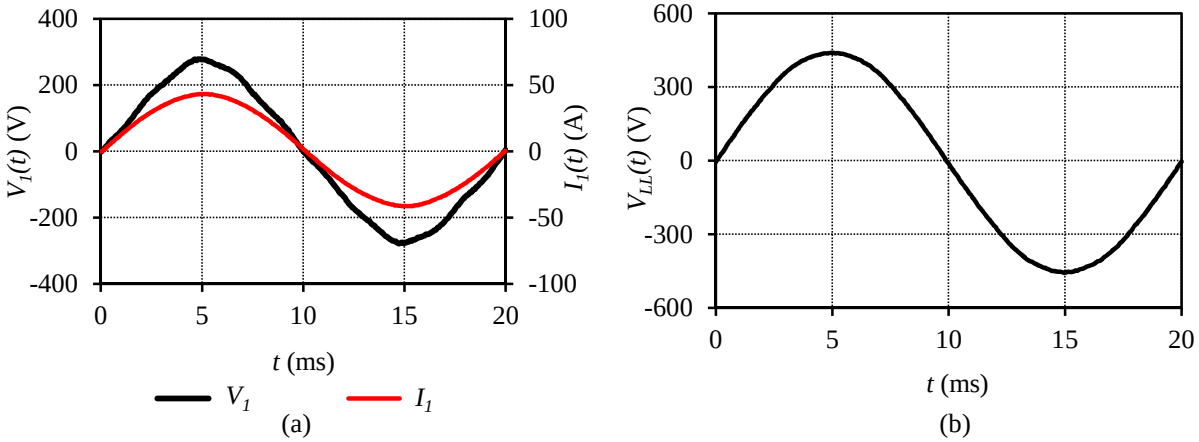

Figure 6.12: (a) Phase voltage and current and (b) line voltage waveforms measured at the SG terminals with the SG connected to a resistance load.

6.3 No-load cogging torque evaluation

As previously mentioned an important machine parameter in wind generator design is the cogging torque. This is a very difficult parameter to measure accurately. Due to the sensitivity of the cogging torque to dimensioned parameter changes as explained in Chapter 3, it is very important to construct and assemble a machine as accurately as possible. Even slight construction and assembly errors can change the cogging torque quality significantly.

It is also not possible to measure the cogging torque parameter with the use of the full drive train due to several dynamic effects contained within the whole drive train test setup. For the most accurate measurement result a static measurement method as indicated in Figs. 6.13 and 6.14 is proposed. This method also eliminates all transient effects within the machine itself, which means that only the cogging torque is measured. To measure the cogging torque the rotor angle is varied in discrete static steps and the static torque reading is taken at each discrete step. As shown in Figs. 6.13 and 6.14 the rotor angle is varied by applying a vertical force to the torque beam, which is connected to the machine shaft. The rotor angle can be calculated knowing that the distance from the shaft centre to the torque beam adjuster is fixed. The height to which the torque beam is set at the adjuster side corresponds to a specific rotor angle. By adjusting the torque beam in 1 mm height steps it is possible to obtain an angular measurement step of almost 0.1°. To ease the taking of measurements it is advised that a counter weight is added to the machine rotor. The torque offset, which can be subtracted afterwards, allows for the measurement of only positive torque values.

Fig. 6.15(a) shows the no-load cogging torque measurement of the PMSG together with the FE-predicted no-load cogging torque calculated by FE-1. In Fig 6.15(b) the measured - and the FE predicted no-load cogging torque of the IG unit are shown.

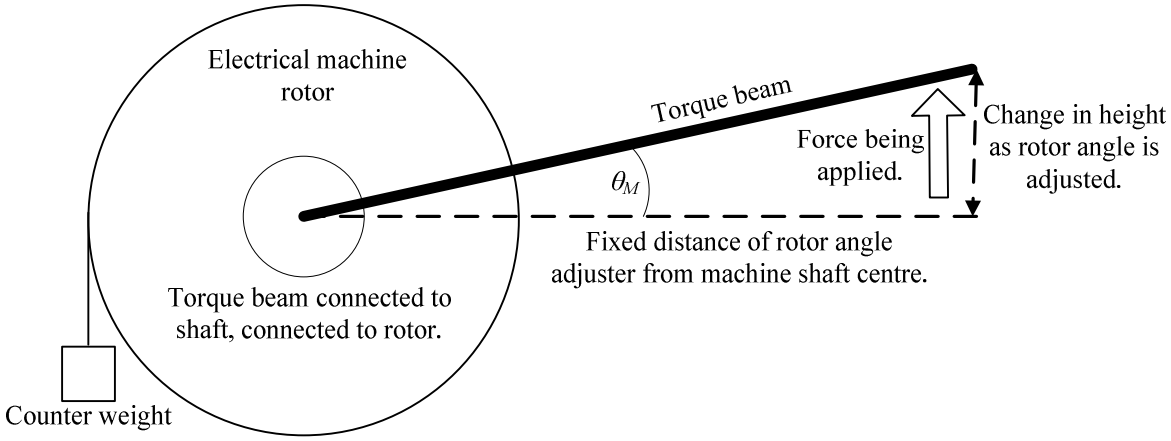

Figure 6.13: Static torque measurement setup schematic.

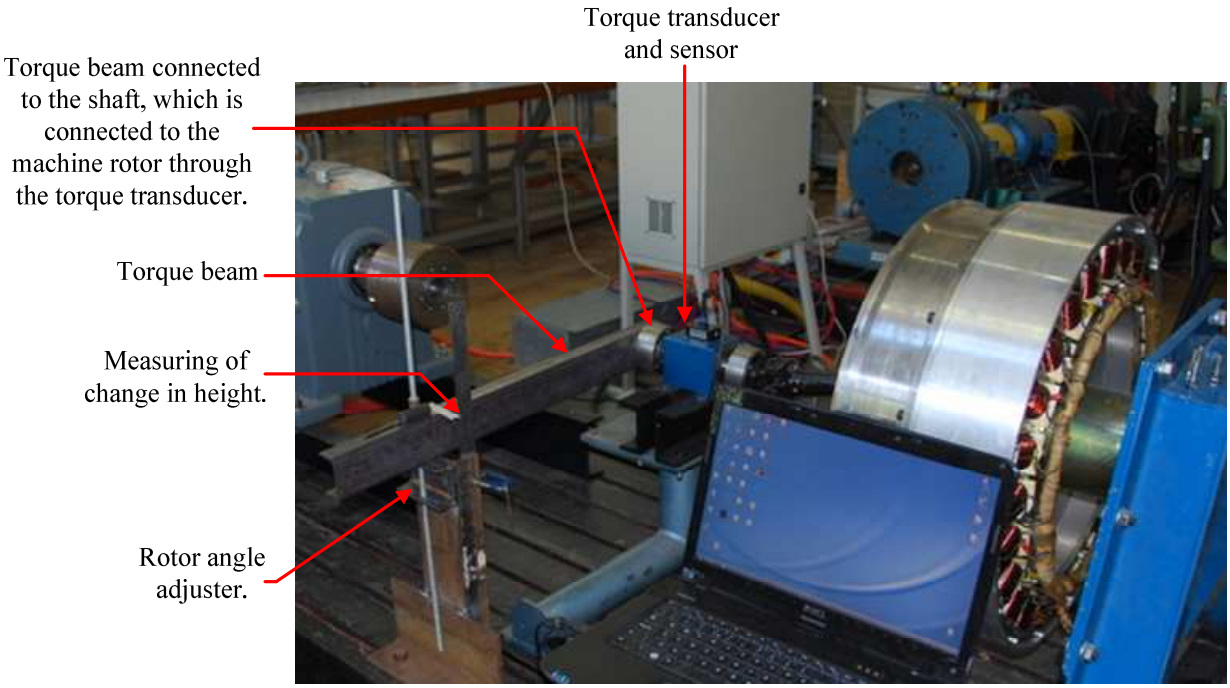

Figure 6.14: Static torque measurement setup with the drive train disconnected and the rotor angle adjuster connected to the shaft connecting the torque sensor.

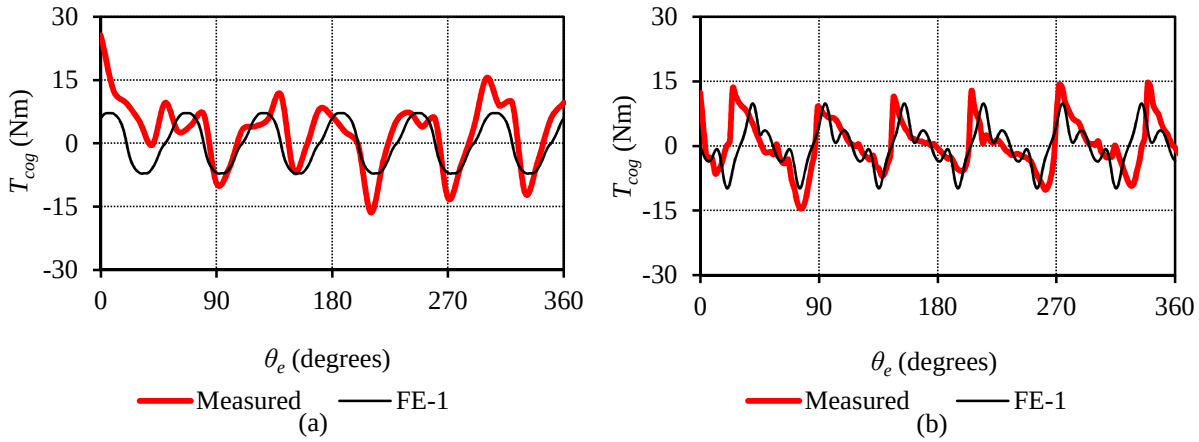

Figure 6.15: Measured - and FE predicted no-load static torque versus the rotor electrical position of (a) the PMSG and (b) the IG unit.

6.4 PM-rotor evaluation

The practical analysis in this section is included to determine whether it is feasible to use solid rotor yokes and magnets. This analysis is only conducted for the PMSG, as the only losses incurred in the IG unit are conductive losses and the type of rotor and PMs used is thus irrelevant to the performance of the IG. The rotor configurations are based upon the work done in [38]. Four rotor configurations are evaluated as defined in Table 8 and shown in Fig. 6.17.

Rotor-1 shown in Fig. 6.17(a) consists of a solid rotor yoke with solid permanent magnets which should be the easiest and most cost effective to manufacture. Rotor-2 shown in Fig. 6.17(b) has exactly the same yoke as Rotor-1 but the magnets are partially segmented in this case. The partially segmented magnets as shown in Fig. 6.16(a) are manufactured in the same way as normal solid magnets, but slits which are not completely cut through are added on both sides. This is unlike conventional segmented magnets shown in Fig. 6.16(b) where the magnets are completely segmented and the pieces glued together. Rotor-3 as shown in Fig. 6.17(c) consists of a solid yoke with solid magnets, but in this case the yoke is partially segmented with several

small slits located on its circumference. Rotor-4 shown in Fig. 6.17(d) is of the conventional type, with a laminated yoke. The magnets used for Rotor-4 are partially segmented as shown in Fig. 6.16(a). In Fig. 6.17(d) the laminations are stacked inside a hub, while for the solid rotors no hub is necessary with the yoke forming part of the mechanical structure. This results in less material being used for the solid rotor yokes.

To test the differences in PMSG loss and efficiency of these four PM-rotors, a separate test is run for each with the same stator. A first measurement at no-load is taken to obtain the no-load losses of the PMSG with each rotor. This measurement is shown in Fig. 6.18(a). It should be noted that this measurement includes the no-load stator losses. The much higher losses of the solid rotor yokes are clearly observed if compared to the losses of the laminated yoke. A slightly better performance is obtained if the partially segmented magnets are used, but no improvement is observed for the use of the partially segmented rotor yoke. In Fig. 6.18(a) it is seen that the losses in Rotor-3 are even more than those of Rotor-1. However, this could be due to the measuring setup, as Rotor-3 was measured with a different torque sensor than the sensor used for the other rotor configurations.

Fig. 6.18(b) shows the efficiencies at rated load for the four different rotors. In this case the efficiency of the laminated rotor yoke is significantly better than that of all the other rotor configurations. For the PMSG it is not feasible to use any of the rotor configurations other than Rotor-4. The partially segmented magnets do have performance and manufacturing advantages, but more information is needed on the structural strength of these magnets as opposed to solid and conventional completely segmented and assembled magnets. It should also be noted that the non-overlap single layer winding contributes largely to the yoke and magnet losses due to the large sub-MMF harmonics associated with this winding type. Better results are expected if a different winding configuration, for instance a double layer winding, is used.

Table 8: Different PM rotor configurations.

PM Rotor	Description
Rotor-1	Solid yoke and solid magnets
Rotor-2	Solid yoke and partially segmented magnets
Rotor-3	Partially segmented yoke and solid magnets
Rotor-4	Laminated yoke and partially segmented magnets

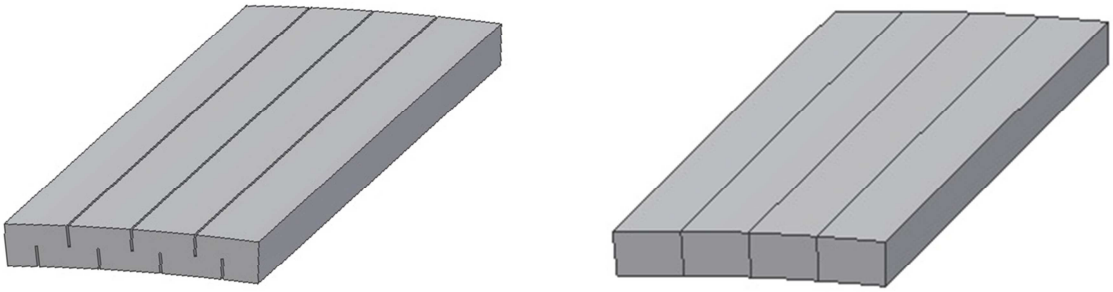

(a) (b)

Figure 6.16: (a) Partially segmented PM and (b) completely segmented and assembled PM [38].

(a)

(b)

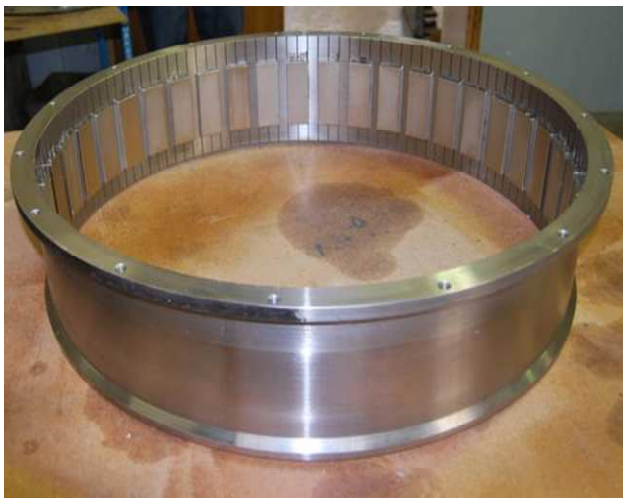

(c)

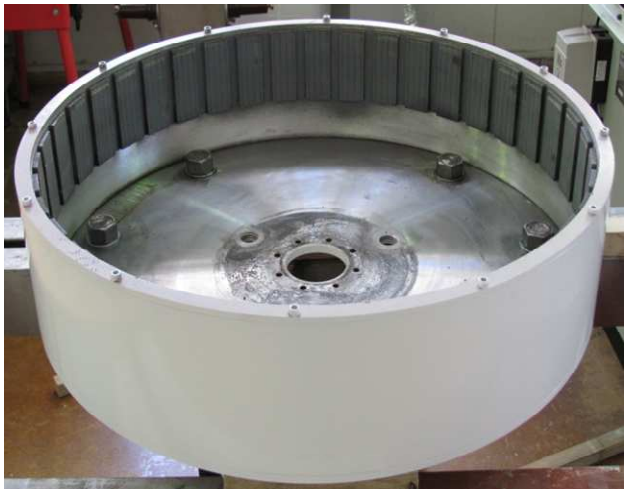

(d)

Figure 6.17: Different PM-rotor configurations with (a) a solid yoke and solid magnets (Rotor-1); (b) a solid yoke with partially segmented magnets (Rotor-2); (c) a partially segmented yoke with solid magnets (Rotor-3) and (d) a laminated yoke with partially segmented magnets (Rotor-4).

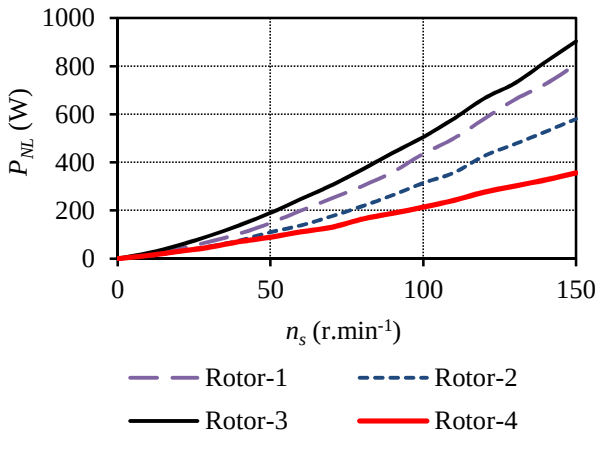

(a)

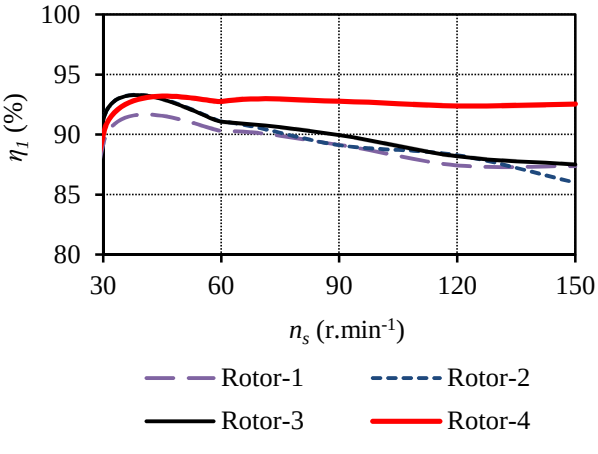

(b)

Figure 6.18: (a) Measured no-load losses and (b) measured efficiency with the PMSG connected to a resistance load for different PM-rotor configurations.

6.5 Measurements of converter-fed PMSG

In this section the PMSG connected to a full rated SSC, with the SSC as shown in Fig. 6.4 is dealt with. As the main focus of this study is on the generator design and performance, all results are measured at the generator output terminals.

6.5.1. SSC operation

Fig. 6.19 shows the active rectifier side of the SSC which is connected to the PMSG terminals through a LC-filter as shown in Fig. 6.20. The SSC controls the PMSG by means of current control, which means that the SSC needs reference values of the generator current I_1 and the power factor angle θ. The best performance of the PMSG is obtained when the current angle is set at $\alpha_s = 0$ and the generator is operated at a power factor angle lagging with respect to V_1. For $\alpha_s = 0$, $\theta = \Delta$ as can be seen from Fig. 3.3 in section 3.1.2. To simulate the machine as if connected in a wind generation setup, the machine evaluation is done at different operating points regarding speed and torque. These operating points are specified from the turbine characteristics at the different wind speeds as shown in Fig. 3.5 in section 3.2.1. From Fig. 3.5, the proposed turbine speed, which is also the PM-rotor speed of the PMSG, is shown in Fig. 6.21 versus wind speed. The torque and current reference values of the SSC are discussed in section 6.5.2. A very basic overview of the SSC system control is shown in Fig. 6.22.

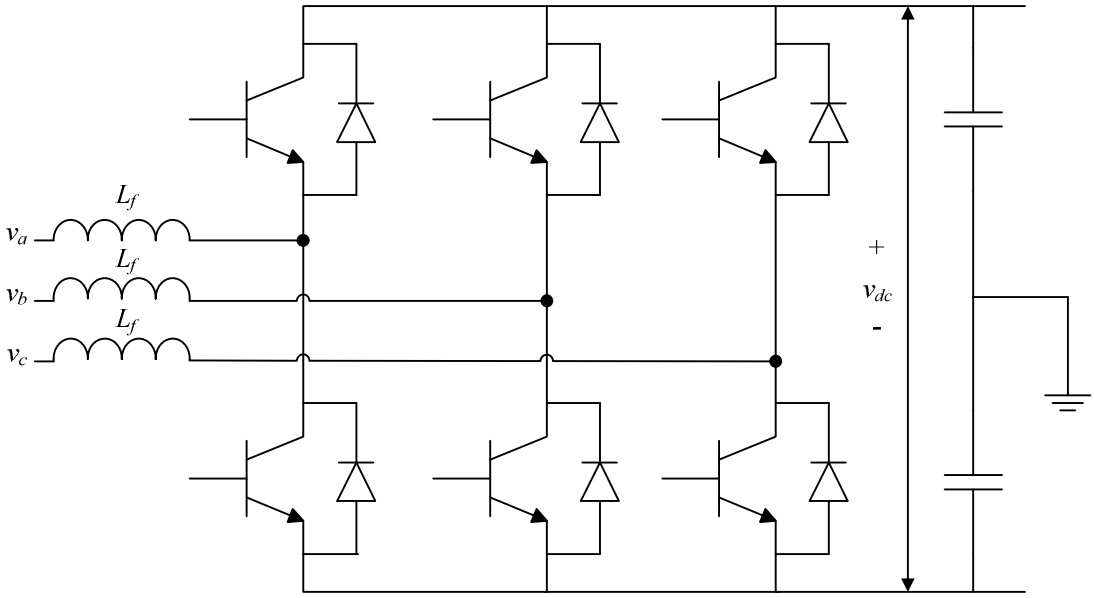

Figure 6.19: Active rectifier side of the SSC which is connected to the PMSG through the filter shown in Fig. 6.20.

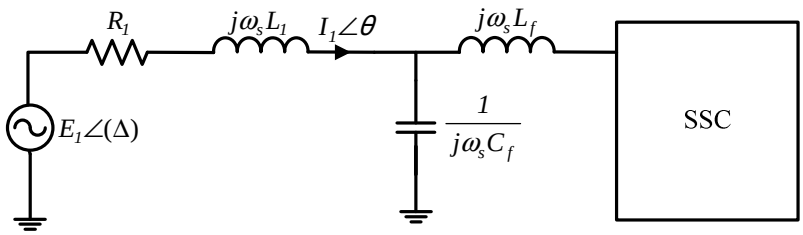

Figure 6.20: SSC filter which is connected to the PMSG output terminals and the active rectifier side of the SSC.

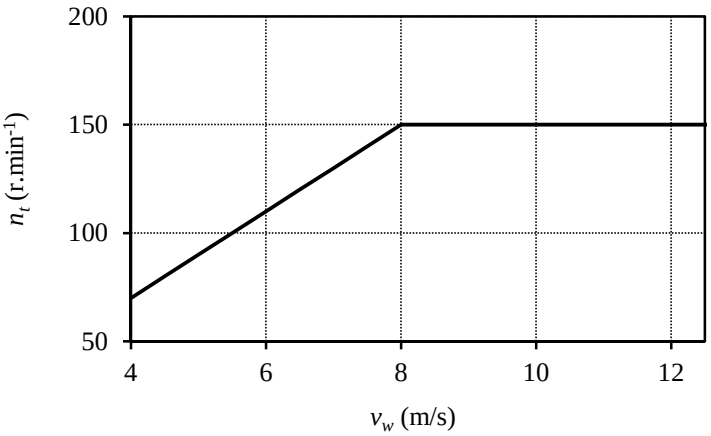

Figure 6.21: Turbine speed reference points needed for the control of the PMSG at the different wind speeds.

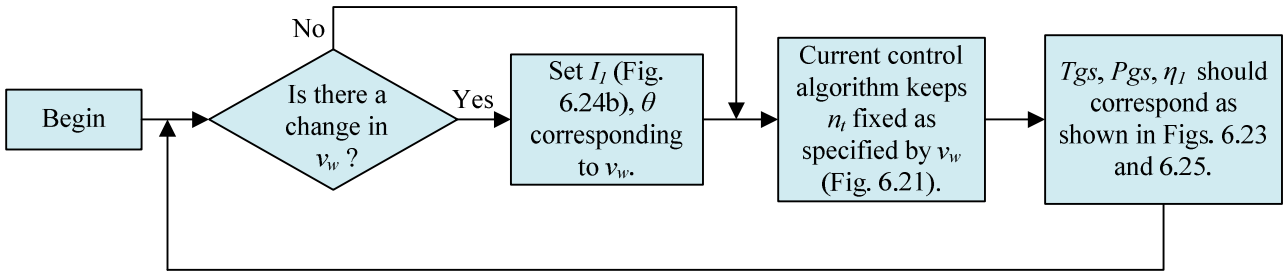

Figure 6.22: Basic overall control of SSC-connected PMSG.

6.5.2. Measured results of SSC connected PMSG

Fig. 6.23(a) shows the FE predicted - and the measured torque values at which the PMSG operates versus the wind speed reference points. The measured - and FE predicted electrical output power of the PMSG versus wind speed is shown in Fig. 6.23(b) and Fig. 6.24 shows the corresponding phase current and line voltage. As can be seen from Figs. 6.23 and 6.24 the simulated and measured values correspond well, especially at the higher load values. However, at the lower load values there are some differences between the FE predicted - and the measured performance. Especially regarding the efficiency, shown in Fig. 6.25, there is no consistency between the FE predicted - and the measured performance at the lower load values. This is also true for the power factor at which the PMSG is supposed to operate. Although the power factor is specified by specifying a value for θ at the different wind speed operating points, the measured power factor of the PMSG differs very much from what was predicted over the whole operating range.

One reason for the difference in efficiency could be the inaccuracy of the torque sensor at the lower load values, as a relatively large torque sensor is used. Another reason for the differences in efficiency and power factor could be the underestimation of the effects caused by the LC filter connecting the PMSG and the SSC shown in Fig. 6.20. Fig. 6.26 shows the line voltage and current waveforms measured at the PMSG terminals at a lower load value. Clearly the effects of the filter capacitor can be seen in the voltage and current waveforms. At the higher load values as shown in Fig. 6.27 at rated load, the filter capacitor no longer imposes any significant effects on the current and voltage waveforms. Some more explanation on the difference in the measured and the FE predicted power factor can be given by Fig. 6.9. In Fig. 6.9 it is shown that the measured inductance under load is far more than predicted by FE. This larger value of L_1, thus, also has a significant effect on the power factor of the generator, especially at the higher load values.

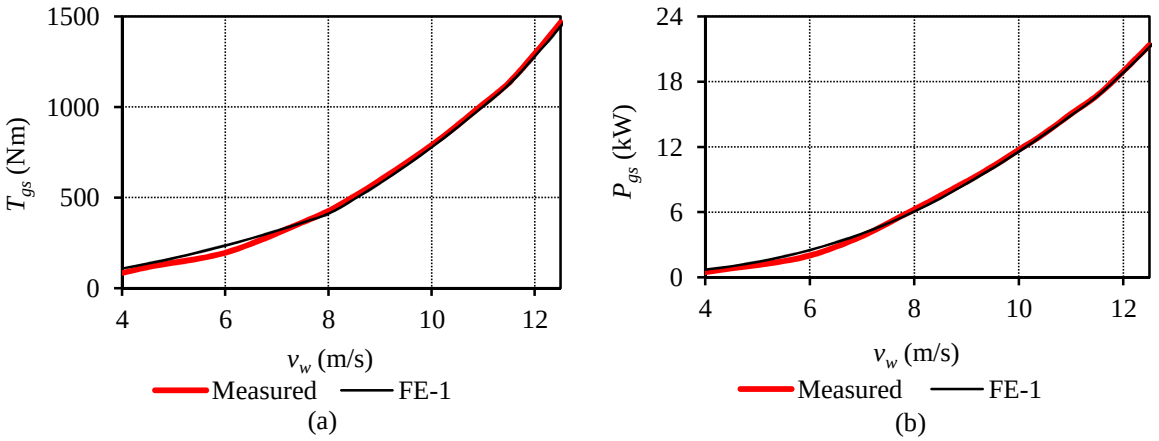

Figure 6.23: Measured - and FE predicted (a) torque and (b) electrical output power of the SSC-connected PMSG versus wind speed.

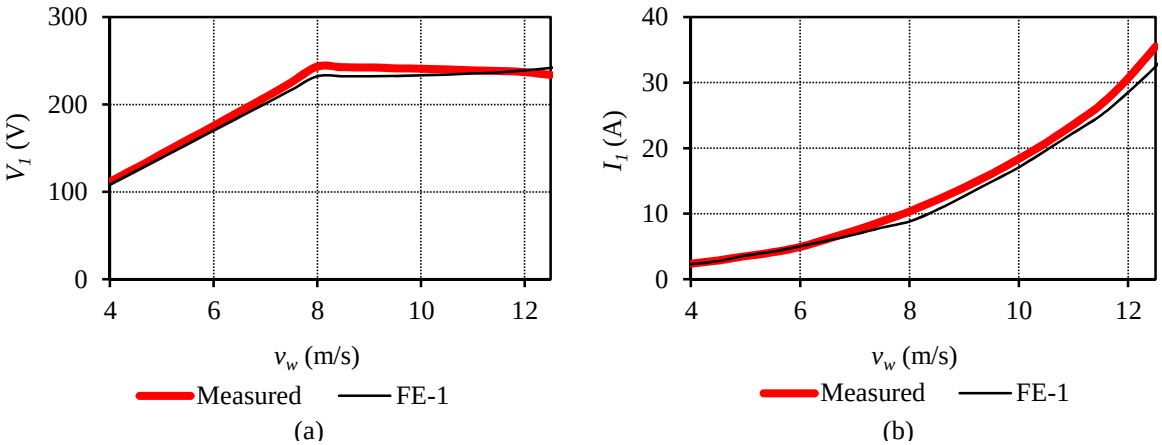

Figure 6.24: Measured - and FE predicted (a) RMS phase voltage and (b) RMS line current of the SSC-connected PMSG versus wind speed.

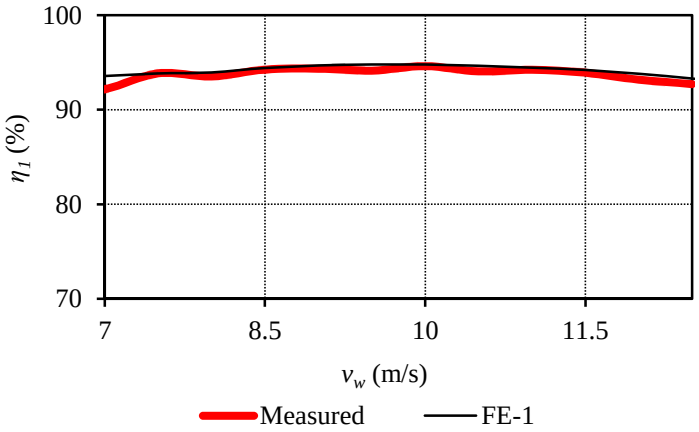

Figure 6.25: Measured - and FE predicted efficiency of the SSC-connected PMSG versus wind speed.

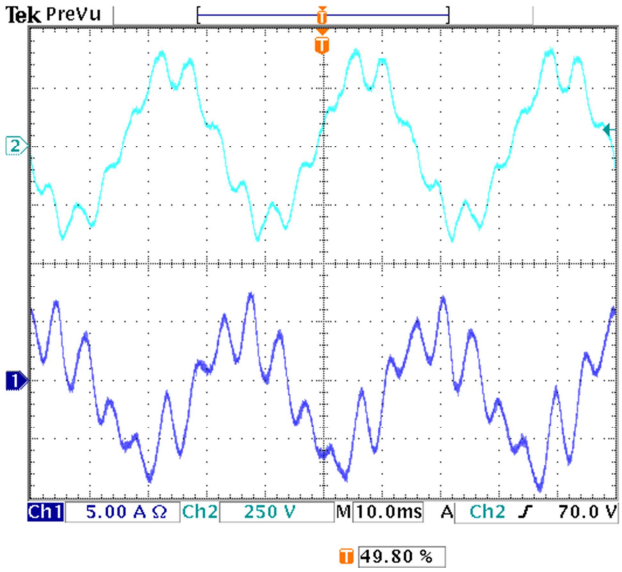

Figure 6.26: Line voltage (shown on top) and current (shown at the bottom) waveforms at a lower load value, measured at the SSC-connected PMSG output terminals.

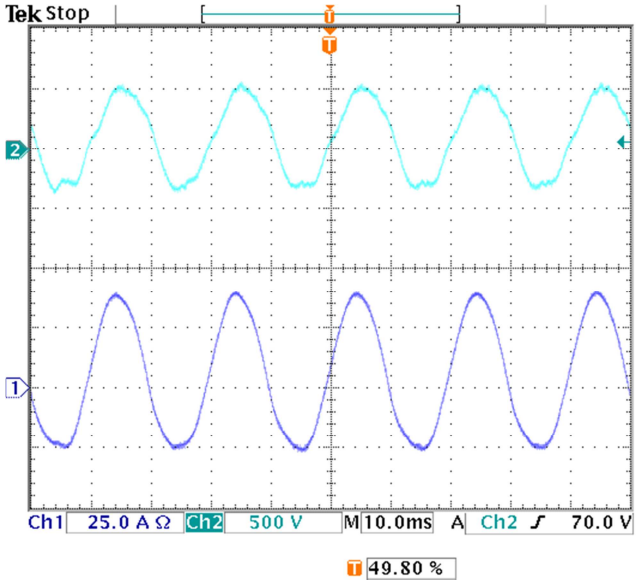

Figure 6.27: Line voltage (shown on top) and current (shown at the bottom) waveforms at the rated load value, measured at the SSC-connected PMSG output terminals.

6.6 Grid connected S-PMIG system

In this section the directly grid connected S-PMIG system as shown in Fig. 6.5 is evaluated. Although the S-PMIG tested is not the optimum machine configuration, it was still possible to obtain meaningful test results.

6.6.1 IG constructional issues

As a first iteration an S-PMIG was built which uses copper bars with aluminium pieces for end connectors as shown in Figs. 4.3(a), (section 4.3.1), and 6.6(a). This is the same IG design as given in Table 6, section 4.4. However this machine does not perform as expected. The per phase-coil resistance of this machine is far too high and this alters the torque slip characteristics of the machine significantly. The much higher resistance can be attributed to the contact resistance between the aluminium end connectors and the copper bars. With the bar coils being solid, only a few μΩ impose significant effects on the IG. FE analysis confirms the decreased IG performance if the extra resistance is added to the per phase equivalent circuit.

The contact resistance depends mainly on the methods used to fix the end connectors to the solid bars. However, in this case it is decided to solve the contact resistance issue by implementing a different IG cage-rotor design. The new cage-rotor is based on the same assembly technique as for the SG by using preformed and paralleled slot coils. In this case solid preformed bar coils cut from an aluminium sheet are used as shown in Fig. 6.28. A quick FE design was done to fit the new IG cage-rotor within the same dimensions as the previous IG cage-rotor. This new IG machine structure with its FE model and field plot are shown in Fig. 6.29.

(a) (b) (c)

Figure 6.28: (a) Solid aluminium bar coil; (b) bar coil inserted in new IG rotor stack; (c) assembled IG cage-rotor.

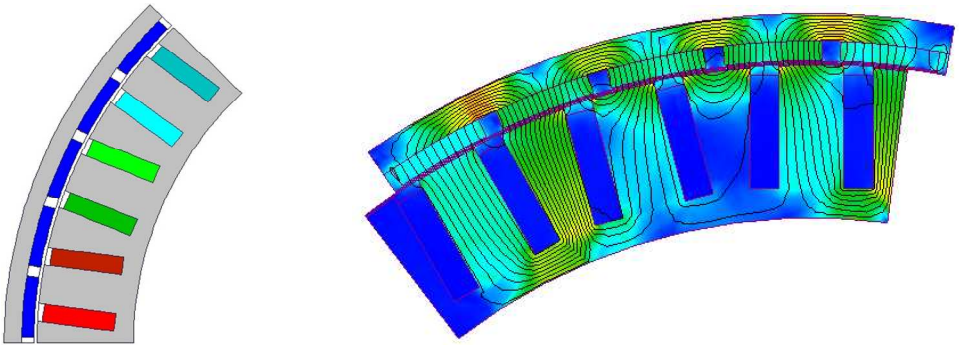

(a) (b)

Figure 6.29: (a) FE model and (b) FE field plot of the new IG unit.

6.6.2 Measured results

A. Torque-slip speed characteristics

The first conducted test is to determine the torque and slip speed characteristics of the IG unit. To ensure that only the IG parameters and no other machine losses (P_{wfs} and P_{ecs} for instance) are measured, the common PM-rotor is locked and the IG cage-rotor is now rotated at only slip speed. The result of this test is shown in Fig. 6.30. From Fig. 6.30 it is seen that the FE predicted torque and the measured torque differs significantly. Both FE-1 and FE-2 predict a much higher pull-out torque (T_b) than the measured pull-out torque.

To shed some more light on the difference between the FE - predicted and the measured torque a short-circuit test as in section 6.1 is done for the SG. In this case the short-circuit torque, corresponding to the short-circuit current shown in Fig. 6.8(b), is measured. The SG short-circuit torque versus generator speed is shown in Fig. 6.31. As for the short-circuit current, for the SG short-circuit torque, FE-1, FE-2 and FE-3 predict a much higher pull-out torque than measured.

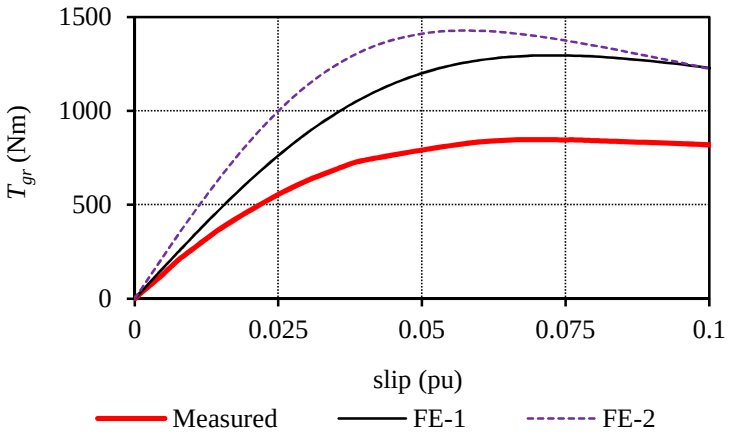

Figure 6.30: IG torque versus slip.

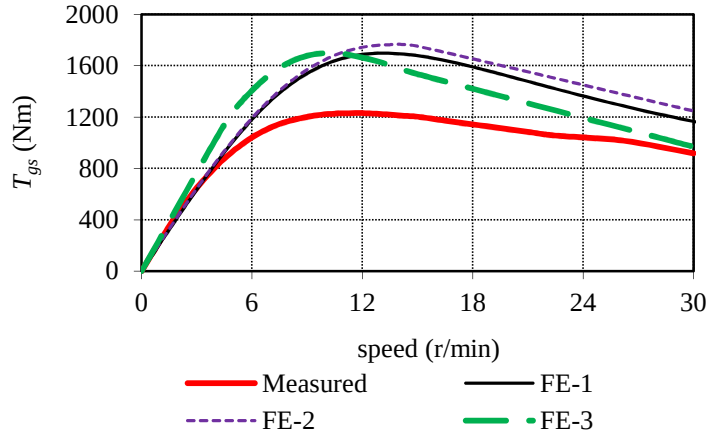

Figure 6.31: SG short-circuit torque versus PM-rotor speed.

B. Grid-connected measurements

For the direct grid connection test, measurements are taken up to the value of T_b, with the rated S-PMIG torque 1000 Nm, $T_b \approx 0.85$ pu. The S-PMIG can thus be tested up to almost 85% of the rated output power of 15 kW. It is however to be expected that the efficiency of the system will be lower than predicted due to the different torque-slip profile of the IG unit as shown in Fig. 6.30, with $\eta_2 = 1 - s$.

The FE predicted and the measured output power at the SG terminals is shown in Fig. 6.32. Fig. 6.33 shows the SG line current as well as the reactive power demand of the S-PMIG system. Although the no-load RMS voltage of the S-PMIG is exactly 230 V at the rated PM-rotor speed, the grid voltage is not always constant. At the time of the measurements the RMS grid voltage is measured as 224 V. In this case the S-PMIG is connected directly to the grid without using a variac to alter the grid voltage. The effects of the voltage difference can be observed in Fig. 6.33(b) with the S-PMIG delivering reactive power to the grid at the lower load values.

Fig. 6.34 shows the overall S-PMIG efficiency and the power factor of the system, with the lower efficiency (due to the higher slip operation) observed only at the high load values. The deterioration of the IG efficiency is clearly seen in Fig. 6.35(b) at the higher load values. The SG efficiency shown in Fig. 6.35(a), however, corresponds well with the FE predicted efficiency. Overall for the grid-connection measurements, the FE predicted results and the measured results coincide well, except for the torque performance of the IG.

Shown in Fig. 6.36 are the waveforms of the current supplied to the grid by the S-PMIG, for a RMS current of 5.8 A in (a) and 15.2 A in (b). Again the current waveform is much less distorted at the higher load current values. In this case the distortion of the current waveform is mainly attributed to the harmonic content of the grid voltage.

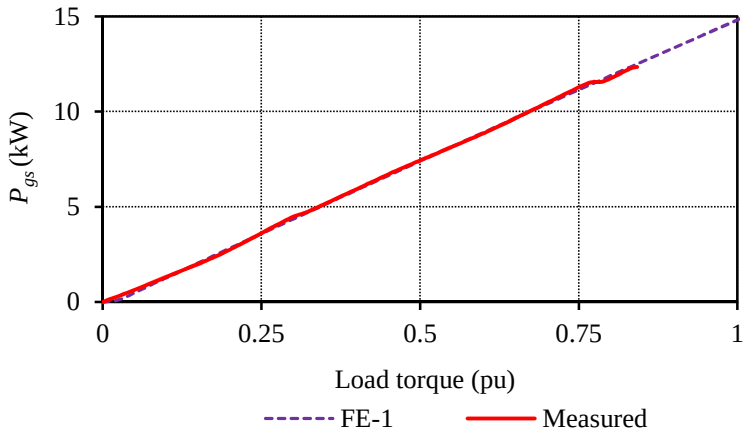

Figure 6.32: FE predicted - and measured electrical output power of the S-PMIG versus load torque.

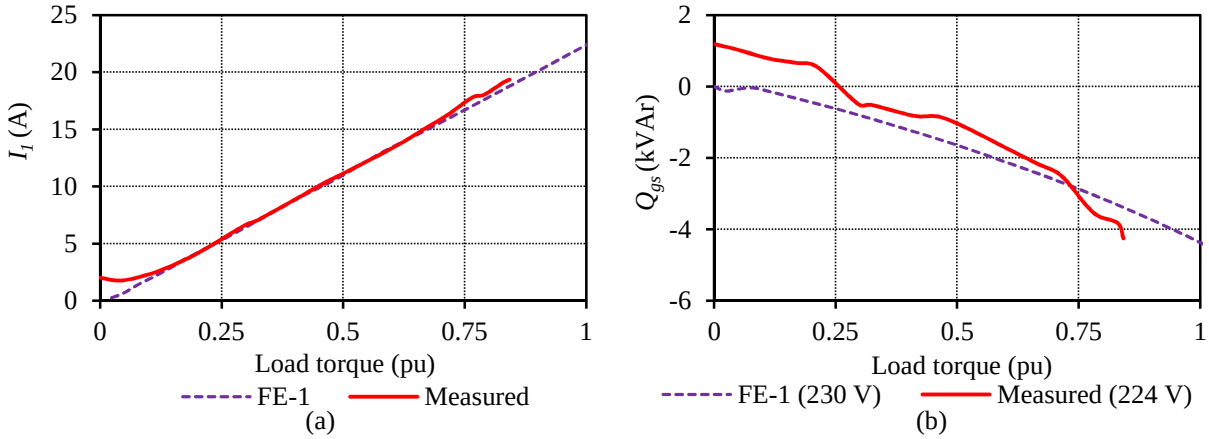

Figure 6.33: FE predicted - and measured (a) line current and (b) reactive power consumption of the S-PMIG versus load torque.

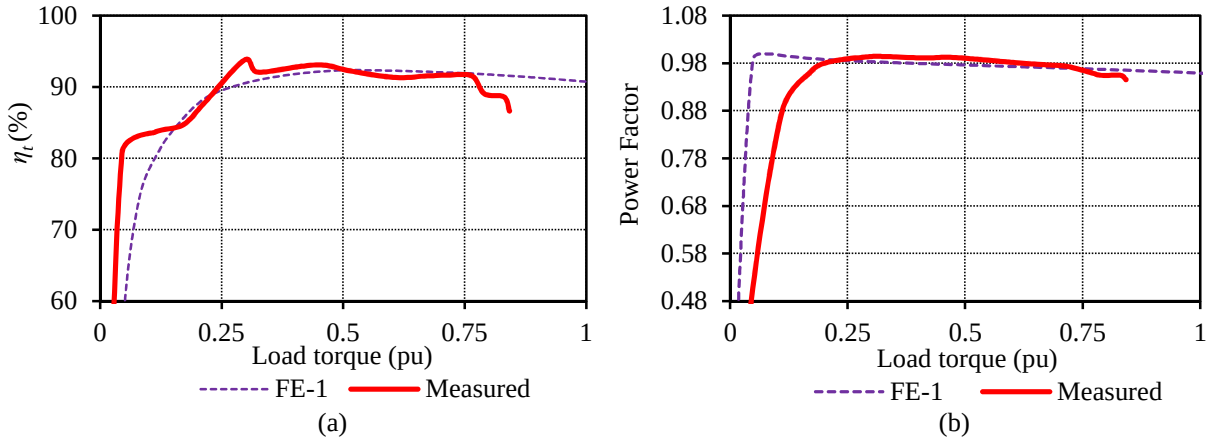

Figure 6.34: FE predicted - and measured (a) overall efficiency and (b) power factor of the S-PMIG versus load torque.

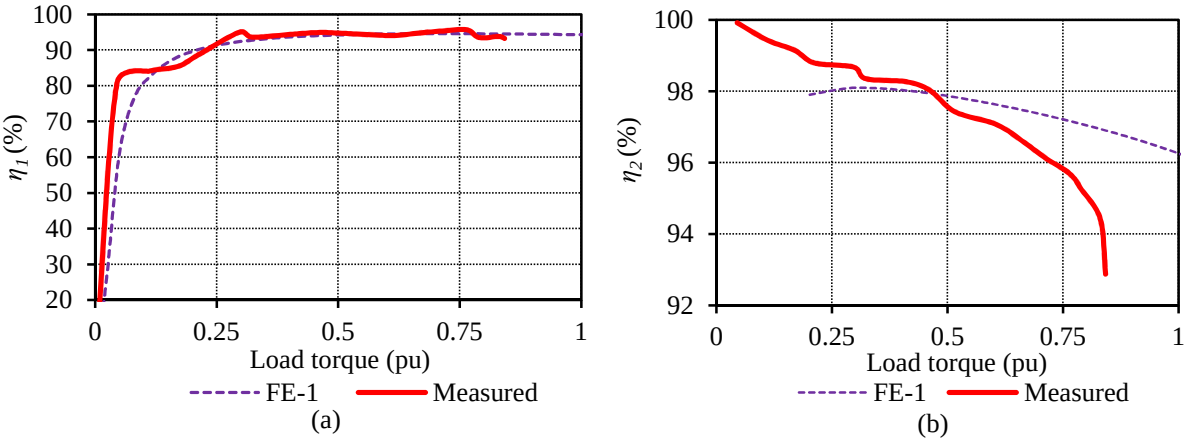

Figure 6.35: FE predicted - and measured (a) SG efficiency and (b) IG efficiency versus load torque.

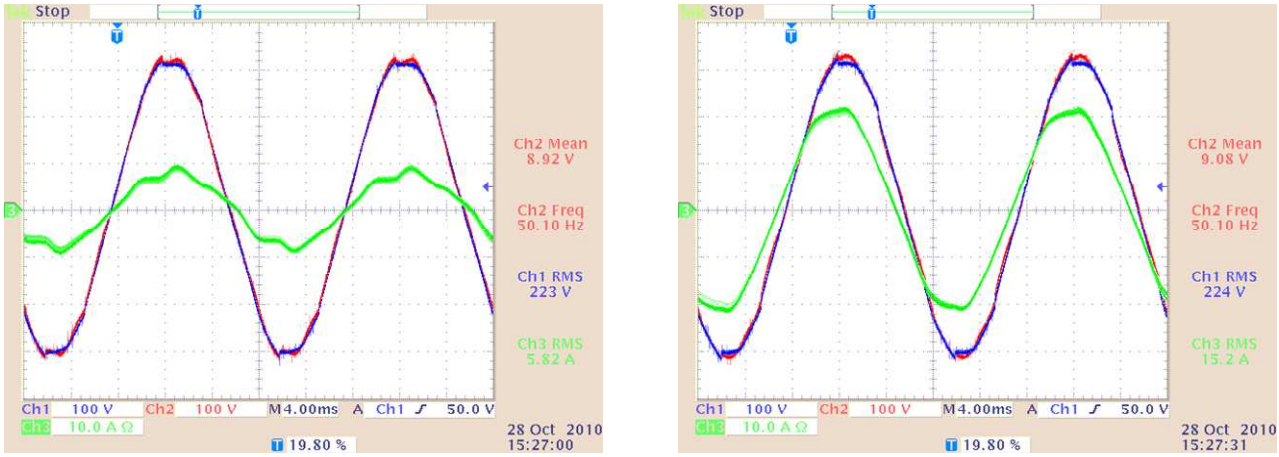

Figure 6.36: Measured current and voltage waveforms of the grid connected S-PMIG at (a) 5.8 A RMS and (b) 15.2 A RMS current supplied to the grid.

C. Dynamic response of the S-PMIG

When evaluating the dynamic response of the S-PMIG system it is not possible to supply the S-PMIG with a perfect step input as done in the dynamic simulations. This is due to the limitations of the control interface for the induction machine used as a prime mover. The average RMS current response for a torque input step of 0 to 0.7 pu of the rated torque is shown in Fig. 6.37. The S-PMIG seems to be relatively stable to sudden torque variations. The response shown is typical of what can be expected for a wind turbine connected S-PMIG system.

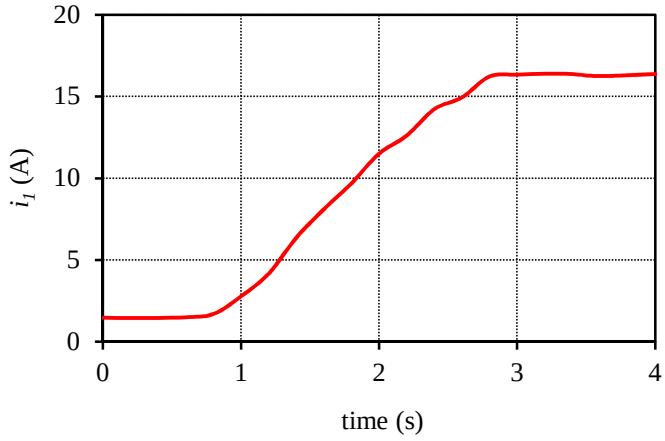

Figure 6.37: (a) Average RMS current response of the grid-connected S-PMIG for a torque step input of 0 to 0.7 pu.

C. Comparing the S-PMIG and converter-fed PMSG

The measured efficiencies of the S-PMIG and the SSC connected PMSG systems versus load torque are shown in Fig. 6.38. The comparison is done for the SG unit of the S-PMIG and the SSC connected PMSG operated at the same PM-rotor speed. For the the load region shown in Fig. 6.38 it is clear that the S-PMIG has a better efficiency than the SSC connected system.

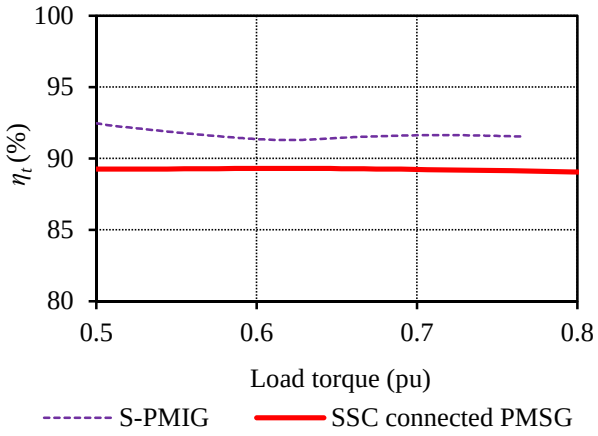

Figure 6.38: Measured efficiencies of the S-PMIG and the SSC connected PMSG versus load torque.

6.7 Summary and conclusion

From the open circuit analysis it is clear that the SG voltage closely matches the FE predicted voltage. The harmonic content of the open circuit voltage waveform, however, is found to be less than predicted and is found to comply with the local utility grid requirements. However, although the SG complies with the specifications in [43], future grid codes might be stricter and it is a question if this generator type will still be suitable for a direct grid connection. The short-circuited SG measured - and FE predicted results differ significantly. The same result is found for the IG unit with its short circuited bar windings. It seems that the FE predicted inductance value of the single layer machines is far lower than the actual inductance.

Different magnet and PM-rotor configurations are investigated. The solid PM-rotors are easier to construct and allow for a reduction in mass. However, with the use of the non-overlap single layer winding configuration severe eddy current losses result in the PM-rotor. Some improvement is observed with the use of partially segmented permanent magnets, but the solid PM-rotor yoke losses are still found to be the most dominant. Although the partially segmented PMs have the advantage of being easier to manufacture, the structural properties of these magnets are still a question. Segmented and assembled magnets with a laminated yoke are thus still the most suitable option.

In this chapter a static torque measurement setup is proposed which allows for a much more accurate cogging torque measurement. The measured cogging torque is found to be higher than the FE predicted cogging torque for both the SG and the IG unit. This can be mainly attributed to manufacturing imperfections.

The SG shows favourable results operated in a SSC-connected PMSG system, as well as in a directly grid connected S-PMIG system. No real reduction in performance of the SG for a direct grid connection at the rated operating point was observed. Efficiencies of 93 % to 95% are obtained for the SG over a wide operating range. The IG unit also demonstrates a fairly high efficiency at the lower slip values. If the correct design is implemented the S-PMIG system should have an overall efficiency of over 90 % at the rated load value. The influence of the higher measured inductance of the SG unit is also seen in the power factor measurements of both the directly grid connected S-PMIG system and the SSC-connected system. In order to predict the performance of the PM machines correctly, it is thus important that further investigations are done to explain the increased inductance as the higher inductance has an especially large influence on the performance of the IG unit.

Chapter 7 – Conclusion

The main focus of this study is to evaluate the possibility of implementing a direct-drive, directly grid connected PM wind generator, by means of the PMIG concept. A first experiment based upon studies reported in available literature (C-PMIG concept) showed a promising performance of this generator type. However, the mechanical complexity and construction of this generator type are found to be limitations.

Proposed S-PMIG

To simplify the mechanical design and alleviate some of the constructional issues this study proposes a variation of the conventional PMIG system, defined as the split permanent magnet induction generator (S-PMIG). It is found that by axially separating the two machines a further simplification in the mechanical design is possible. The result is, thus, a completely modular generator system, which can either be operated as a SSC connected SG system or as an S-PMIG system with the addition of the IG unit. With the generator being completely modular, the FE design for both units is done completely independently. The focus throughout the whole design process is to present this generator as an easily constructible, low maintenance, cost effective alternative to other wind generation systems.

SG design

To simplify the SG design a non-overlap, single layer winding is proposed. A further simplification is done by using preformed modular coils. A drawback of the single layer winding, however, is the large sub MMF harmonic content. There is also a large harmonic content present in the generator induced voltage. However it is shown that the voltage waveform can be improved by changing some of the machine design parameters.

For a more simplified design the use of solid rotor yokes and solid magnets are evaluated. The losses in the solid yokes and magnets are found to be severe for this non-overlap single layer winding machine. The partially segmented solid permanent magnets have a performance improvement over the solid permanent magnets and are easier to manufacture than conventional segmented permanent magnets. However, the structural properties of these magnets are still a question. For the best performance, conventional segmented permanent magnets with a laminated yoke are still the best option for the choice of PM-rotor.

Due to the irregular slotting caused by the paralleled slot configuration, to incorporate the preformed windings, the cogging torque minimisation of this machine poses some difficulty. To address this problem, a thorough cogging torque analysis is done. In this study the sensitivity of the cogging torque to variation of different parameters is investigated. From this analysis the optimum parameter regions for the best cogging torque performance are identified. It should be noted that the accuracy of some parameters are more difficult to control during the manufacturing process than that of others. This is especially true for the permanent magnets. Parameter regions where a variation in the magnet dimensions has the least effect on the cogging torque should, thus, be selected. A static measurement technique is also proposed in this study to measure the no-load cogging torque more accurately. However, it is extremely difficult to measure the cogging torque exactly as predicted by FE, as even slight manufacturing errors impose significant changes.

IG design

The machine modelling and design of the IG are mostly based upon the design of the SG. The current IG design however, is found unsuitable for use in the current S-PMIG wind generator system due to the inability of the IG to match the required turbine torque. The FE predicted - and measured torque differs significantly. The same difference in measurement and FE prediction is found for the short-circuited SG. It is clear that the inductance of the non-overlap single layer winding is much higher under load than predicted by the FE analysis. Hence, some more investigation is needed to update the FE models in order to predict the torque profile of these machines more accurately. Meaningful S-PMIG measurements, however, are still obtained from the current S-PMIG design, with the S-PMIG having a higher efficiency than the SSC connected PMSG system. Even better results can be obtained if the correct IG design is implemented.

If a non-overlap single layer winding is to be used for the IG unit, the size of the machine needs to be increased. A double layer non-overlap winding might still provide the required performance, but the winding configuration is much more complex. A normal overlap cage winding design might result in a better torque performance without increasing the size of the machine. However, this winding type might require special torque ripple minimisation techniques as cogging torque in this case is much more of a problem. Further studies are, thus, needed in this regard. The manufacturing technique of the normal cage is also a question. In this case the cage most likely needs to be casted.

Grid Connection

It is still questionable if the induced voltage waveform of the SG unit is acceptable. Although measurements illustrate that the quality of the no-load induced voltage complies with current local grid requirements, these requirements might become stricter in the future.

It is known that the directly grid connected SG compensates for grid voltage variations by injecting or drawing reactive power from the grid as seen from the practical measurements. If reactive power flow is undesirable, the feasibility of tap changing transformers as well as STATCOM systems in conjunction with the S-PMIG can be investigated. The low voltage ride through capability of this generator also needs to be investigated, to see if the machine behaviour at low voltage conditions are acceptable. In this case the higher inductance value might be an advantage, as it acts as a buffer between the generator and the grid. If low voltage conditions occur it will largely limit the short-circuit current of the generator. Furthermore, simulations also found the S-PMIG to damp some of the unwanted effects causing voltage flickering.

Feasibility of the S-PMIG concept

The feasibility of the fixed speed operation of the S-PMIG, which will result in a lower energy yield at the lower wind speeds needs to be investigated. This lower energy yield will, however, be highly dependent on the turbine design as well as the wind speed distribution at the site where the generator is installed. The S-PMIG can also be implemented in variable speed applications. There is the option of connecting several PMIGs in conjunction, to a variable voltage and frequency controlled grid. The single SSC used for several wind generators instead of one for each wind generator might have some advantages. This could especially be beneficial for HVDC transmission, by having an AC collection grid with a central DC distribution. The other variable speed option is to implement the PMIG as a doubly-fed system by using a wound IG rotor and by controlling the rotor frequency. However, further studies are still needed regarding the feasibility of these concepts. In the end it comes down to the cost per unit of energy produced. A thorough cost analysis of the S-PMIG as well as that of other wind generating systems is needed to compare the S-PMIG system with others based upon the annual energy yield of each type of system. Other factors which could favour the S-PMIG system are the reduced maintenance and increased robustness of this system and the fact that there are fewer components that can fail. This can lead to shorter wind generator down times, which has significant economic implications.

The weight of the S-PMIG is also a problem. For the current system the total generator mass increase of the PMSG to S-PMIG system is about 1.7 pu. A normal overlap cage winding with a better IG torque performance might result in a lower mass. The mass of the IG will, however, still be mostly dependent on the specified maximum torque and efficiency of the IG. Furthermore although the generator's mass increase is 1.7 pu, the overall tower top mass increase will be very much less.

From this study it can be concluded that the S-PMIG system can work and operate in a stable way in a wind generating setup, and that the mechanical issues previously associated with this machine type can be solved. The study conducted provides an initial basis for the working principles and design of a generator of this type. This study is the first known instance of a large diameter high pole PMIG ever being built. Further studies should be done to improve the concept. To obtain a true reflection on the feasibility of this concept, it is essential that a design which can be implemented in a wind generator field-test setup is obtained.

References

[1] Anca D. Hansen and Lars H. Hansen, "Market penetration of wind turbine concepts over the years", Proc. of the European Wind Energy Conference & Exhibition, Milan, Italy, 2007

[2] Det Norske Veritas (DNV) and Risø National Laboratory, *Guidelines for design of wind turbines*, 2nd ed., Denmark, printed by Jydsk Centraltrykkeri, 2002.

[3] Leon Freris and David Infield, *Renewable energy in power systems*, United Kingdom, Wiley, 2008.

[4] Siegfried Heier, *Grid integration of wind energy conversion systems*, United Kingdom, Wiley, 2006.

[5] Peter Jamieson, *Getting out of gear and into magnets*, Garrad Hassan, Wind power Monthly, November 2008.

[6] D. Howe and K. Atallah, "A novel high-performance magnetic gear", *IEEE Trans. on Magnetics*, Vol. 37,No. 4, pp. 2844-2846, July 2001

[7] H. Müller, M. Pöller, A. Basteck, M. Tilscher, and J. Pfister, "Compatibility of variable speed wind turbines with directly coupled synchronous generator and hydro dynamically controlled gearbox" Sixth Int'l Workshop on Large-Scale Integration of Wind Power and Transmission Networks for Offshore Wind Farms, Delft, Netherlands, 26–28 October, 2006.

[8] A.J.G. Westlake, J.R. Bumby and E. Spooner, "Damping the power angle oscillations of a permanent-magnet synchronous generator with particular reference to wind turbine applications", *IEE Proc. Power Appl.*, Vol. 143, No. 3, May 1996.

[9] F. Punga and L. Schon, "Der neue kollektorlose einphasenmotor der firma krupp", *Elektro-technishe Zietschrift*, Bucharest, Rumania, vol. 47, pt 1, no. 29, pp 842-847; pt II, pp 877-881, July 1926.

[10] J. F. H. Douglas, "Characteristics of induction motors with permanent-magnet excitation," *Trans. AIEE Power Apparatus and Systems*, vol. 78, pp. 221-225, June 1959.

[11] J. K. Sedivy, "Induction motor with free-rotating DC excitation, "*IEEE Trans. Power App. Syst.*, vol. PAS-86, pp. 463–469, Apr. 1967.

[12] W.F. Low and N. Schofield, "Design of a permanent magnet excited induction generator", Proc. International Conference on Electrical Machines ICEM 92, 1077–1081, Manchester University, United Kingdom, 1992.

[13] T. Epskamp, B. Hagenkort, T. Hartkopf and S. Jöckel, "No gearing no converter - assessing the idea of highly reliable permanent-magnet induction generators" Proc. of EWEC 1999,Nice, France, pp. 813-816.

[14] B. Hagenkort, T. Hartkopf, A. Binder and S. Jockel, "Modelling a direct drive permanent magnet induction machine", Proc. of the International Conference on Electrical Machines (ICEM), Espoo (Finland), Aug. 2000,pp. 1495-1499.

[15] G. Gail, T. Hartkopf, E. Troster, M. Hoffling, M. Henschel and H.Schneider, "Static and dynamic measurements of a permanent magnet induction generator: Test results of a new wind generator concept", Proc. of the International Conference on Electrical Machines (ICEM'04), Cracow, Poland, Sept. 2004.

[16] E. Tröster, T. Hartkopf, H. Schneider, G. Gail, M. Henschel, "Analysis of the equivalent circuit diagram of a permanent magnet induction machine", Proc. of the International Conference on Electrical Machines (ICEM), Cracow, Poland, Sept. 2004.

[17] E. Tröster, M. Sperling and T. Hartkopf, "Finite element analysis of a permanent magnet induction machine", International Symposium on Power Electronics, Electrical Drives, Automation and Motion (SPEEDAM), Taormina (Sicily), Italy 2006.

[18] Yoshiyuki Shibata, Nuio Tsuchida and Koji Imai, "High torque induction motor with rotating magnets in the rotor", *Electrical Engineering in Japan*, vol. 117, No. 3, 1996.

[19] Yoshiyuki Shibata, Nuio Tsuchida and Koji Imai, "Performance of induction motor with free-rotating magnets inside its rotor", *IEEE Trans. on Industrial Electronics*, vol. 46, no. 3, June 1999.

[20] Tadashi Fukami, Kenichi Nakagawa, Ryoichi Hanaoka, Shinzo Takata and Toshio Miyamoto,"Non linear modelling of a permanent-magnet induction machine", *Electrical Engineering in Japan*, vol. 144, no. 1, 2003

[21] T. Fukami, M. Yokoi, Y. Kanamaru and T. Miyamoto, "Performance evaluation of a permanent magnet induction generator", *IEEJ Trans. Ind. Appl.*, vol. 123, no. 9, pp. 1065-1070, Sep. 2003.

[22] Tadashi Fukami, Kenichi Nakagawa, Yasunori Kanamaru and Toshio Miyamoto, "A technique for the steady-state analysis of a grid-connected permanent-magnet induction generator", *IEEE Trans. on Energy Conversion*, vol. 19, no. 2, Jun. 2004.

[23] T. Tsuda, T. Fukami, Y. Kanamaru and T. Miyamoto, "Performance analysis of a permanent magnet induction generator connected to a single-phase power grid", *IEEJ Trans. Ind. Appl.*, vol. 125, no. 6, pp. 666-672, Jun. 2005.

[24] T. Tsuda, T. Fukami,Y. Kanamaru and T. Miyamoto, "Experimental study on the inrush current in a permanent magnet induction generator" presented at the Natl. Conv. Rec. IEEJ, 2006, 5-140

[25] T. Tsuda, T. Fukami,Y. Kanamaru and T. Miyamoto, "Effects of the built-in permanent magnet rotor on the equivalent circuit parameters of a permanent magnet induction generator", *IEEE Trans. on Energy Conv.*, vol. 22, no 3, Sept. 2007.

[26] A.J. Thomas, "A Doubly-fed permanent magnet generator for wind turbines", Master dissertation, Massachusetts Institute of Technology, June 2004.

[27] J.H.J. Potgieter, A.N. Lombard, R-J Wang and M.J. Kamper, "Evaluation of a permanent magnet excited induction generator for renewable energy applications", *Southern African Universities Power Engineering Conference (SAUPEC)*, Stellenbosch, South Africa, Jan. 2009, pp. 299-304.

[28] R. Vermaak, J.H.J. Potgieter and M.J. Kamper, "Grid-connected VSC-HVDC wind farm system and control using permanent magnet induction generators", IEEE International Conference on Power Electronics and Drive Systems (PEDS), Tapei, Taiwan, Nov. 2009.

[29] J.H.J. Potgieter and M.J. Kamper, "Design of new concept permanent magnet induction wind generator", IEEE Energy Conversion Congress & Expo (ECCE), Atlanta (USA), 12-16 Sept. 2010.

[30] Bernd Ackermann, "Single-phase induction motor with permanent magnet excitation", *IEEE Trans. on Magnetics*, vol. 36 no. 5, Sept. 2000

[31] M.J. Kamper, "The design criteria and development of a design program for squirrel-cage induction motors with use in the load region", Master dissertation, University of Stellenbosch, South Africa, 1987.

[32] I. Boldea and S.A. Nasar, *The induction machine handbook*, CRC Press, 2002

[33] M.J. Kamper, "Design optimisation of cageless flux barrier rotor reluctance synchronous machine", Ph.D. dissertation, University of Stellenbosch, South Africa, 1996

[34] M.J. Kamper, F.S. van der Merwe and S. Williamson, "Direct finite element design optimisation of the cageless reluctance synchronous machine", *IEEE Trans. on Energy Conversion*, vol. 11, no. 3, Sept. 1996, pp. 547-553

[35] M.J.D. Powell, "An efficient method for finding the minimum of a function of several variables without calculating derivatives", *Computer Journal*, vol. 7, pp. 155-162, 1964

[36] P.E. Gill, W. Murray and M.H. Wright, *Practical optimization*, Academic Press (London), 1981, pp. 117-133 and pp. 335-338.

[37] D.A. Wills and M.J. Kamper, "Analytical prediction of rotor eddy current loss due to stator slotting in PM machines", IEEE Energy Conversion Congress & Expo (ECCE), Atlanta (USA), 12-16 Sept. 2010.

[38] D.A. Wills and M.J. Kamper, "Reducing rotor eddy current losses using partial magnet and rotor yoke segmentation.", Proc. of Int. Conf. on Electrical Machines (ICEM'10), Rome, Italy, Sept, 2010.

[39] J.N. Stander, "The specification of a small wind energy conversion system for the South African Antarctic research base SANAE IV", Master dissertation, Department Mechanical and Mechatronic Engineering, University of Stellenbosch, South Africa, 2008

[40] J.H.J. Potgieter, M.J. Kamper, "Cogging torque sensitivity in design optimisation of low cost non-overlap winding PM Wind Generator", Proc. of Int. Conf. on Electrical Machines (ICEM'10), Rome, Italy, Sept, 2010.

[41] S.E. Skaar, O. Krovel and R. Nilsen, "Distribution, coil-span and winding factors for PM machines with concentrated windings", Proc. Of Int. Conf. On Electrical Machines (ICEM'06), Chania, Crete Island, Greece, Sept. 2006.

[42] M.J. Kamper, A.J. Rix, D.A. Wills and R-J Wang, "Formulation, finite-element modelling and winding factors of non-overlap winding permanent magnet machines", Proc. of Int. Conf. on Electrical Machines (ICEM'08), Vilamoura, Portugal, Sept. 2008.

[43] *Electricity Supply - Quality of supply, Part 2: Voltage characteristics, compatibility levels, limits and assessment methods*, Standards South Africa, NRS 048-2:2004, June 2004

List of Figures

List of Tables